University of Naples "*Federico II*"
Department of Physics "*E. Pancini*"

Doctor of Philosophy in Novel Technologies
for Materials, Sensors and Imaging - XVIII cycle

Laser-driven beams for future medical applications

Francesca Margaret Perozziello

PhD Thesis

Tutor:
Dr. Lorenzo Manti

March 2016

…to my grandfather Richard

Laser-driven beams for future medical applications

Introduction

Cancer is one of the leading causes of death in developed countries and one-third of the population experiences it during their lifespan [1]. This drives and motivates research activities spanning from physics, biology and medicine into novel, more cost-effective ways of cancer prevention and treatment.

Radiotherapy with charged particles (mainly protons and carbon ions), known as hadrontherapy, has become an increasingly common treatment modality, because of several advantages it offers compared to photons [2]. These are both physical and radiobiological. Charged particles have a peculiar nature of physical energy deposition path in matter, which is described by the Bragg curve. As a result, they deposit most of their energy at the end of their range, thus allowing a much better localization of the dose distribution within the tumor volume compared, for example, to X-rays. Moreover, heavier charged particles such as carbon ions exhibit a higher radiobiological effectiveness due to their denser ionization event pattern through matter, hence they cause more severe cellular damage, e.g. clustered DNA breaks, in comparison with photons that are, instead, characterized by ionization events spatially distributed.

Clinical facilities employing charged-particle beams produced by synchrotron, cyclotron or LINAC accelerators have to face high installation (approximately 200M€ per center) management and running costs besides the vast areas needed to install such equipment, which considerably limits their expansion. Despite that, to date, there are over 40 operating hadrontherapy centers worldwide, the majority of which employing protons [3], and a growing interest exists towards this modality of cancer treatment [4]. Hence, there is a strong need to find novel approaches in order to improve the large-scale adoption of hadrontherapy.

Innovative solutions are looking to find a compact, flexible and cost-effective solution such as employing laser-based accelerators to obtain higher performance at lower costs [5]. In the last decades, in fact, optical ion acceleration due to laser-plasma interaction

has become a popular topic for multidisciplinary applications and opened new scenarios in the ion therapy framework, representing a possible future alternative to classic accelerators. Up to now, the highest energies laser-driven ion beams have been produced exploiting the TNSA (Target Normal Sheath Acceleration) mechanism. In this regime, ultra-short (from *fs* to *ps*) and ultra-intense ($\geq 10^{19}$ W/cm^2) lasers interacting with solid targets are conceived to produce laser-driven proton beams with energies (in the near future) useful for medical applications, i.e. in the order of 250 MeV. This leads to a necessary research activity to develop new instrumentation and methodologies for dosimetry and radiobiology in order to realize a hadrontherapy facility based on laser-driven proton beams.

Clinically exploitable laser-accelerated beams require the achievement of specific physical constraints, such as beam reproducibility and stability as well as irradiated field homogeneity. Once these requirements are met, radiobiological investigations become mandatory in order to validate their future therapeutic use.

Currently there is a significant technological effort to achieve a satisfactory level in the proton beam parameters for laser-driven sources to be a realistic alternative to "conventionally" accelerated beams. As above mentioned, laser-driven beams have a completely different regime. Plasma-emitted ions are characterized by ultra-high dose rates exceeding 10^9 Gy/s, that is several orders of magnitude greater than the conventional therapeutic working regime of 1-10 Gy/min [6-7].

There exist at least two major concerns: one regards the ability to control transport and dosimetry of beams with such peculiar features; the other is to understand the dependence of the biological effects from the extreme spatio-temporal nature of the physical pattern of the energy deposition events [8].

The design of laser-based accelerating facilities for clinical applications is part of a large EU-funded project called ELIMED (ELI-Beamlines MEDical applications), which is part of the international network ELIMAIA (ELI Multidisciplinary Applications of laser-Ion Acceleration). This is being developed at the ELI-Beamlines (Extreme Light Infrastructure) facility in Prague, Czech Republic, in close association with the Italian INFN (National

Institute of Nuclear Physics). Radiation therapy applications are the ideal candidate as demonstration-case because they are the most demanding and challenging in terms of beam stability, dosimetry and diagnostic performances.

The experimental work illustrated in this thesis has dealt with dosimetric and radiobiological studies of laser-driven proton beams in view of future medical applications.

A prototype of a major component of the whole BTL (Beam Transport Line) system, the Energy Selector System (ESS), able to control and select the energies of the laser-driven proton beam, thereby delivering a beam with required properties, has already been developed and experimentally characterized with mono-energetic proton beams at LNS-INFN, Catania and LNL-INFN Legnaro, Italy, and with a laser-driven proton beam available at the TARANIS laser facility, Belfast Queen's University (UK).

In fact, work carried out at the latter facility pointed out some issues regarding the current layout of the ESS, which was found to cause beam non-uniformity and low fluence. This has led to the design of a module of four permanent magnetic quadrupoles (PMQ) to be placed before the ESS in order to maximize the transmission efficiency and the uniformity of particles distribution (the PMQ has been recently delivered at LNS-INFN, Catania, Italy).

Moreover, preliminary radiobiological investigations have been successfully carried out on normal human umbilical vein endothelial cells (HUVEC) by means of laser-driven protons produced in the TNSA regime with $5x10^{19}$ W/cm^2 short pulse laser (1,3 ps) at the $LULI_{2000}$ facility in Paris, France. The obtained results were compared with pulsed proton beams and classically accelerated proton beams produced at LNS-INFN, Catania (IT).

Chapter 1

Scientific rationale of the use of charged particles for medical applications

1.1 Physics background

Radiation interaction with matter causes an energy transfer to the atomic/molecular structure of the traversed material. Radiation having sufficient energy to excite and/or eject an electron from an atomic structure of the material is referred to as ionizing radiation (IR, figure 1). If an electron is expelled, the energy released into the target is higher than the binding energy of the electron to the nucleus and its velocity is proportional to the difference between the absorbed energy and its binding energy. When dealing with the biological effects of exposure of living matter (i.e. cells or sub-cellular structures) to IR, depending on whether the ionization event of the irradiated matter occurs via direct or indirect mechanisms it is possible to distinguish between *directly ionizing* and *indirectly ionizing* radiation. Electrons, α-particles and, in general, charged particles, are directly ionizing radiation, while X-rays, γ-rays and neutrons are indirectly ionizing.

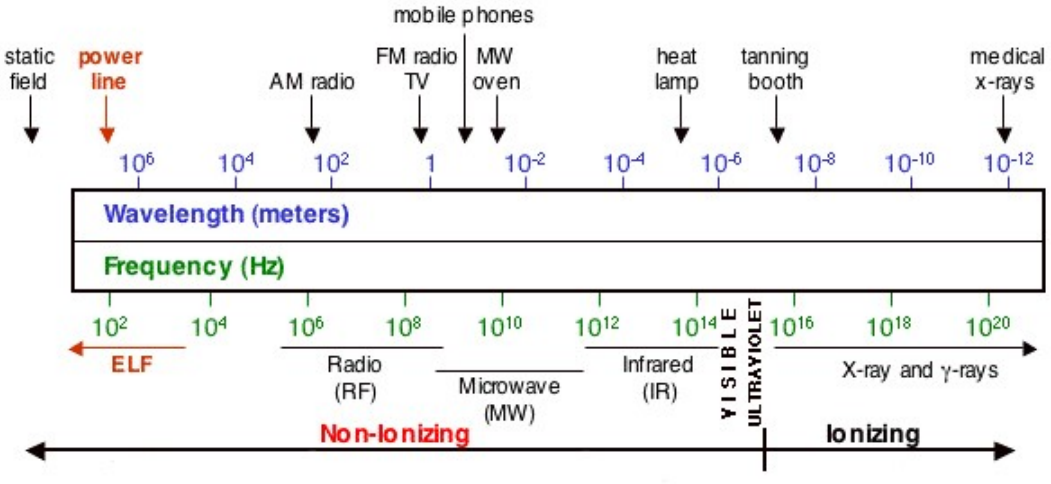

Fig 1 Electromagnetic spectrum. Ionizing radiations have frequency values (v) > $3x10^{16}$Hz.

1.1.1 Directly and indirectly ionizing radiation

Directly ionizing radiation consist of charged particles that release kinetic energy in the interaction with matter able to directly ionize the target; the energy loss is due to inelastic collisions with orbital electrons and through elastic scattering with the nucleus. The elastic collision with the nuclei happens frequently, although it has a lower probability in comparison to the electronic collisions, and transfers to matter a negligible amount of the total energy lost by the projectiles. Each single collision is a statistical process that can occur with a certain probability. The heavier the mass of the incident particle, the higher the number of collisions per track, so the statistical fluctuations of the total energy loss are low; therefore, it becomes possible to consider the mean energy loss per unit length of the particle track. A first evaluation of this process was made by Bohr and it was based on purely classical principles [9]. Later, Bethe and Bloch proposed a calculation using quantum mechanics principles. The energy loss per unit length is then described by the so-called Bethe- Bloch formula:

$$-\frac{dE}{dx} = 2\pi N_a r_e^2 m_e c^2 \rho \frac{Z}{A}\frac{z^2}{\beta^2}\left[ln\frac{2m_e\gamma^2 v^2 T_{max}}{I^2} - 2\beta^2 - \delta - 2\frac{C}{Z}\right]$$

dx: target thickness, expressed in in g/cm^2

r_e: classical electron radius

m_e: electron rest mass

N_a: Avogadro's number

ρ: target density

Z: atomic number of the target

z: charge of the projectile expressed in electron charge unit (e)

A: relative atomic mass of the target

β: ratio between the velocity of the incident particle and that of light v/c

T_{max}: maximum energy transferred in a single collision

I: mean excitation potentikal.

In the above formula there are two correction terms, δ e $\frac{C}{Z}$. The first, δ, represents the *density effect correction*, is relevant at high energies and is related to the particle electric field that polarizes the atoms along its path. The atom polarization shields the electric field to which the electrons (far from the ions path) are subjected, therefore the collisions with these electrons gives a slight contribution to the total energy loss.

The second correction factor, $\frac{C}{Z}$, is known as a *shell correction*: it becomes important when the speed of the incident particle is comparable (or smaller) to the speed of the bounded orbital electrons. Figure 2 shows the trend of the energy loss by the protons in a copper layer described by the Bethe- Bloch formula with and without the correction terms.

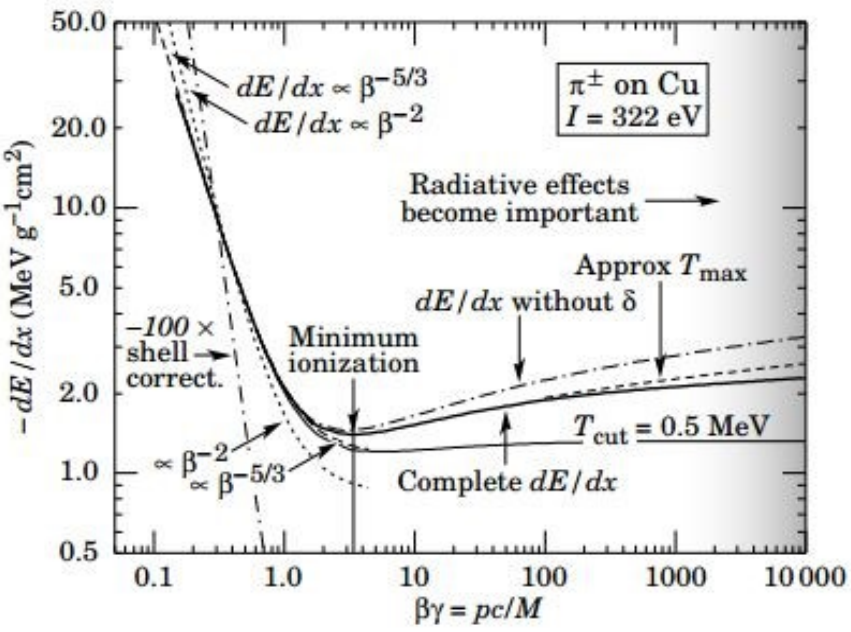

Fig. 2 Energy loss in copper. The function without the density effect correction is also shown, as is the shell correction and two low-energy approximations.

The energy loss per unit length changes with the kinetic energy of the incident particle; the higher the initial energy, the lower the energy released in matter and vice versa. Therefore, the energy deposition becomes significant at low kinetic energy values at the

end of the track path. The energy loss as a function of depth is graphically represented by the Bragg peak (figure 3).

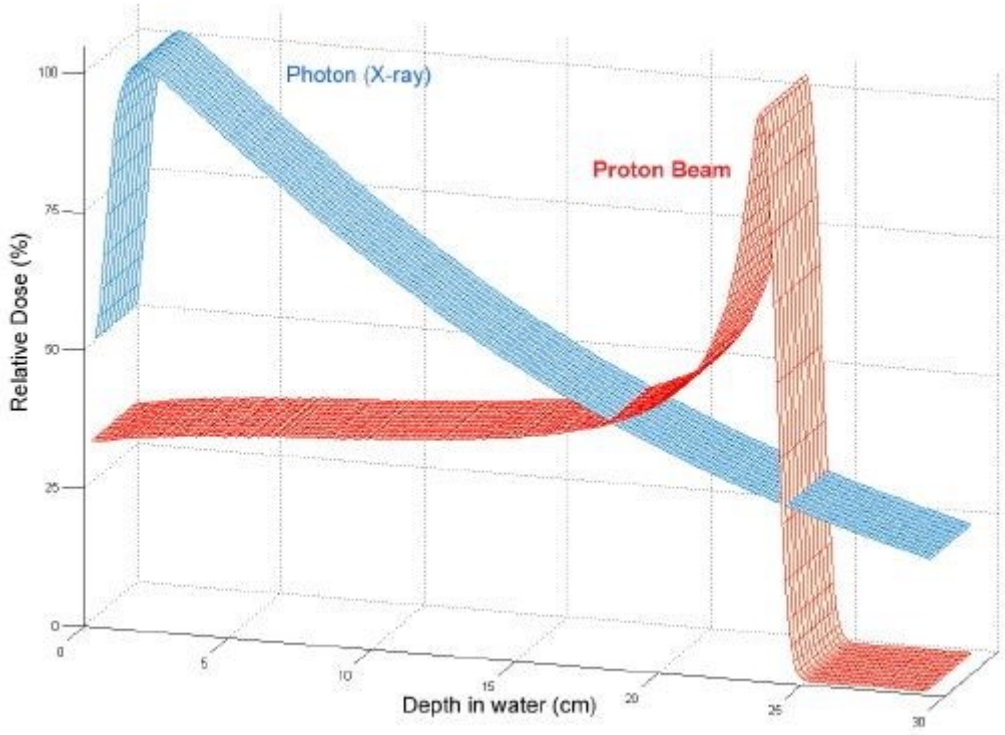

Fig. 3 Relative energy absorbed per unit mass (dose) in water for X-rays and charged particles (protons).

In the case of "light" particles, such as electrons and positrons, the energy loss in the material is a competitive process between the collision and the "deceleration radiation" known as *bremsstrahlung*:

$$\frac{dE}{dx} = \left(\frac{dE}{dx}\right)_{coll} + \left(\frac{dE}{dx}\right)_{rad}.$$

The energy loss by collision occurs conceptually in a similar manner to the case of "heavy" particles, therefore it is describable with the Bethe-Bloch formula, appropriately revised for two reasons. The first is related to the small mass of the electron (9.11×10^{-31}kg): the approximation of a straight trajectory in the interaction process, therefore, is no longer

valid. The second reason concerns the fact that electrons interact with other electrons of the target so that, in the evaluation of the total energy loss, it should be taken into account that the particles are not distinguishable. It follows that the Bethe-Bloch formula becomes:

$$-\frac{dE}{dx} = 2\pi N_a r_e^2 m_e c^2 \rho \frac{Z}{A}\frac{1}{\beta^2}\left[ln\frac{(\tau+)\tau^2}{2\left(\frac{I}{m_e c^2}\right)^2} + F(\tau) - \delta - 2\frac{C}{Z}\right].$$

Where τ is the kinetic energy of the incident particle per unit of $m_e c^2$ and F(τ) can assume two different values:

$$F(\tau) = 1 - \beta^2 + \frac{\frac{\tau^2}{8} - (2r+1)ln2}{(\tau+1)^2} \qquad \text{for electrons}$$

$$F(\tau) = 2ln2 - \frac{\beta^2}{12}\left(23 + \frac{14}{\tau+2} + \frac{10}{(\tau+2)^2} + \frac{4}{(\tau+2)^3}\right) \qquad \text{for positrons.}$$

The energy loss for *bremsstrahlung* is given from:

$$-\left(\frac{dE}{dx}\right)_{rad} = NE_0\Phi_{\mathrm{rad}}$$

where N is the number of atoms for cm^3 and:

$$\Phi_{\mathrm{rad}} = \frac{1}{\mathrm{E_0}}\int \mathrm{h\nu}\frac{\mathrm{d\sigma}}{\mathrm{d\nu}}(\mathrm{E_0}, \nu)\mathrm{d\nu}.$$

For each material a critical energy Ec is defined such that for E=Ec it will be:

$$\left(\frac{dE}{dx}\right)_{coll} = \left(\frac{dE}{dx}\right)_{rad}$$

for E>>Ec the energy loss is possible only for "deceleration radiation". In figure 4 the trend of the energy loss due to collisions and *bremsstrahlung* for electrons in a copper layer is shown.

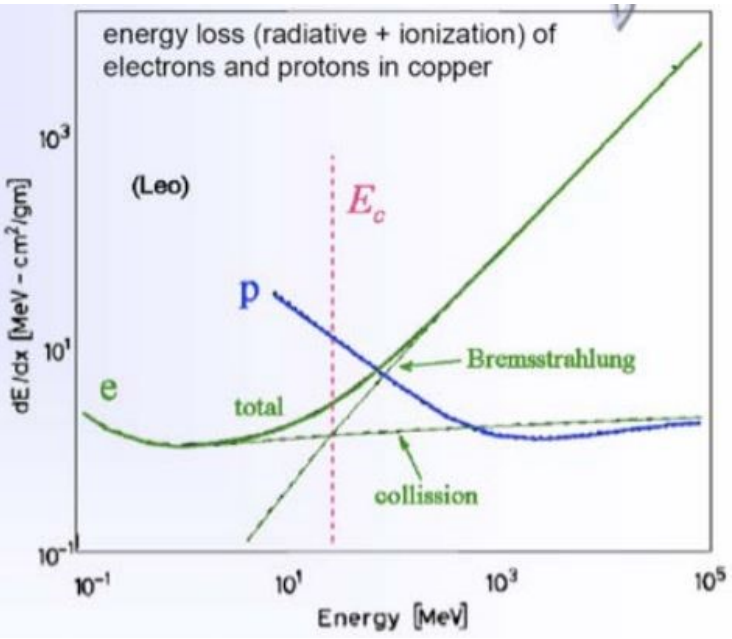

Fig. 4 Electron energy loss as a function of energy in copper for collision and bremsstrahlung.

Indirectly ionizing radiation differs from the one discussed above, since energy deposition/transfer is caused by particles with no electric charge, which in the interaction process emit particles that in turn are directly ionizing. To this category belong neutrons and photons (X-rays and γ –rays).

Neutrons cross matter until they collide with an atomic nucleus; in this case, the interaction probability is related to the cross section and the interaction effect consists in the production of charged particles or γ-rays, which can induce secondary ionizations.

The interaction can take place through different reactions:

- elastic scattering (n, n)
- inelastic scattering (n, nγ)
- transmutation (n, p), (n, α)
- radiative capture
- fission

Photons, contrary to neutrons and charged particles, in the interaction with matter are attenuated according to their energy, i.e. the beam is degraded in intensity, but not in energy. The mathematical expression that describes the attenuation in a material is of an exponential type:

$$I_{out}(x) = I_{in}e^{-\mu x}$$

Where:

$I_{out}(x)$: intensity of the photon beam outgoing the target of thickness x.

I_{in}: intensity of the incident photons beam.

μ: coefficient of linear absorption, measured in cm^{-1}, proportional to the interaction cross section.

The main interaction processes of photons with matter are:

- Rayleigh Scattering
- Auger Effect
- Photoelectric effect
- Compton Effect
- Pair production

Of these, the ones of interest for biologically relevant consequences are the photoelectric effect, the Compton effect and pair production, whose cross sections as a function of the photons energy is shown in figure 5.

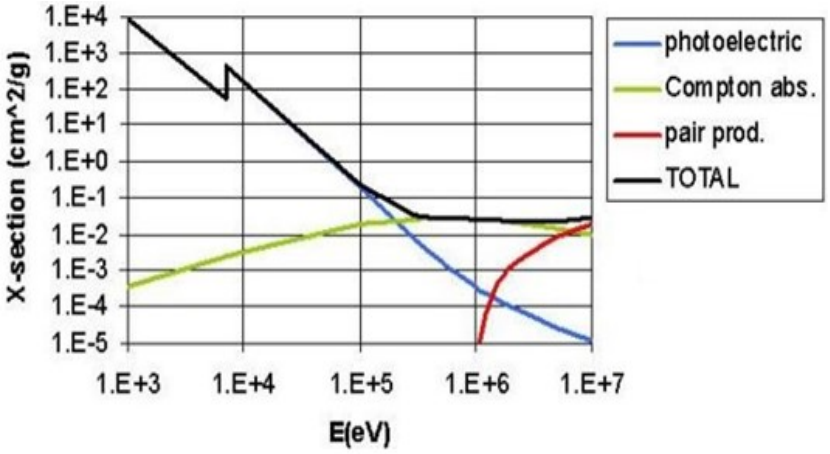

Fig. 5 Trend of the photoelectric, Compton and pair production cross sections in function of the energy of the incident photons.

Directly ionizing radiations, such as protons, α-particles etc., have a high probability to interact with matter due to their charge, so they produce ionization events close to each other (in some cases they occur so close that they can spatio-temporally overlap); therefore, they are called *densely ionizing radiation*. Photons and, in general, indirectly ionizing radiation, cause distinct and scattered ionization events; hence the name of *sparsely ionizing radiation*. Moreover, the number of ionizations produced per unit length is linked to the energy released into matter; therefore, directly ionizing radiations have usually a higher linear energy transfer value (LET) compared to indirectly ionizing radiations (figure 6). A detailed discussion of LET can be found in the Appendix A.

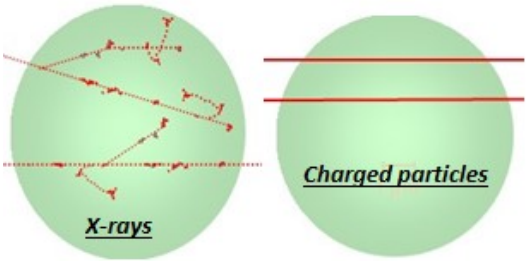

Radiation	Linear Energy Transfer (keV/μm)
Cobalt-60 γ-rays	0.2
250-kV x-rays	2.0
10-MeV protons	4.7
150-MeV proton	0.5

Fig. 6 Left: Schematization of energy deposition events for X-rays and charged particles. Right: LET values for different radiation qualities.

1.2 Biological response to ionizing radiation

The cyto-genotoxic action of ionizing radiation (IR), responsible of damages to the cell's structures that in some cases could be lethal, is well known [10]. The effects of IR on biological molecules is a consequence of the energy release during the interaction process, and are mainly due to lesions to sensitive targets within the cell, among which the DNA macromolecule stands out because it contains the genetic information and exists as a single copy.

The action on the critical target(s) can be indirect and/or direct. The indirect action occurs when the incident particles interact with molecules and atoms of the cell other than the DNA, producing highly reactive free radicals, which are known to be harmful [11]. On the contrary, direct action happens every time IR interacts directly with the biomolecules of interest, essentially the DNA. Both actions are described by the biophysical model known as target theory, which is a classical paradigm of radiation biophysics. Briefly, the theory is based on the assumption that for a cellular lethal effect to be caused, it is necessary that the sensitive target must be "hit" by IR. Initially there was no clarity as what the sensitive sites within a cell were. Subsequently, these were identified with the DNA. However, it is not sufficient for the DNA to be hit: the fate of a cell exposed to IR depends on the type of lesion its DNA incurs, as cells are able to repair IR-induced damage, at least to a certain extent. In the last couple of decades, the dogma of the DNA as the main target of IR action has been questioned, from studies on the so-called *non-targeted* effects: biological effects of IR, generally associated to energy deposition within the cell nucleus, can manifest themselves also in cells not directly exposed, or as a result of cytoplasm and/or of biomolecules different from DNA damages. This happens in cells that have received "stress" signals from irradiated cells [12-13] and/or among are descendants of initially exposed cell population, which retain a "memory" of the insult [14].

When studying the biological effects of IR another parameter to be considered is represented by the "timing"; IR-induced damage, in fact, can be influenced by the time elapsing from the irradiation. This gives rise to *acute effects* and *long-term effects* (figure 7). The acute effect manifest itself immediately or shortly after exposure (from ns

up to a few days after irradiation), involves directly irradiated cells and is defined as "deterministic", i.e. its severity is proportional to the dose and happens when the dose exceeds a threshold. The long-term effect, instead, occurs a long time after exposure (up to years), involving the progeny of the cell population directly exposed and is defined as "stochastic", i.e. probabilistic and non-dose dependent.

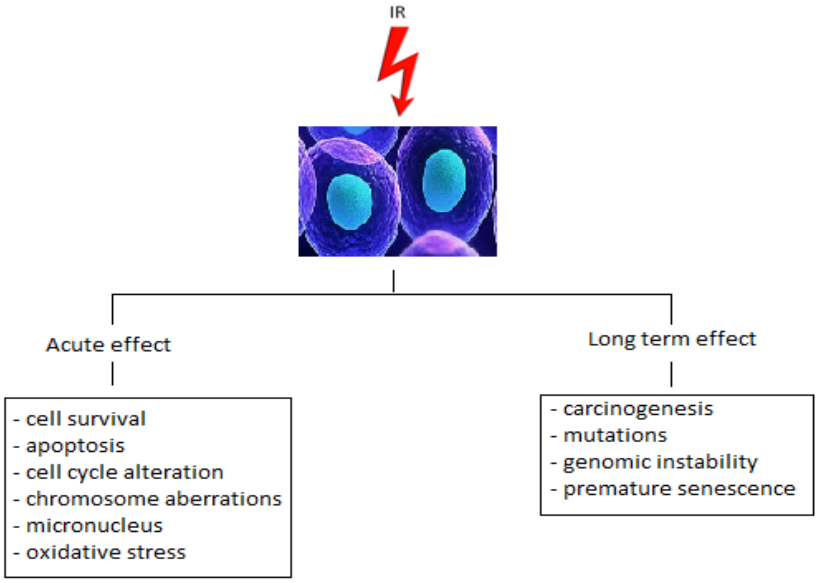

Fig. 7 A schematic representation of acute and long-term effects of ionizing radiation.

1.2.1 Cellular survival: influence of radiation quality

The study of radiobiological effects observed following exposure to IR often makes use of *in vitro* cell cultures. Depending on the dose, cells can experience different fates. The correlation between the amount of dose of IR absorbed by the cells and the lethal and/or sub-lethal effects caused by it, such as the loss or the reduction of the cells' proliferative capacity, is of great interest in the radiobiology field. Sub-lethal effects are of paramount importance since they determine the long-term consequences of IR exposure such as oncogenic transformation. On the other hand, IR-induced cell death may reverberate on acute effects. There are many modes a cell can die as a result of IR-inflicetd damage; reproductive death is one of the most comprehensively studied since it ensures that a

cell loses its ability to divide, which is essential, for example, to determine the success of radiotherapy since a tumor is cured if all its cells are killed. It is necessary consider that the response in terms of magnitude of a given biological effect as a function of dose (described by a dose-effect curve) is strictly related to the radiation quality or LET (i.e. whether it is photons or charged particles cells are exposed to). In addition, there are other biological factors that influence the extent to which cells can be killed, such as the phase of the cell cycle at which the irradiation takes place and the type of cell. The latter reflects the fact that different cell lines may have a different intrinsic radiosensitivity, which finds its equivalent *in vivo* in the inter-individual variability of the response to a given radiation, for a given dose and LET.

Puck and Marcus in the middle of last century [15-16] proposed a first interpretative model of the dose-effect relation, based on *in vitro* measurements and gave an operative definition of cell survival, that is: *every irradiated cell is considered having survived if it keeps intact its reproductive capacity, developing a colony.* The latter is defined as an agglomeration of at least fifty cells, corresponding to 5-6 cells division post-irradiation. From this assumption, after an IR exposure, from a cell culture an appropriate number of cells is inoculated at increasing numbers as radiation dose increases and, after a certain time, which varies among cell lines depending on their doubling time, the colonies or clones can be counted (figure 8).

The counted colonies will give information on how many cells survived the initial insult, and is thus possible to estimate the surviving fraction (SF) for any dose and radiation type as follows:

$$SF = \frac{counted\ colonies}{cells\ seeded * PE/100}.$$

PE is the plating efficiency, which takes into account the proliferative capacity of non-irradiated cells, to which the SF values at various doses have to be normalized.

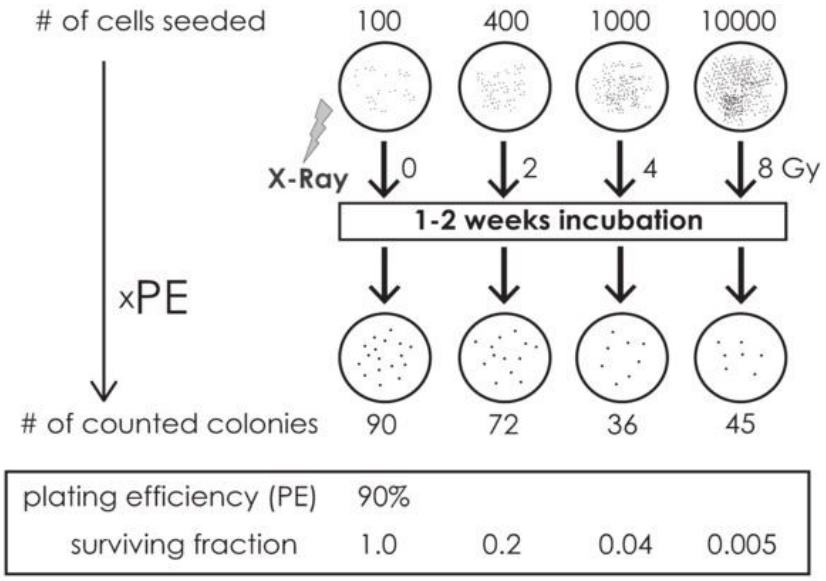

Fig. 8 Scheme of the model proposed by Puck e Marcus for the determination of the so-called clonogenic curve following exposure to IR.

Several mathematical formalisms have been developed to best fit the experimental data from the clonogenic assay that describe the cell survival trend as a function of dose; over the years the linear-quadratic model has proven to provide the best interpretation to the experimental data.

The linear-quadratic model is described by the following equation:

$$SF = e^{-\alpha D - \beta D^2}$$

SF: surviving fraction;
α: factor that models the lethal damage, proportional to the dose;
β: factor that models the sub-lethal damage, proportional to the dose square;
D: dose (Gy).

According to this model, cell death can be induced by means of a single lethal event (single intra-track event) or by the accumulation of sub-lethal events. To understand the concept that the linear component of the linear-quadratic equation is related to the lethal damage, while the quadratic component is related to the sub-lethal damage it is useful

to examine the typical survival curves obtained from cells exposed to low-LET radiation, i.e. X-rays (figure 9) and compare them with those derived from high-LET radiation. At this point, it is important to bear in mind that these two types of radiation induced DNA damage mainly by the indirect and the direct effect, respectively. The X-ray curve shows a "shoulder" at low doses (typically <1Gy), then as radiation LET increases (in the case of figure 9, alpha particles) the shoulder gradually disappears and the curve slope becomes steeper: this is interpreted as a higher efficiency in cell death induction by high-LET radiation. In fact, the greater the LET, the denser are the ionization events along the ion track and the cellular repair processes are less efficient. Hence, for densely ionizing radiations to cause lethal events a single lethal lesion is sufficient, even at low doses, along their track. This translates into a linear dependence upon dose. Conversely, sparsely ionizing radiation (low LET) can kill especially by the interaction of at least two lesions produced by independent tracks (thereby a dependence on the square of the dose), and the severity of the damage is less pronounced, particularly at low doses, which explains the shoulder reflecting sub-lethal damage being restored. The ratio between α/β is very important (in a treatment plan for example) because gives an idea of the radiosensitivity of the cell line.

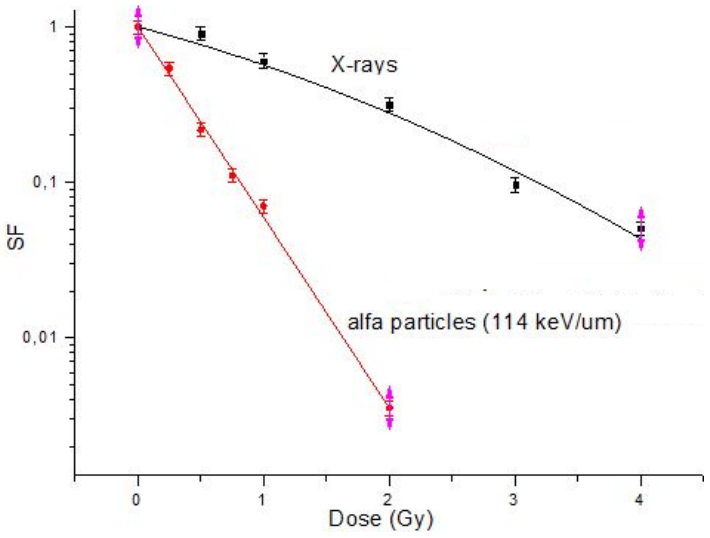

Fig. 9 Cell survival curves of X-rays (black squares) and charged particles (red dots). The X-rays curve shows the typical "shoulder" of low-LET radiation.

1.2.2 Relative biological effectiveness (RBE)

Radiations of different quality, at the same dose, usually induce a different amount of the same radiobiological effect. The biological efficiency of a given radiation is usually expressed by the concept of Relative Biological Effectiveness (RBE). This corresponds to the ratio between the dose of a reference radiation, generally X-rays (Dx), and the dose of the examined radiation (D) that elicits the same amount of damage (biologically iso-effective dose). Therefore, the RBE is defined by the following expression:

$$RBE = {}^{Dx}/_{D}$$

The RBE can be derived graphically or computed from the dose-response curves of the examined radiation and the reference one as shown in figure 10. Since the RBE is defined for a given level of damage, for instance the same amount of cell killing, its value depends on the shape of the dose response curves, and can vary according to the level of damage chosen to derive it. Therefore, given that low- and high-LET survival curves usually differ in their shapes, the RBE is greater in the low dose region because of the different trends, i.e. linear-quadratic vs linear respectively.

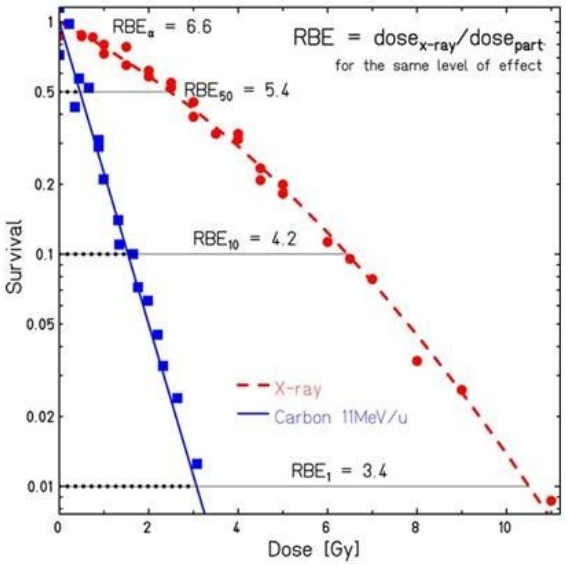

Fig. 10 Scheme of graphic evaluation of the RBE. In this case, the examined radiation is a beam of Carbon ions of 11 MeV/u and the reference radiation is X-rays, as usual.

It is interesting to analyze the trend of RBE as a function of LET. For increasing LET values, the RBE increases gradually until it reaches a maximum at about 100 keV/um (figure 11), then it rapidly decreases. The reason why this relationship peaks around that particular LET value is due to the fact that the mean distance between two ionization events is comparable to the DNA double helix diameter (2nm) for that LET value. This maximizes the probability of causing a DNA Double Strand Beak (DBS), which is the typical lethal lesion for a cell (if unrepaired or mis-repaired), therefore this translates in the highest probability of causing lethal damage (figure 12).

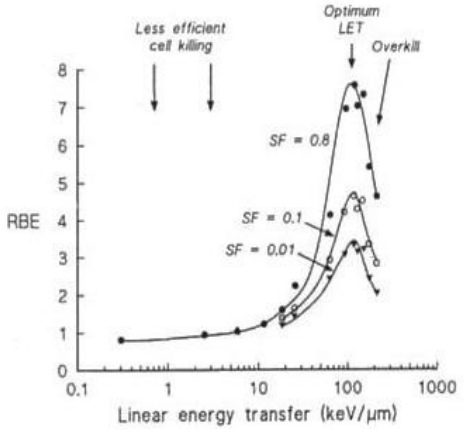

Fig. 11 Graphic illustration on the RBE as a function of LET.

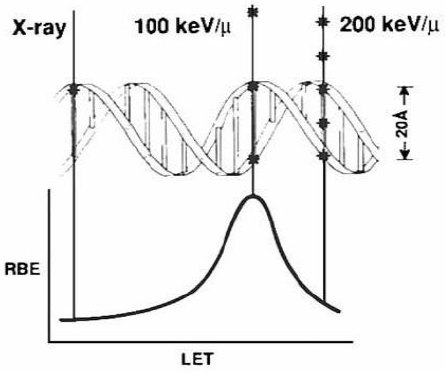

Fig. 12 Illustration of the RBE efficiency peak at the LET value of ~100keV/um. The decreasing trend after the peak is due to the so-called "overkill" effect.

1.2.3 Cellular senescence

In complex biological systems like mammals, somatic tissues contain a certain proportion of mitotic cells, i.e. cells that have a proliferative ability and are dividing. This confers to such tissues important characteristics such as repair, renewal and, sometimes, regeneration of the cells of which they are composed, which implies also a greater susceptibility to hyperproliferative diseases such as cancer. To avoid this, cells have developed several mechanisms of tumor suppression able to regulate the cellular transformation and/or uncontrolled growth. Some of these mechanisms are based on the prevention of DNA damage accumulation and/or on the optimization of repair, while others are based on the monitoring of already mutated or damaged cells that can turn into cancerous ones.

One of these mechanisms is the *cellular senescence*, which is a physiological process by which cells lose permanently their proliferative ability while remaining metabolically active. This can also occur in response to various events such as, DNA damage, oncogenic stimuli, oxidative stress, etc. Since also normal cells accumulate “errors” as they age and undergo several replication rounds, this irreversible growth arrest has been interpreted as an evolutionarily designed mechanism to prevent the damage transmission in the replication process.

Despite only recently the role of cellular senescence as a mechanism of tumor suppression has been recognized, the first definition was given in the late ‘900 [17], who showed that a primary human fibroblasts cell culture can undergo only a limited number of divisions (about 55) prior to its irreversible growth arrest. This replication limit was the first demonstration that cells can experience the so-called "replicative senescence" [18], which nowadays is known to be directly related to the shortening of the telomeres, the end-chromosome sequences that are lost at each cell division, until their length reaches a critical limit, marking the onset of senescence [19].

The identification of the pathways that regulate cellular senescence are still an open issue even if up to date the best known are those controlled by p53 and pRB, which are tumor suppressor genes.

Besides p53 and pRB, many genes undergo an alteration of their expression and several are the functional and morphological changes adopted by senescent cells. It is necessary to say that as well as the positive role of cellular senescence as a tumor suppressor, recent studies pointed out some unfavorable aspects [20]. There is evidence of a potentially harmful secretory pattern in the cellular microenvironment shown by senescent cells. The acquisition of what is called "Senescence-Associated Secretory Phenotype" (SASP), gives to senescent cells proinflammatory characteristics that have the potential to promote tumor growth. Albeit controversial, this aspect may be relevant in tissues that have a higher-than-normal number of senescent cells, as a result, for instance, of the exposure to ionizing radiation in radiotherapy. The radiation-induced senescence is generally referred to as "Stress-Induced Premature Senescence" (SIPS).

1.2.4 Stress-Induced Premature Senescence (SIPS)

Irradiated cancer cells that undergo cell death or senescence result, in both cases, in a permanent halt of tumor progression. In this case, the induction of senescence would have a positive impact representing an alternative cell death pathway to reproductive death at sub-lethal doses. However, SIPS could represent an important and unwanted side effect of ionizing radiation exposure, so far underestimated. Recently, there is a growing interest in studying SIPS in normal cells, especially because it could be induced even at very low doses of radiation, i.e. the typical doses at which healthy tissues are exposed in radiotherapy. In fact, in hadrontherapy although the radiation dose is mostly deposited within the tumor, (due to the peak-plateau ratio of the Bragg peak), healthy tissues inevitably receive a dose that is lower than that they would receive from photon/electron beams. However, such dose is not negligible and may be still able to induce cells into senescence. Thus far, not many SIPS investigations (mainly *in vitro)* have been carried out in cells and at doses of interest for hadrontherapy. The unknown role that this phenomenon can play *in vivo* opens new scenarios and strengthens the need for

more radiobiological studies due to its possible ambivalent action in tumor and surrounding healthy tissues.

The total dose to be delivered in a radiotherapy treatment plan varies depending, first of all, on the tumor type (i.e. whether it is more or less radioresistant) and also on the stage at which the tumor is treated. A typical dose for a solid epithelial tumor ranges from 60-80 Gy, while lymphomas are usually given 20-40 Gy. These doses are typically administered in fractions of about 1.8-2 Gy every 24 h. For an exhaustive overview of the radiobiological principles guiding current radiotherapy regimes [21].

In general, SIPS is a dose dependent mechanism but this is not always true and it is strictly related to the radiation quality and on the examined cell line; at higher dose values the predominant event could be clonogenic cell death while at lower doses cellular senescence, giving to senescence a dose-independent character.

SIPS appears to share the same molecular pathway(s) that lead to replicative senescence. One important difference, however, is that the senescence response induced by ionizing radiation may persist in the progeny of the initially exposed ones in the sense that more cells in time will go into senescence than would if they had not been exposed. Results from other experiments have shown that in vitro cells undergo SIPS up to one month (or more) post irradiation (depending on the cell line).

Since is known that ionizing radiation induces SIPS, in both normal and cancerous cells, after exposure to high and low doses [22] and that in tumor cells represents a positive effect in the context of cancer treatment, an important implication to understand is the rule that senescence plays as a possible mediator of tumor recurrence after radiotherapy. Furthermore, the accumulation of senescent cells as a result of SIPS induction in cells of healthy tissues could contribute to tissue degeneration and/or malfunctioning of organs.

The commonly used radiobiological test to reveal senescence makes use of affinity of senescing cells for β-galactosidase, also referred to as β-gal, which is a hydrolase enzyme that catalyzes the β-galactose hydrolysis. Senescent cells are specifically positive to β-galactosidase, a phenomenon defined as SA-βgal or Senescence-Associated β-galactosidase. The peculiarity of the latter is that it is, in principle, expressed only by

senescent cells and not from quiescent or terminally differentiated cells. SA-βgal is detectable in some cell types but not in others, for which it is necessary to use other markers of recognition, therefore is not a universal marker for senescence detection [23]. However, the cell line used in this work, human umbilical vein endothelial cells (HUVEC), was chosen because it is known to be an excellent model for SA-βgal.

1.3 Advantages of radiation therapy by charged particles: hadrontherapy

Cancer is a leading cause of death despite at the time of diagnosis more than 50% of tumors has not formed metastases yet [24]. In such cases, the tumors are potentially curable with localized therapies, such as surgery, chemotherapy and radiotherapy; often combined treatments between them are used. In 20% of the cases, the treatment modalities fail due to the inability to completely remove the tumor or to inactivate all tumor cells [25]. Hadrontherapy is a relatively new radiation treatment modality that uses beams of accelerated charged particles contrary to conventional radiotherapy treatments. In fact, conventional radiation therapy uses high-energy photons that, after the interaction with matter, release their energy in an exponentially decreasing manner, so they are useful to cure superficial tumors; furthermore, from the radiobiological point of view, at a given dose they are less effective than ion beams such as carbon.

Significant progress in the treatment of deep and/or radioresistant tumors is claimed with the hadrontherapy technique that mainly uses protons and carbon ions. Studies for the use of beams with particles of higher atomic number (Z), such as oxygen, but also of ions with a lower atomic number such as lithium [26], are ongoing. In the interaction with matter, the continuum of the ionization events, called track structure, produced by ions, is related to the particles' energy, and for a given energy, by Z. It has to be noted that even at equal/similar LET values particles with different Z can cause qualitatively and quantitatively different biological effects due to secondary ionization events, hence their track structure.

The two most important clinically relevant advantages presented by hadrontherapy compared to conventional radiotherapy are:

1. Greater ballistic accuracy in the dose release into the tumor site;
2. Higher radiobiological effectiveness (in the case of carbon ions).

The first aspect is a direct consequence of the physical nature of the energy deposition process along and around the path of ion beams in matter, described (as previously discussed in paragraph 1.1.1) by the Bragg curve. The second aspect, instead, is the result of the response of the tumor cells to ionizing radiation of different quality as seen in 1.2.1; in general charged particles of increasing Z exhibit a greater biological effectiveness, that is they can kill more cells than do photons or protons of the same dose (see the concept of RBE in 1.2.2). This allows, in principle, the use of lower doses to achieve the same percentage of inactivation of tumor cells attained by photons sparing, at the same time, healthy tissues because of the Bragg curve inverse dose-depth profile.

The ratio between the energy deposited in the Bragg peak (in clinical settings the Spread-Out Bragg Peak or SOBP) and that deposited at the beam entrance (the plateau region) can be quite high (in the order of 2 or even 3 for carbon ions) and represents the main physical rationale of the use of charged particles in tumor therapy. A problem is, however, represented by the substantial lack of detailed radiobiological data on the biological effects along the entire Bragg curve. For obvious reasons, most of the existing data concern the SOBP region (that corresponds to the tumor region) and little is known on the late effects (whether cancerous or not) that are a consequence of the exposure to regions that precede and follow the Bragg Peak. The dose released to healthy tissues is source of sub-lethal damage that, if poorly repaired and transferred to the progeny, can lead to the formation of chromosomal alterations which are, in turn, potentially carcinogenic [27-30]. Moreover, such damage can also be linked, for example, to organ function degeneration, resulting from the induction of premature cellular senescence (SIPS) rather than cancer [31], and discussed in the previous paragraph. In the future, to make the best use of these benefits, it will be necessary to try to reduce as more as possible the associated side effects (figure 13).

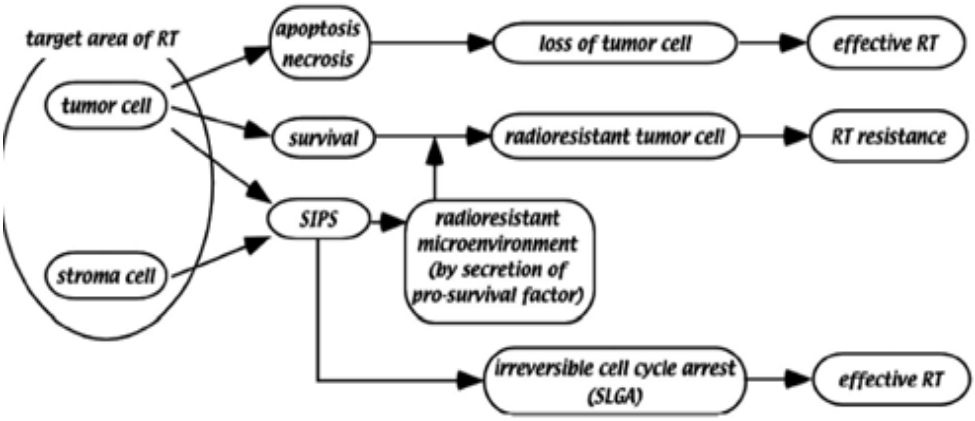

Fig. 13 Possible role(s) of SIPS in radiotherapy [31].

For these reasons, it would be desirable to be able to estimate the extent of the damage along the whole path of the charged particle beam [32], in order to evaluate the RBE changes along the entire Bragg curve. As mentioned above, the experiments are mainly done at the entrance (at the beginning of the plateau) and then into the peak or better into the Spread-Out Bragg Peak (SOBP). In fact, the Bragg peak for a mono-energetic beam is very narrow but the tumor has a volume that is necessary to irradiate as uniformly as possible. Hence, the need to produce the so-called SOBP (figure 14) by modulating the energy of the beam as to obtain a series of Bragg curves, whose convolution "broadens" the peak. Focusing mainly on the SOBP has allowed to determine the optimal dose profile for the tumor cells inactivation, but it has resulted in overlooking sub-lethal effects in the plateau region and in the region immediately behind it as well. The latter is of particular importance for carbon ion hadrontherapy because of fragmentation processes [33]. It is therefore necessary to obtain more accurate biophysical models on the effects of high-LET radiation along the whole Bragg curve, for example, through a sort of biological mapping of the Bragg curve that is a “biological Bragg curve”.

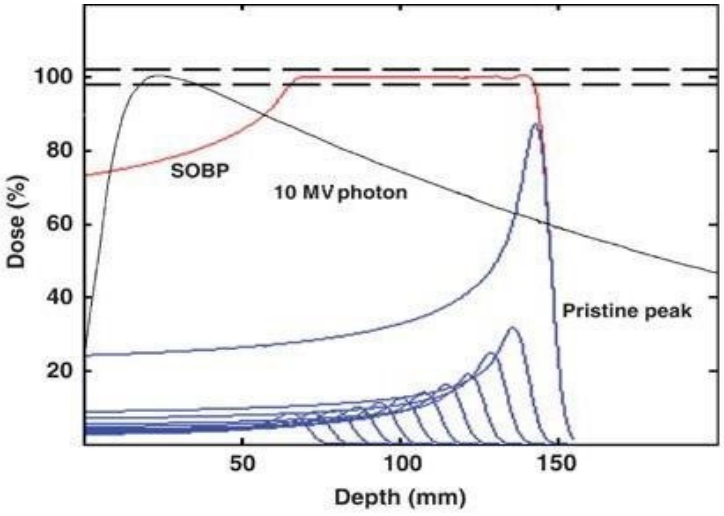

Fig. 14 The modulation of the energy of the beam to produce a SOBP can be obtained in an active or passive manner respectively either by varying the voltage at the accelerator, or using attenuators (the second one is mainly used in daily practice).

The few studies thus far carried out to this end show that there is a significant variation of radiation- induced damage along the Bragg curve, depending on the choice of the ion, on the dose and also on the examined endpoint (aberrations, micronuclei, senescence, etc.) [34]. As mentioned, an aspect not to ignore is what happens, in terms of biological effects, in the region behind the SOBP, especially for heavy ions, for which a kind of "tail" in the dose delivered exist, which is due to the fragmentation of the incident beam. Secondary ions, with a lower Z value and less energetic (hence with a higher LET) will be produced and they will stop in the healthy tissue contributing to the total dose released from the primary beam itself.

Fragmentation is a complex issue that has to be taken into account and in recent years they are performing research activities to exploit in a positive way this process. The idea comes from a technique used in Germany, and under development at INFN-LNS laboratories in Catania, that consists in an on line PET (Positron Emission Tomography) during the proton therapy sessions, called "in-beam PET" [35]. It exploits the production of β^+ ion emitters as a result of the interaction of protons with the biological material.

If carbon, oxygen etc. ion beams would be used, one would have not only the β^+ produced from the interaction of the radiation with matter, but also the β^+ produced from the fragments of the primary ions.

1.3.1 General observations on the use of charged particles in tumor therapy

The dose released to healthy tissues is the limiting factor of conventional radiotherapy as well as radiation therapy with charged particles, and finding the compromise between the curative and harmful effect of radiation is very complex. The aim of the latest photon-based radiotherapy techniques such as IMRT (Intensity Modulated Radiation Therapy, figure 15) [36] and of the hadrontherapy approach is to conform as much as possible the dose to the tumor region while minimizing the exposure of healthy tissues, but there are still some open issues that need to be urgently addressed by radiobiological studies. With the IMRT (currently the most advanced technique of therapy with photons that can be also used with protons) the tumor is irradiated with beams coming from different angles, so that their joint action converges on the target, and at the same time, the input corridors receive the dose of a single beam. With hadrontherapy, as previously discussed, the Bragg curve guarantees a ballistic accuracy of the energy release into the target, which means a high ratio between the peak-plateau in the dose delivery; this is not synonymous of a certain fully preservation of non-tumor tissues. To determine which of the two techniques is more efficient in terms of protection for the healthy tissues is particularly difficult, because, with the IMRT, the joint action into the tumor of beams coming from different directions involves the irradiation of a large region of healthy tissue but with very low dose values. On the other hand, with hadrontherapy, the region of healthy tissue that receives the insult is considerably smaller than the one irradiated with the IMRT, but the dose values are higher. Another methodology used in the clinical routine in radiotherapy treatments, always with the aim to protect healthy tissues, is to decrease the number of fractions of the treatment itself (hypofractionation).

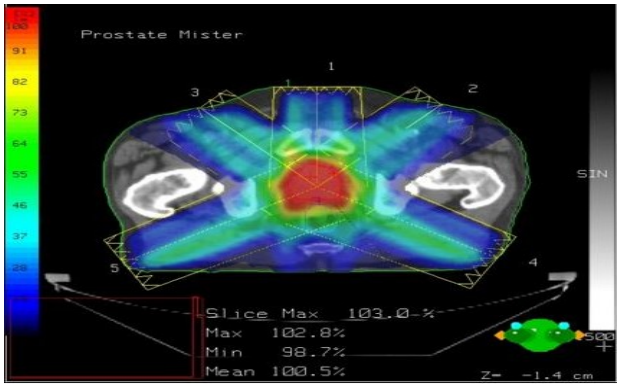

Fig. 15 Dose distribution in a typical IMRT treatment.

Finally, when looking for the right balance between the beneficial and injurious effect of radiation in cancer therapy, it has to be taken into consideration that the dose-incidence for tumor local control and the probability of complications are two sigmoids parallel to each other (figure 16).

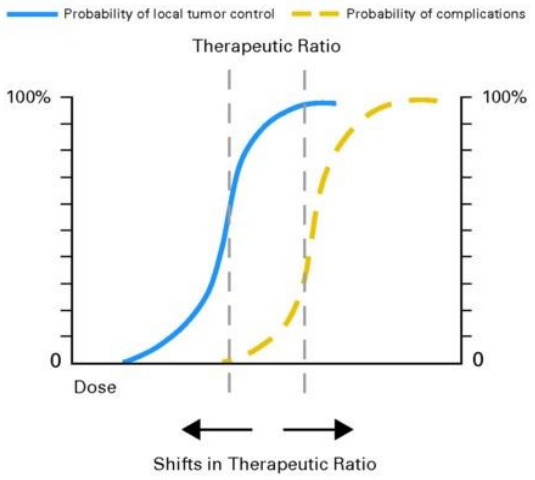

Fig. 16 Dose-incidence for tumor local control vs probability of complications.

This means that if there is a high probability of local tumor control, one will also have a high (and unacceptable) probability of damaging healthy tissues and vice versa. All this represents a major source of difficulties that experts have to deal with when programming an effective treatment plan.

Chapter 2

Laser-driven proton beams

2.1 Laser-target interaction

In the last decades, due to laser-target interaction, optical ion acceleration has become a popular topic for multidisciplinary applications and has opened new scenarios in the ion therapy framework. It has been identified as the possible future alternative to classic accelerators in the radiation therapy field, once the demanding beam characteristic and performances are met [3].

A turning point in the laser-driven acceleration research area occurred when in the year 2000 experimental campaigns demonstrated the production of multi-MeV protons obtained from the rear surface of a target after the interaction of a laser pulse with the front surface of the target itself [37-39]. Currently, with technological improvements, laser-driven beams can reach energies of around a hundred MeV [40]. Moreover, the peculiar properties of these beams necessitate a focused research activity to develop new instrumentation and dedicated methodologies for beam handling in terms of transport, delivery and dosimetry. All these requirements are mandatory to perform radiobiology experiments, which in turn are an essential prerequisite to any possible future clinical use of laser-driven beams [41].

In general, one refers to ion acceleration produced from laser-target interaction as “laser-driven ion beam”, but this is not a completely appropriate manner to define such a process since ions cannot be accelerated directly in an efficient way due to their high atomic number. Therefore, a laser-driven ion beam is the result of a double stage acceleration that begins with a direct acceleration of electrons, produced in the laser-target interaction, which in turn, by means of charge separation give rise to an electrostatic field that generates ions and is responsible for their acceleration [42].

The whole ion production and acceleration process starts with the interaction of a high-power *(*of intensity $I > 10^{18}\ W/cm^2$*)* and sub-nanosecond pulsed laser with a solid target. In this framework, great progress was made in the '80s when the chirped pulse amplification (CPA) technique was first introduced. The CPA process (discussed in detail in paragraph 2.1.1) through a stretched in time amplification and compression of the pulse, enables the production of an ultra-short and ultra-intense laser pulse starting from an ultra-short but low-intensity pulse [43-44]. The interaction of a highly intense laser pulse with matter is able to match and exceed the binding energy of a given electron in its atom and gives rise to the target ionization forming a plasma. The ejected electrons will acquire a kinetic energy greater than their rest mass and they become highly relativistic. It is useful to introduce the *laser strength parameter* (a_0):

$$a_0 = \frac{eA}{m_e c^2}.$$

It represents the peak value of the laser potential vector (A) normalized with respect to the electron rest mass (m_e). It can be related to the peak intensity (I_L) and the laser wavelength (λ_L) by means of the following formula:

$$a_0 = \frac{e}{m_e c^2}\sqrt{I_L \lambda_L \frac{2}{\pi c}}.$$

where a_0 is the maximum momentum of an electron quivering in the laser field (it can also be seen as the electric field amplitude) and it reaches a relativistic regime for laser intensity $I > 10^{18}\ W/cm^2$.

When a laser pulse with optical or near infrared frequency ω_L is focused on a gas, the produced plasma has an electron density n_e (which determines the plasma oscillation frequency ω_p) lower than the critical density, n_c with:

$$\omega_L = \frac{2\pi c}{\lambda}, \qquad n_c = {m_e \omega_L^2}/{4\pi e^2}.$$

In the case of $n_e < n_c$ we are in the *under-dense* region and the electromagnetic wave is able to propagate through the plasma.

The context of laser-solid target interaction is a completely different scenario (compared to the laser-gas interaction) since the electromagnetic wave immediately ionizes the

target forming a plasma in which $n_e > n_c$; the laser pulse cannot propagate into solid density materials and we are in the so-called *over-dense* region. The laser pulse can only propagate into the target's skin layer $l_{sd} = c/\omega_p = (\lambda/2\pi)\sqrt{n_c/n_e}$ and the interaction is therefore a surface interaction. In the latter process part of the laser light is reflected, while a significant percentage of the laser energy is absorbed by the target and transported by energetic fast electrons [45]. Several energy absorption mechanisms are described in literature [46-47]; the overall definition is given by the Vlasov-Maxwell system of equations based on the use of a self-consistent collective field created by the charged plasma particles [48].

In the case of laser-target interaction of short laser pulses with relativistic intensities, the plasma temperature rises quickly and collisions can be considered ineffective.

Different collision-less processes, such as the *resonance absorption* effect, in which the electromagnetic field excites a large amplitude plasma wave, can absorb laser radiation. The energy transfer to the plasma then damps the effect.

The laser energy absorbed from the target and then transported by electrons is a phenomena of fundamental importance in laser-ion acceleration. In fact, whatever possible energy absorption mechanism is considered, it will surely result in the heating of electrons at temperatures considerably higher than the initial bulk temperature, and will influence their path. If normal laser-target incidence is considered, "hot electrons" that are able to cross the target and distribute on its rear surface, are pushed inward by the *ponderomotive force* (discussed in detail in paragraph 2.1.2) creating a charge separation, which produces an electrostatic field that is then experienced by ions. Thus far, the highest proton energies with the best characteristics have been theoretically explained and experimentally obtained by the so-called Target Normal Sheath Acceleration (TNSA) mechanism [49] (discussed in detail in paragraph 2.2).

2.1.1 Chirped-pulse amplification (CPA)

The ion production and acceleration process originates from the interaction of ultra-intense $I > 10^{18} W/cm^2$ and ultra-short (*ps to fs*) laser pulses with solid targets. The key in reaching such high powers starting from short but lower power laser shots is

the chirped pulse amplification (CPA) technique originally introduced as a method to increase the available radars power in the '60s [50]. In the mid '80s G. Mourou and D. Strickland of the University of Rochester (USA) discovered that this technique could be applied in the optical domain with revolutionary consequences for laser science technology in research facilities and universities, as well as numerous lower power scientific and industrial applications [37]. CPA is the predominant technique in the production of high-peak power lasers, through the amplification of very short laser pulses, producing energies previously available only from long-pulse lasers. Nowadays it is the state-of-the-art methodology used by the highest power lasers facilities (from TW to PW) in the world (figure 17).

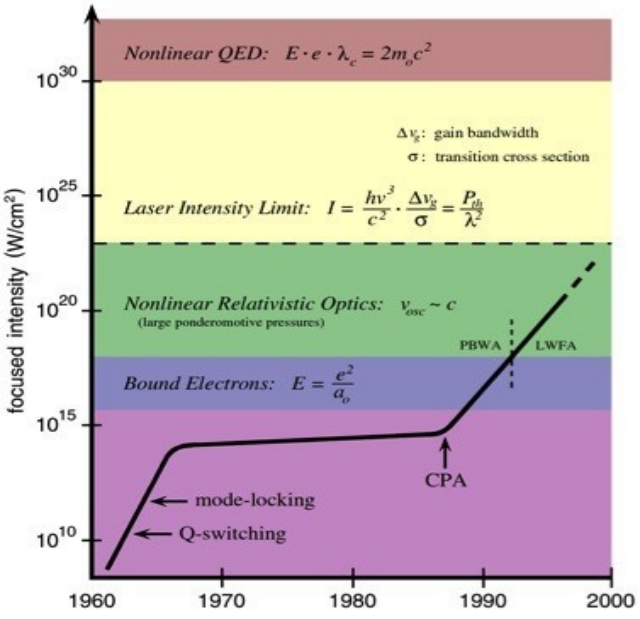

Fig. 17 Laser intensity values as a function of technological improvements in time.

The idea of CPA is simple and consists in manipulating an ultra-short pulse in a controllable and reversible manner. It is known that the intensity limits associated with optical damage for standard reflective and diffractive optical components are orders of magnitude greater than those associated with nonlinear effects and damage in transmission through a laser amplifier. If it is possible to amplify an ultra-short laser pulse keeping the pulse duration close to the original, it becomes then possible to bypass the

damage limitations of laser amplifiers and scale the short-pulse lasers to extreme peak powers.

The CPA methodology consists of three phases: stretching, amplification and recompression. Figure 18 shows the overall scheme of the CPA.

Primarily, it is important to say that there are many ways to construct stretchers and compressors but a typical Ti:sapphire-based laser chirped-pulse amplifier (used in our experimental campaigns) makes use of grating-based devices.

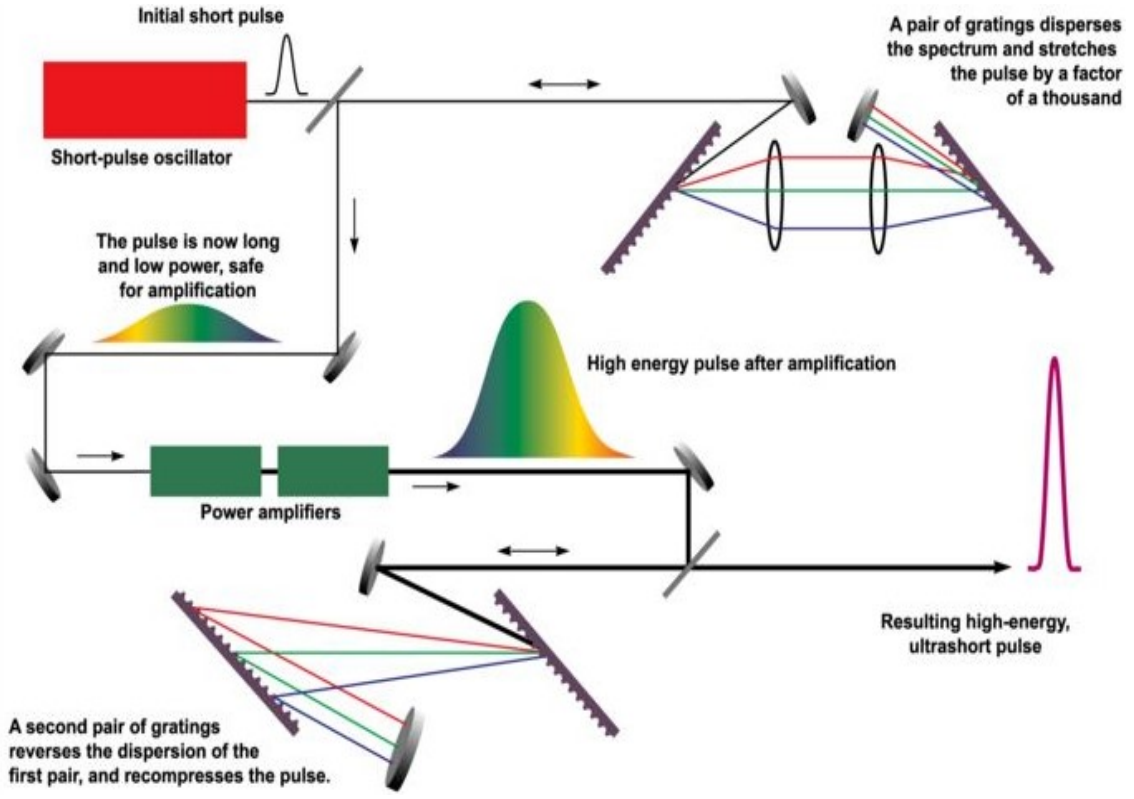

Fig. 18 Scheme of the CPA technique [51].

The first step in the CPA mechanism is the "stretch in time" of the pulse duration making use of grating-based dispersive optical system (the focusing element is a spherical or cylindrical mirror rather than lens) in which the laser pulse spectral components travel different paths according to their frequencies. The low-frequency (long-wavelength) component of the laser pulse travels a shorter path than the high-frequency

(short-wavelength) component (figure 19). This is called *positive dispersion* and the resulting pulse has a duration longer than the original one. This process produces a *chirped* in frequency laser pulse, i.e. the frequency varies between the front and tail of it and leads to an elongation (stretching) of the pulse and a corresponding reduction of the electromagnetic field amplitude. This allows an efficient and safe amplification in the second stage.

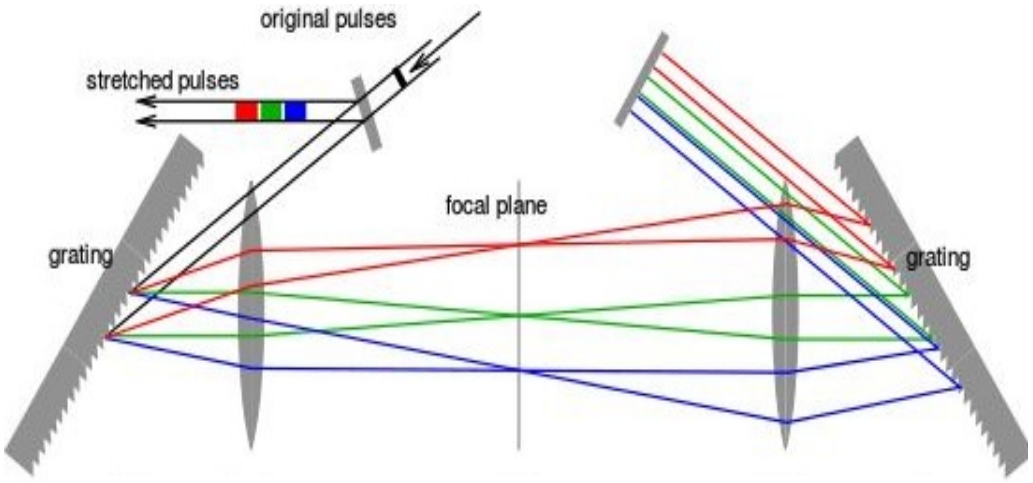

Fig. 19 Scheme of the CPA "stretching in time" element. The pulse wavelength component values decrease from the red to the blue lines [51].

The second stage consists in the pulse amplification by means of a "gain medium" that amplifies the pulse by a factor of 10^6 or more. The "gain medium" could be, for example, a crystal to which appropriate energy is supplied.

The third and last stage is the recompression of the amplified laser pulse that is obtained by means of a simplest grating-based optical configuration (compared to the "stretching" one), where low-frequency (long-wavelength) components travel a larger distance than the high-frequency (short-wavelength) components; this is called *negative dispersion*, (figure 20). After the CPA process the pulse is amplified to appropriate intensities and ready to interact with solid targets for proton production and acceleration.

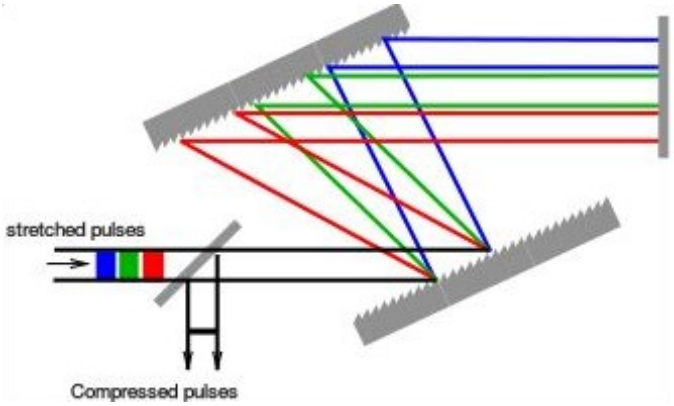

Fig. 20 Scheme of the CPA "compressor" element. The pulse wavelength component values decrease from the red lines to the blue lines [51].

2.1.2 The ponderomotive force

The laser interaction with a solid target yields to its ionization. Due to the high intensities ($I > 10^{18} W/cm^2$) of the laser pulse the ejected electrons will dispose in a relativistic configuration. The resulting (typically Gaussian-like) electric field distribution in space in all three dimensions, in a relativistic regime, causes the occurrence of an additional force called *ponderomotive force,* which leads to charge separation and permanent heating of the electrons; its idea was first introduced in 1900 [52].

To briefly describe and understand this force we will start from the non-relativistic ($v \ll c$) case [53], in which the equation of motion obtained from the Lorentz force is:

$$\frac{\delta v_x}{\delta t} - \frac{e}{m_e} E_x(r).$$

Considering the electromagnetic wave propagating in the z direction and the electric field oscillating in the x direction with a radial intensity dependency, if one uses the Taylor expansion of the electric field:

$$E_x(r) = E_0(x)\cos(\omega_l t - kx) + x\frac{\delta E_0(x)}{\delta x}\cos(\omega_L t - kx)$$

with ω_L = laser oscillation frequency, we have the plain wave solution at the first order and a fast oscillation term at the second order. Its form is:

$$\frac{\delta v_x(2)}{\delta t} = -\frac{e^2}{m_e^2 \omega_L^2} E_0 \frac{\delta E_0(x)}{\delta x} cos^2(\omega_L t - kx).$$

The *ponderomotive force* f_p on a given electron, when multiplying by m_e and taking into account the cycle-average, is:

$$f_p = -\frac{e^2}{4m_e \omega_L^2} \frac{\delta E_0^2}{\delta x}.$$

The latter can be expressed as the spatial derivative of a potential $f_p = -\nabla \Phi_p$, with $\Phi_p = \frac{m_e c^2}{4\gamma^2} a_0^2$ the *ponderomotive potential* of a laser field (with γ the relativistic factor and a_0 the electric field amplitude, the latter defined in 2.1). The relation between f_p and m_e shows that the *ponderomotive force* mainly acts on electrons, and if we consider the ion mass m_i instead of the electron mass m_e, it becomes negligible. As mentioned above (paragraph 2.1), at first ions are not accelerated (due to their high mass) and only electrons are; then, via charge separation, they lead to ion acceleration [54]. This non-relativistic calculation disregards the magnetic field action; therefore, electrons are consequently driven out of the laser focus under a 90° angle with respect to the laser propagation direction. When taking into account the magnetic field component and considering relativistic intensities, electrons experience an additional forward boost. To achieve the *ponderomotive force* in the relativistic case, the Lorentz force can be written in terms of a potential vector A and the electron motion can be divided in two parts taking into consideration the different temporal scales: p_s and p_f are the slow and fast components of the electron momentum, respectively. The relativistically correct solution is [55]:

$$f_p = m_e c^2 \nabla \frac{\delta \gamma}{\delta t},$$

with $\frac{\delta\gamma}{\delta t} = \sqrt{1 + a_0^2/2}$ the time-averaged relativistic factor for linearly polarized light over one laser cycle. The circularly polarized light solution is similar except that a_0^2 replaces $a_0^2/2$. Solving the equation of motion for electrons is possible only numerically, while the final kinetic energy W_p and propagation angle Θ, which is relative to the laser propagation direction, can be calculated as follows:

$$W_p = \left(\frac{\delta\gamma}{\delta t} - 1\right) m_e c^2 \quad \& \quad tan^2(\theta) = \frac{2}{\frac{\delta\gamma}{\delta t} - 1}.$$

These equations show a direct relation between the electron angle and the ejection energy, as also confirmed by experimental results [38].

2.2 Target Normal Sheath Acceleration (TNSA) mechanism and scaling laws

Over the last decade, a remarkable experimental work was dedicated to the development and optimization of laser-driven proton acceleration. Most of the work was carried out studying and trying to improve the so-called Target Normal Sheath Acceleration (TNSA) mechanism since it is the predominant rear surface ion acceleration regime achieved by the interaction of lasers with intensities up to $10^{21}\, W/cm^2$ with thin targets [42].

The TNSA process can be described as composed of 4 phases, schematically represented in figure 21 [56].

In the first phase **(a),** a pre-plasma is generated on the target front surface by the pre-pulse (due to the stretched and amplified part of the pulse not recompressed in the CPA process), before the main pulse arrives.

In the second phase **(b),** the main pulse interacts with the pre-plasma and propagates up to the critical surface; in the *over-dense* region the pulse can propagate only in the skin layer of the target due to the electron density (n_e) being greater than the critical density (n_c).

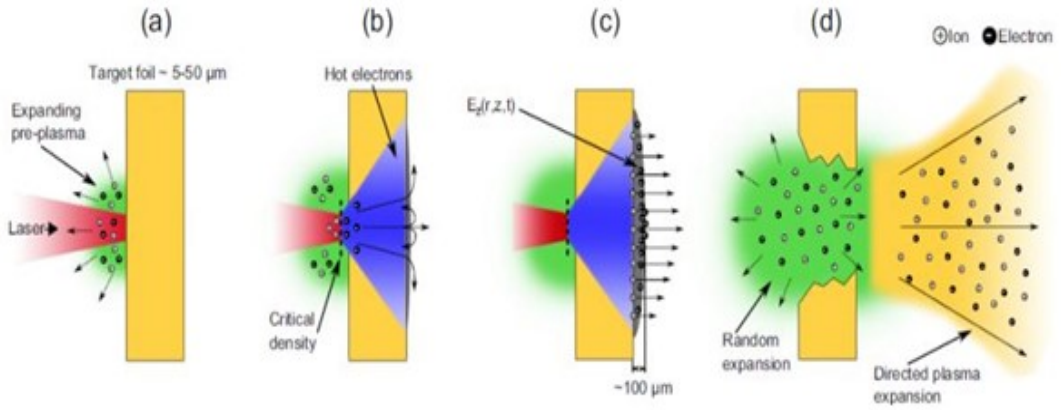

Fig. 21 Schematic description of the TNSA mechanism.

The relativistic electrons, generated from the interaction of the main pulse with the target, absorb a consistent percentage of the laser energy that causes their heating. "Hot electrons" have a mean free path larger than the target thickness, hence they start to expand across it. Through a divergence angle electrons are transported into the target and they reach the rear surface forming a cloud of dense electron sheath. The strong electric field that is in the order of TV/m generated by the charge separation (due to the *ponderomotive force*) is able to ionize atoms at the rear side; protons can be present either as surface contaminants or as target components **(c).**

Ions, still due to the strong electric field, are accelerated in the target normal direction. After the acceleration process is over, the target, disrupts in the order of *ns* **(d).**

The higher laser-driven proton beam energies so far reached (of around 70 MeV) were obtained in the TNSA regime [57]. The real limiting factor of the maximum achievable ion energy is the available laser intensities. Studies report intensities of the order of $10^{22}\ W/cm^2$, but in practice the maximum on-target intensity achieved in experiments so far is ~$10^{21} W/cm^2$ [58]. The next generation laser facilities will allow higher intensities than this value, hence paving the way towards higher ion energies.

Several studies were dedicated to determine scaling laws in order to speculate about the possible maximum energy of laser-driven protons as a function of the irradiating pulse parameters. These studies, performed in different facilities worldwide, are based on

experimental results that are mandatory for the implementation of future technologies. The collected data from the TNSA proton acceleration experiments analysis report the maximum energy values, E_{max}, as a function of the irradiance parameter $I\lambda^2(Wcm^{-2}\mu m^2)$, with I the laser intensity and λ the laser wavelength. Furthermore, the existing data suggest for the TNSA regime a scaling of $(I\lambda^2)^{1/2}$, which is valid up to values of $I\lambda^2 = 3 * 10^{20}(Wcm^{-2}\mu m^2)$ [59].

Figure 22 shows graphically the maximum proton energy obtained from laser-irradiated solid targets as a function of laser irradiance for three ranges of pulse durations (until 2008), with additional data (labeled in green "Lund" and "Saclay") reporting later experiments. Two trend lines are overlaid, the shallower one corresponding to a $(I\lambda^2)^{1/2}$ dependence, and the steeper one corresponding to $I\lambda^2$ dependence (being $(I\lambda^2)^{1/2}$ and $I\lambda^2$ dependencies related to the energy that ions acquire crossing the electron sheath). It seems that the $(I\lambda^2)^{1/2}$ scaling would lead to 200 MeV cut-off energy, which is of relevance for cancer therapy, at intensities in the order of $5 * 10^{21}\ W/cm^2$ [60].

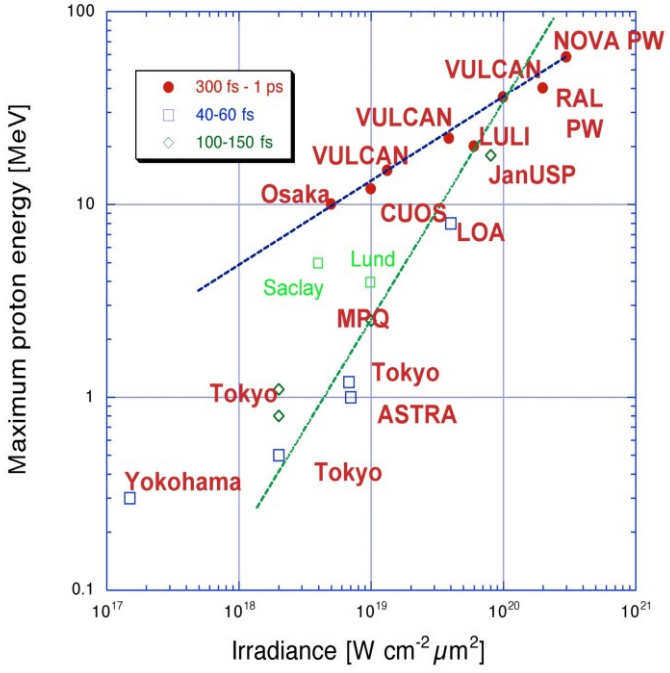

Fig.22 Maximum proton energy as a function of laser irradiance for three ranges of pulse duration is shown. Two energy trends are reported: as a function of $(I\lambda^2)^{1/2}$ (shallower), and as a function of $I\lambda^2$ (steeper).

Irradiance is not the only laser parameter playing a role in determining the maximum laser-accelerated ion energy. In fact, several secondary factors such as the thickness of solid targets can also affect the maximum energy measurable as well as the deliverable dose.

As shown in figure 23, at decreasing target thickness, the maximum proton energy increases although there is a limit (at around 8 μm) caused by the target disruption by means of the pre-pulse, previous to the main laser pulse interaction. The phenomenon is due to the different temperatures and densities reached by the electrons after the laser-target interaction. The reported example refers to an aluminum (Al) target, but other conductive materials, as gold (Au), give similar results [61].

As said, the target thickness has an influence on the proton beam dose as well. The thinner the target, the smaller the divergence angle of electrons propagating into the target and the denser the sheath that they form. The intensity of the electric field due to charge separation is higher and the percentage of produced ions, consequently, is also higher.

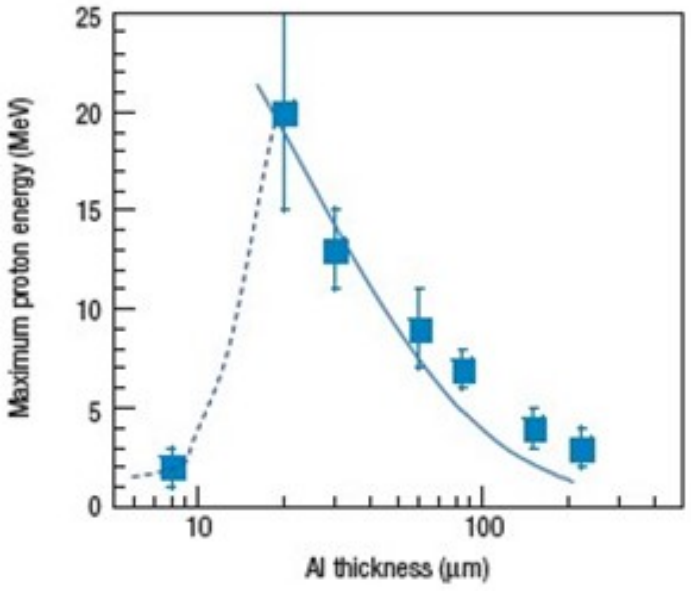

Fig.23 Maximum proton energy as a function of Al target thicknesses for protons with energy > 4 MeV, laser pulse duration of 320 fs and I ~4 × 10^{19} W/cm^{-2}; the errors are due to the shot-to-shot fluctuation and detector uncertainties [61].

2.3 Conventional accelerators versus laser-based accelerators in radiation therapy

The cyclotron was invented by Lawrence in 1932 on the principle that charged particles accelerate outwards from the center along a spiral path, while its descendant, the synchrotron, was invented by Veksler in 1944: the guiding magnetic field that bends particles into a closed path, is time-dependent, being synchronized to a particle beam of increasing kinetic energy. Since then, considerable improvements were achieved in the particle acceleration field.

In fact, there is a continuously growing interest regarding the use of such machines for a broad spectrum of applications, among which radiation therapy with charged particles emerges. The Italian state-of-the-art center for hadrontherapy treatments (being one of the most recent in terms of construction year) is the Centro Nazionale di Adronterapia Oncologica (CNAO). Its accelerator is a synchrotron consisting of an 80-meter long circle with a diameter of 25 meters (figure 24).

Fig. 24 Picture of the CNAO Synchrotron Accelerating machine.

The latter is the result of a research activity in high-energy physics based on the collaboration and cooperation principally with the Istituto Nazionale di Fisica Nucleare (INFN) laboratories but also with foreign institutes (CERN in Switzerland, GSI in Germany

and LPSC in France). The CNAO synchrotron for proton treatment reaches an energy of ~250 MeV, thus being able to cure deep tumors [62]. It is important to underline that although there was plenty of scientific documentation regarding the running regimes of conventional accelerators machines provided by other active facilities worldwide, several years were necessary to reach the reliability of the beams produced from the CNAO synchrotron. In particular, of fundamental importance was the radiobiological validation of the accelerator. The construction of the center started in the early 2000 and the first patients were treated with protons in 2011 [63]. The current CNAO therapeutic proton dose SOBP (paragraph 1.3) profile and LET (appendix A) profile are shown in figure 25.

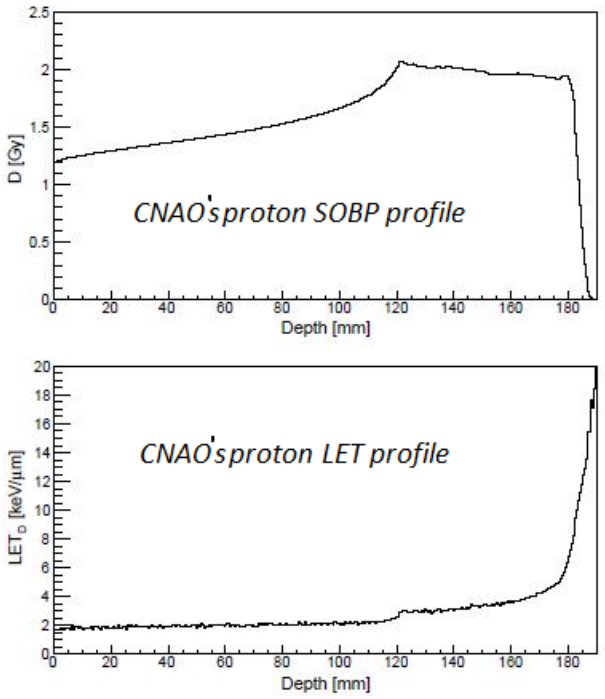

Fig. 25 CNAO proton dose vs depth SOBP profile and LET vs depth profile obtained by Fluka simulations are shown (courtesy of M. Ciocca and A. Mairani, CNAO Foundation).

Currently, there are 42 operative hadrontherapy centers worldwide, even though this kind of treatment is preferable for a remarkable percentage of cancer patients (≥ 30%). The factor that limits a large-scale diffusion of these facilities is the high installation and managing costs that could be higher than 200M€, and the requirement of huge spaces to

install the accelerator, the beam transport and delivery system. New technologies aim to investigate innovative solutions and the laser-driven methodology is a promising candidate due to the relatively small size of the laser ion accelerator associated with lower overall expenses. This would make hadrontherapy treatment more accessible for medical centers, and consequently, for patients. In view of laser-based medical facilities, one possible solution is to replace only the conventional accelerator component with the laser-driven element, while keeping the whole transport and delivery system (for example, the magnets for beam deflection) as much as possible intact. Albeit easy to implement, this is not a completely satisfactory solution. The desirable configuration would have all the components needed for beam transport and deflection replaced by optical systems, able to direct the laser beam into the treatment room where the laser-target interaction occurs and, as a consequence, the proton beam is produced. This challenging scenario would significantly reduce the overall space and costs needed for tumor treatment [64]. The issue is that clinically amenable laser-driven proton beams require specific constraints to be met, such as beam reproducibility, homogeneity and stability that can be envisaged to be difficult to achieve by laser-driven ion beams due to their intrinsic characteristics. Therefore, a major technological effort is to be able to achieve an acceptable level in the ion beam parameters by means of sophisticated transport, delivery and dosimetry systems. To make the proposed solution a realistic one in terms of its medical applications, studies must be conducted in the radiobiological field in order to assess the effectiveness of these beams. The ultra-short and ultra-intense nature of the laser-target interaction gives rise to proton bursts of ultra-high dose rates ($\geq 10^9\ Gy/s$), several orders of magnitude larger than the ones used in the conventional therapeutic working regimes. There are two main concerns regarding the use of laser-driven beams in radiation therapy: the ability to control such peculiar beam features from the dosimetry point of view and understanding the possible cellular effects they can cause due to their peculiar nature. As for the latter, it is not yet clear how the extreme spatio-temporal nature of the laser-driven particle beams can affect the biological response, since this is related to the physical pattern of the energy deposition [5-6].

Chapter 3

First experimental campaign

3.1 The ELIMED project within the ELIMAIA framework

The acronym ELIMED stands for MEDical applications at ELI-Beamlines, which in turn stands for Extreme Light Infrastructure (ELI). The latter is part of the European Strategy Forum for Research Infrastructures (ESFRI) scientific plan to build a network of new generation research facilities and, in particular, to create the latest laser equipment in the world. The aim is to accomplish innovative research activities in several fields of fundamental and applied physics and implement the existing projects regarding the interaction of light with matter to achieve laser intensities 10 times higher than currently achievable values [65]. ELI will provide ultra-short laser pulses of femtosecond duration (10-15 fs) and give performance up to 10 PW. It will host the most intense worldwide laser that is expected to bring innovation in different scientific areas, developing interdisciplinary research opportunities, among which new techniques for radiotherapy and diagnostic emerge. Therefore, the ELIMED project has a relevant role in the whole ELI framework, which involves many European countries with the main facilities being hosted in the Czech Republic, Hungary and Romania, and its purpose is the development of the most advanced instrumentation, technologies and methodologies for dosimetry and radiobiology in order to develop an hadrontherapy facility based on laser-driven beams accelerated at the ELI-Beamlines laser facility in the Czech Republic.

Dolní Břežany municipality in the Central Bohemia region, near Prague, was selected as a convenient location for the most intense laser in the world with laser intensities of about 10^{23} W/cm^2 with a proton beam energy range between 10^2-10^3 MeV. Presently at an advanced point of construction, it is the pillar of the whole ELI consortium and is called ***ELI-Beamlines*** (figure 26). This facility will mainly focus on the development of short-pulse secondary sources of particle radiation, and on their multidisciplinary applications in molecular, biomedical and material sciences, physics of dense plasmas, warm dense

matter and astrophysics. In addition, the structure will utilize its high-power, high-repetition rate lasers to perform studies in the physics of exotic plasma.

Fig. 26 Picture of the ELI-Beamlines facility.

The second research facility, ***ELI-Attosecond Light Pulse Source*** (ELI-ALPS), is under construction in Szeged, Hungary. This facility will provide users in the field of scientific research and industrial applications with the possibility of using primary laser pulses in conjunction with an impressive array of synchronized secondary light and particle pulses. Among the outstanding characteristics of the facility is the ability to supply light sources with frequencies in the range of 10^{12} Hz (THz) and X-rays in the range between 10^{18} -10^{19} Hz in the form of ultrashort pulses with high repetition rates. The ELI-ALPS, in general, will be dedicated to ultra-fast dynamics of electrons in the scale of attoseconds.

The ***ELI-Nuclear Physics*** (ELI-NP) will be the other pillar of the European distributed ELI infrastructure whose installation is forecasted in Magurele, Romania. This facility will be based on two main systems: a very high-intensity laser produced from two 10 PW beams coherently added to obtain intensities in the order of 10^{23}-10^{24} W/cm^2, and a beam

system that will produce highly collimated, high intensity γ radiation with tunable energy up to 20 MeV. This unique combination will enable ELI-NP to tackle a wide range of research topics in fundamental physics, nuclear physics, astrophysics, and research activities that will soon find applications in material sciences, management of nuclear materials and life sciences [65].

The above description is a general overview of the current major international project focused on the improvement of laser systems. One of the objectives of the work presented here was the preliminary implementation of the ***ELI-Beamlines*** research agenda that in the future, hopefully, will be dedicated to tumor treatment. The beam line will be called ELIMAIA (Extreme Light Infrastructure Multidisciplinary Application of laser-Ion Acceleration). An experimental hall of the ELI-Beamline building has already been assigned to the development and realization of the ELIMAIA transport beamline and will be available for users interested in studying the suitability of laser-driven ions in different fields, including obviously the already mentioned clinical applications [66]. Figure 27 shows a scheme of the laser building and the hall dedicated to ELIMAIA.

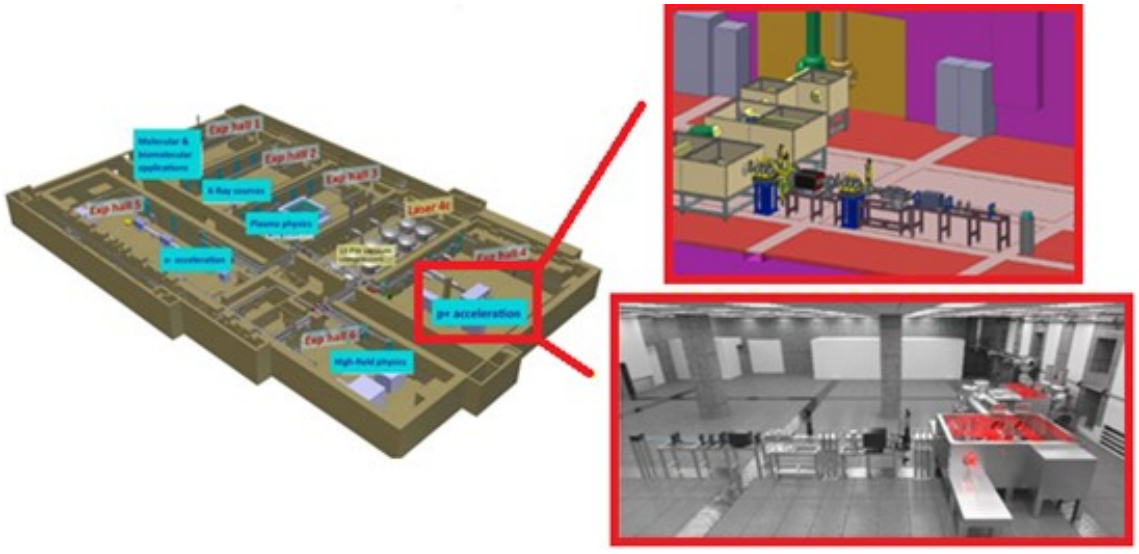

Fig. 27 Left: schematic layout of the ELI-Beamlines laser building. Top right: Scheme of the ELIMAIA beamline. Bottom right: picture of the current beamline status.

In 2013, the Italian National Institute for Nuclear Physics (INFN) funded a three-year project called PLASMAMED (Proton LASer-driven beam transport, diagnostic and Multidisciplinary Applications), which became the Italian pillar of the pan-European ELI consortium as far as medical applications are concerned., i.e. ELIMED. The development of the ELIMED/PLASMAMED was articulated in several Work Packages (WPs) foreseeing four stages.

The *preliminary phase (2013-2016)* during which the facility is being realized and no laser-driven beam is available at ELI-Beamlines is ending. This represented a crucial period since the prototype of the beam transport, selection and delivery system had to be designed, constructed and tested. Preliminary experimental runs have been conducted at regular particle accelerator facilities as well as available, lower intensity laser facilities. The latter had the scope of providing actual laser-driven proton beams: albeit with lasers of physical characteristics order of magnitude lower than the envisaged ELI-Beamlines ones, their role was deemed essential for proof-of-principal experiments such as testing of detectors and radiobiological studies in conditions other than those usually experienced at conventional particle accelerators and current hadrontherapy regimes.

In *phase 1 (2016-2017)* the first laser shots are programmed for the production of protons in the range of 20-30 MeV. If everything proceeds as scheduled, the energy selection system will be installed in the transport line and the related dosimetry studies will begin.

In *phase 2 (2017-2019)* proton beams up to 60 MeV are expected after the laser-target interaction.

In *Phase 3 (2020)* proton beams with a maximum energy of 1 GeV are expected and the transport, selection and dosimetry systems will be up and running so that radiobiological experiments can be performed for the first time under the most extreme conditions ever achieved in the field of laser particle acceleration.

Figure 28 is a summary of the laser and laser-driven proton beam characteristics expected in the various phases [67].

	Phase 1	Phase 2	Phase 3
Focused intensity [W/cm^2]	$10^{19} - 5 \cdot 10^{21}$	$5 \cdot 10^{19} - 10^{23}$	$5 \cdot 10^{19} - 10^{23}$
Energy range [MeV]	20 - 30	60 - 200	100 - 1000
No particle per shot	$10^{9} - 10^{10}$	$10^{10} - 10^{11}$	$10^{11} - 10^{12}$
Bunch duration [nsec]	1	0.1 - 1	< 0.1
Protons per pulse after the beam transport	$5 \cdot 10^{8} - 5 \cdot 10^{10}$	$5 \cdot 10^{9} - 5 \cdot 10^{10}$	$\sim 10^{11}$
Energy spread	±5%	±5%	not still defined
Proton dose per shot to the cells	0.1 - 1 Gy	0.06 - 0.6 Gy	~ 7 Gy per shot

Fig. 28 Synopsis of laser and laser-driven proton properties expected over the years.

The scientific activity has been divided in three WPs, each in turn divided into sub-WPs. WP-1 is dedicated to the target choice and optimization and beam handling in terms of energy selection and beam transport. WP-2 is focused on the beam diagnostics while WP-3 (the one in which the Radiation Biophysics Group of the Physics Department, University of Naples Federico II is involved) is dedicated to the beam dosimetry and to radiobiology experiments.

The proton beam transport system starts where the proton production (target area) occurs and extends up to the sample irradiation position. It serves the purpose to render the laser-accelerated beam feasible for clinical application so that all the physical constraints are met (such as beam homogeneity and stability as for energy and dose). Preliminary tests (performed in collaboration with the LNS-INFN group and discussed in paragraph 3.2.2) allowed to achieve a configuration based on two main modular elements, which are the focusing system, for protons transmission efficiency optimization, and the energy selector system. Figure 29 shows the current configuration of the ELIMED beamline assembly starting with the laser-target interaction area, passing through the focusing system and then through the energy selector system until the sample irradiation point downstream.

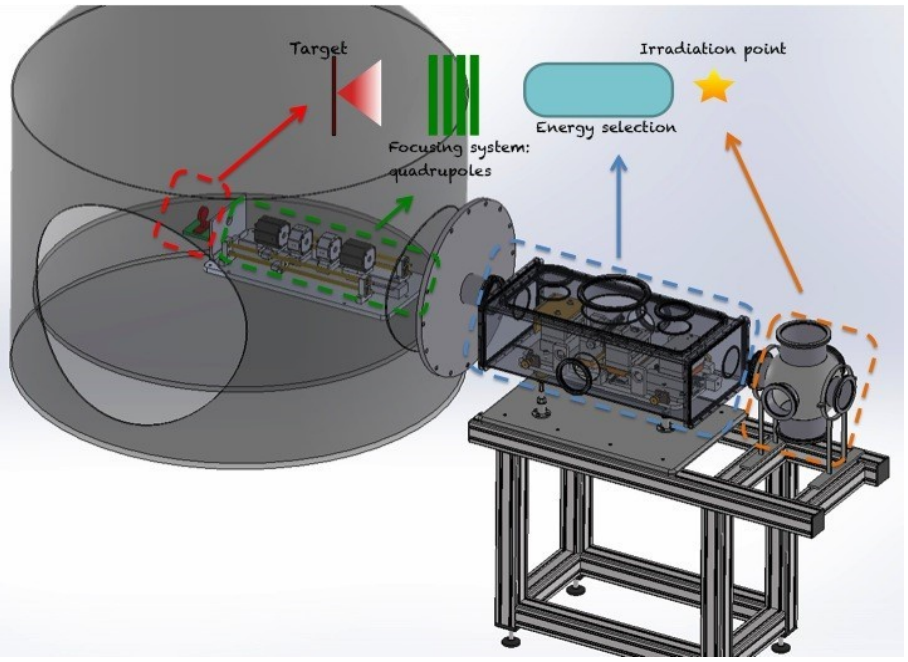

Fig. 29 Prototype of the ELIMED beamline assembly.

3.2 The Energy Selector System (ESS)

The energy selection of a laser-driven proton beam represents a critical process of the entire beam transport and is fundamental to make these beams suitable for clinical applications.

Optically accelerated ion beams are characterized by high intensities, various ion species with different charge states, broad energy spectrum and angular, energy-dependent, distributions. Therefore, to use these beams for multidisciplinary purposes, it is necessary to control the beam energy and angular distribution as well as to render reproducible the fluence over the irradiated area. Moreover, accurate and reliable dosimetry measurements are mandatory for radiobiological pre-clinical studies.

The energy selector system (ESS) was developed in Catania at the Laboratori Nazionali del Sud (LNS-INFN), leader of the ELIMED/PLASMAMED collaboration, and tested in different facilities and experimental campaigns in which we were active participants.

The ESS consists of a sequence of four magnet dipoles with alternating polarities [68-70]; it act as a bunch compressor [71, 72]. The two external dipoles have an opposite polarity compared to the two central ones. Thanks to the magnetic field action in each dipole, spatial separation of charged particles with different energies is provided. The dipole sequence, combined with a slit device placed in the middle of the magnetic system, separates and selects protons within an energy range. Figure 30 shows a scheme of the ESS and gives an idea of its functioning by illustrating the magnetic field profile [70].

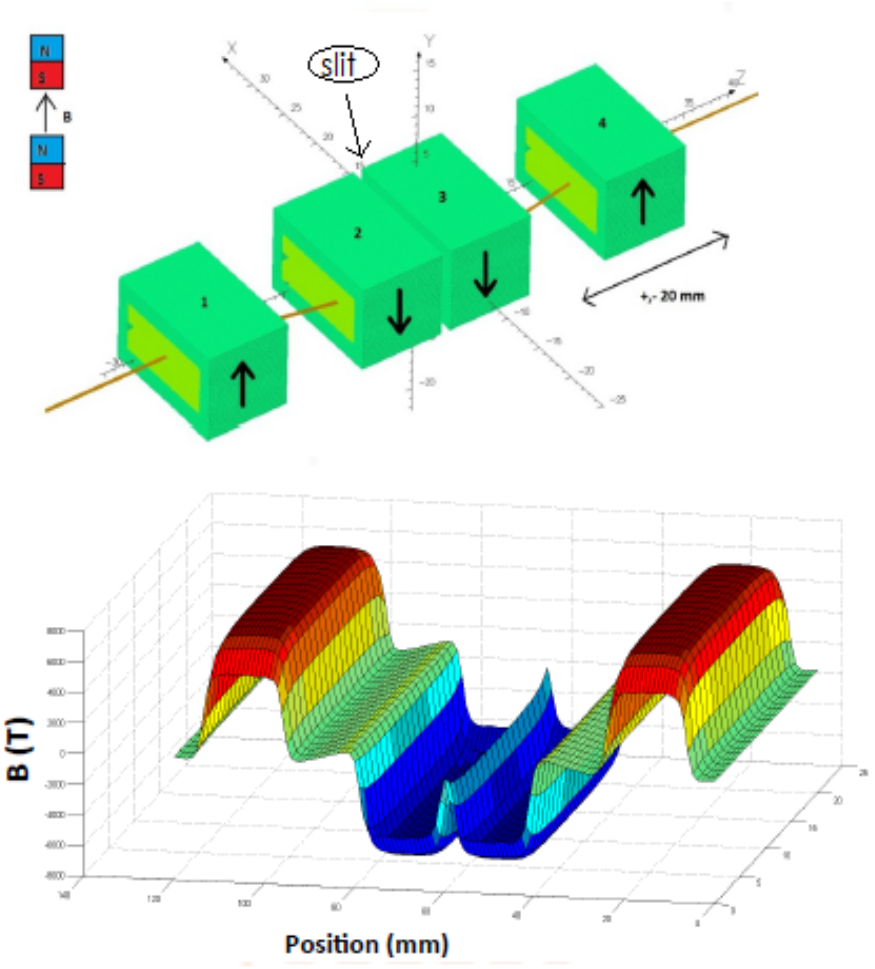

Fig. 30 Top: Graphic scheme of the ESS dipoles configuration. Bottom: ESS magnetic field profile. The maximum magnetic field value is 8400 Gauss; each experimental value is affected by ± 50 Gauss error, due to the uncertainty of the detector positioning.

The multi-MeV proton beam that passes through the first and second dipole, due to their opposite magnetic field polarity, is spectrally dispersed in the radial plane. At the exit of the second dipole, a satisfactory particle separation is achieved. Particles have a different trajectory as a function of their energy; in fact, lower energy components have a higher divergence angle than the higher energy ones. The movable slit device is placed between the two central dipoles, in order to further select in a narrower energy range particles that are going to enter the third dipole, and at the same time, to stop particles with a different energy than the selected one. The collimated particles are then refocused by the opposite gradient of the third and fourth dipole magnetic fields. Figure 31 schematically shows particles trends according to their energies.

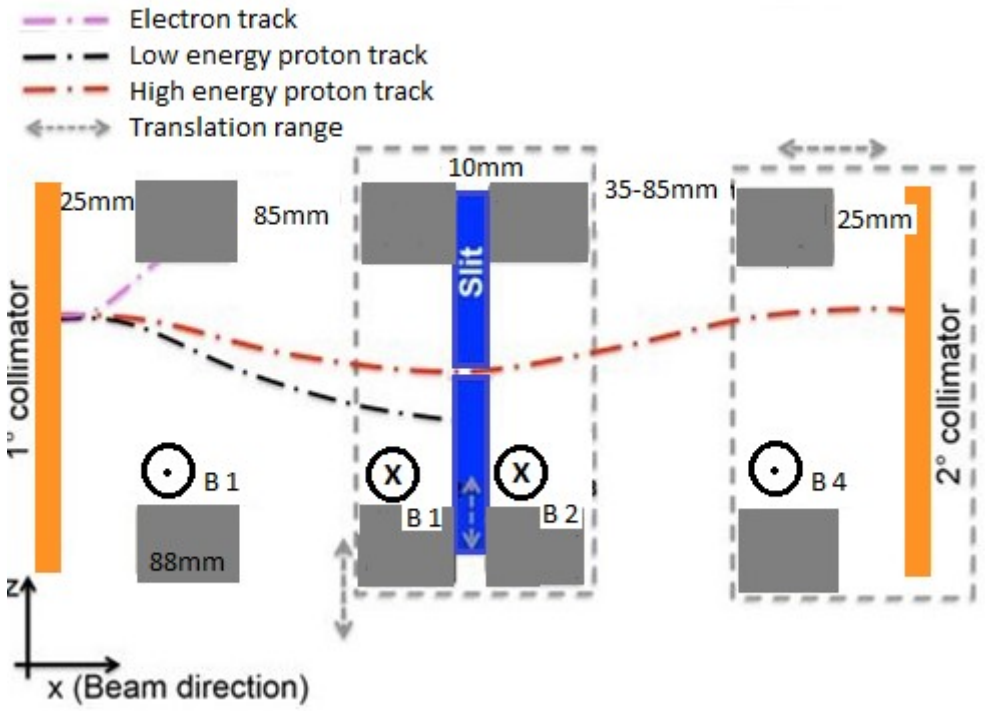

Fig. 31 ESS draft top view and representation of the particles path through the device.

The dipoles, thanks to their hybrid configuration, which is a combination of soft iron yokes and permanent magnets (NdFeB), provide a maximum magnetic field of ~ 0.8 T on a 10-mm gap. The slit device (see figure 31), can be maneuvered by a remote controller depending on the desired energy to be selected while a roller guide system allows the

radial movement of the twin central magnets by 50 mm in the transversal direction. This is also useful in appropriately selecting the lower energy components of the particle beam. In such a way, the device is able to select protons of energy within the range of 1-60 MeV. Furthermore, the last dipole can shift by 50 mm along the longitudinal direction (towards the third dipole) to compensate the asymmetry of the magnetic field. This movement minimizes the angular spread of the outgoing beam (figure 32, courtesy of Dr. A. Tramontana) [70].

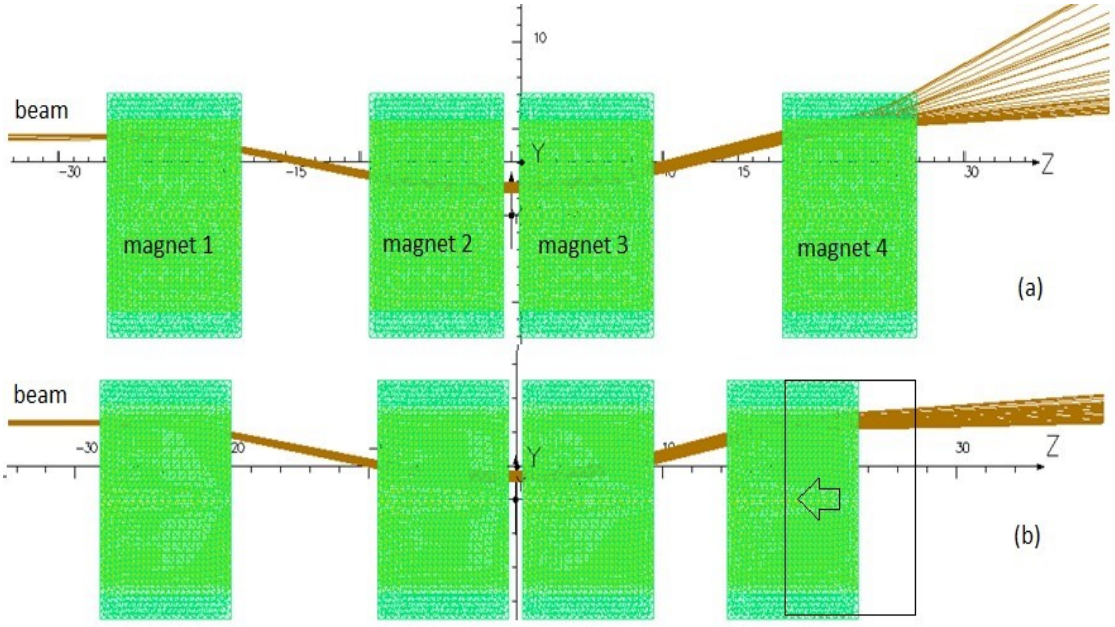

Fig. 32 Two possible layouts of the ESS are shown. Top: a symmetric positioning of the magnets is shown and the beam (incoming from the left) leaves the device with a wide angular spread. If the fourth magnet is shifted by a length in the order of centimeters (towards the third dipole), such an effect is minimized (bottom).

The whole magnet system is almost 600 mm in length and thanks to its compactness it is possible to mount it inside a typical laser target chamber, although the system has a dedicated vacuum case that can be placed along the beam transport line (figure 33). Two additional collimators are placed 25 mm upstream and downstream before and after the first and fourth dipole, respectively. The first collimator is used to preliminary select the

beam (in terms of its divergence angle) in order to limit the spatial mixing of particles with different energies inside the ESS, caused by the peculiar laser-driven beam wide angular distribution. The second collimator, instead, would refine the beam selection.

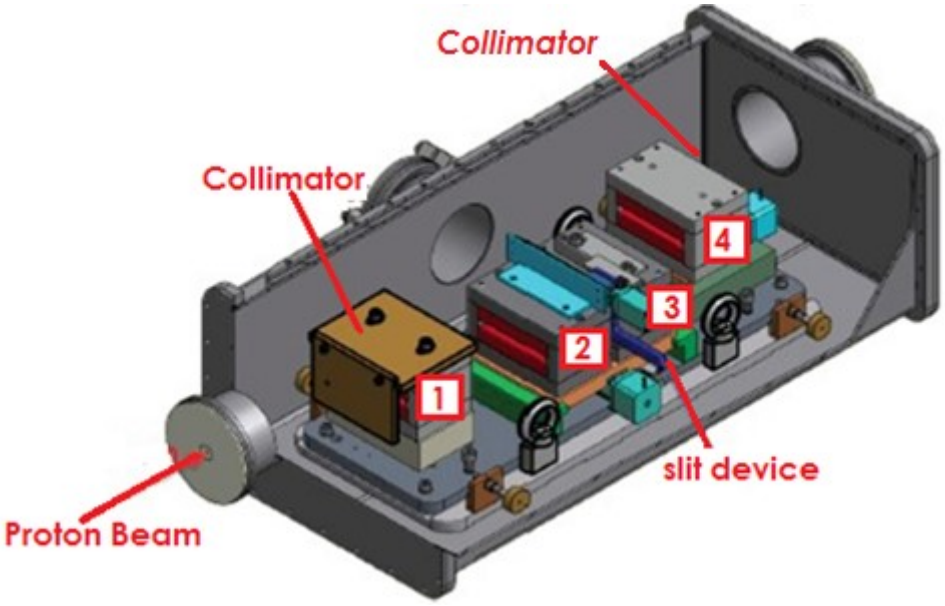

Fig. 33 CAD representation of the ESS in its dedicated vacuum chamber.

3.2.1 The ESS preliminary tests with conventional accelerators

The ESS has been successfully tested and calibrated in dedicated experimental campaigns with conventional proton beams at the Laboratori Nazionali del Sud (LNS-INFN) in Catania and at the Laboratori Nazionali di Legnaro (LNL-INFN) in Padova. The tests thus far completed are calibration of the slit-based device performed with the beam delivered by the 13-MV TANDEM Accelerator (LNS-INFN) and optical properties studies with the beam delivered by the 7-MV CN Van de Graaff (LNL-INFN). Both experiments were performed in collaboration with the LNS-INFN group.

The tests of the slit-based device with monochromatic proton beams of different energies were performed in order to ensure that at a given slit position (located between the two central dipoles) the expected energy was actually selected, thereby constructing a

calibration curve. Figure 34 reports a picture of the ESS in its vacuum chamber and a top view picture taken during the LNS-INFN campaign. The latter experiment was of fundamental importance in order to assess the correct functioning of the ESS for its possible future use.

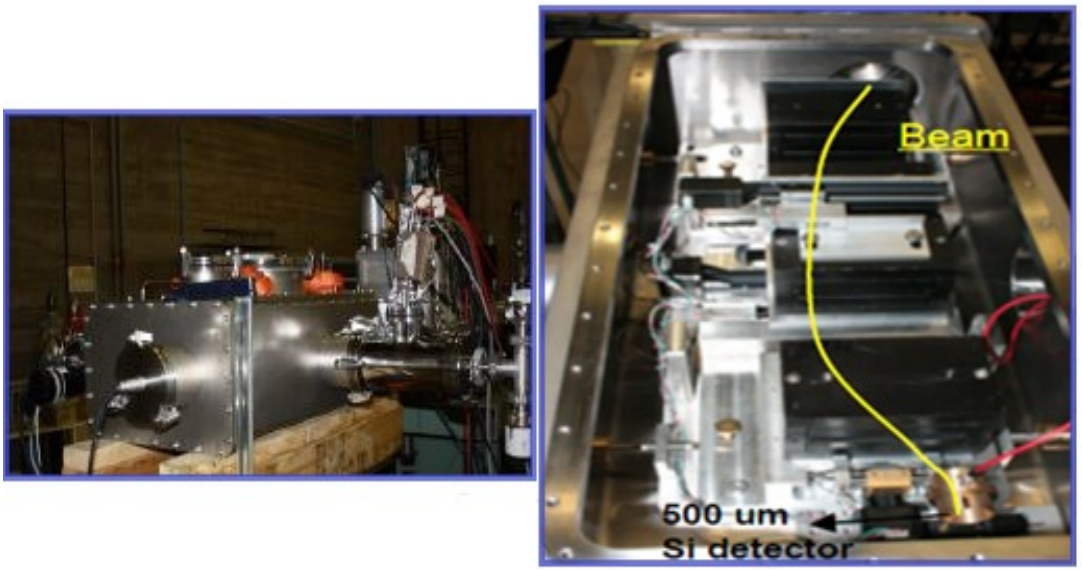

Fig. 34 Left: Picture of the ESS in its vacuum chamber at the beamline end of the TANDEM accelerator in Catania during the slit-based device system test shift. Right: ESS top view with beam trajectory illustration.

The results of the test show a good agreement between simulations, obtained by means of the GEANT4 toolkit (performed for comparison by the LNS-INFN colleagues), and the experimental data (figure 35).

An energy range of 4.5-12 MeV was investigated. The beam was collimated by means of an initial 2-mm thick Al collimator with a 3-mm diameter hole (placed before the first dipole) while the slit is an 8-mm thick Al device with a 1 mm × 10 mm aperture; no final collimator was used. Protons exiting the ESS were detected by a 500-μm Si surface barrier detector positioned downstream the fourth dipole along the initial beam direction.

The slit aperture size plays a role in the detected beam energy spread. Therefore, at a given selected energy, the spread can be reduced by decreasing the slit aperture; in this

case, one must consider that a smaller slit aperture decreases particle transmission efficiency through the device, hence the dose.

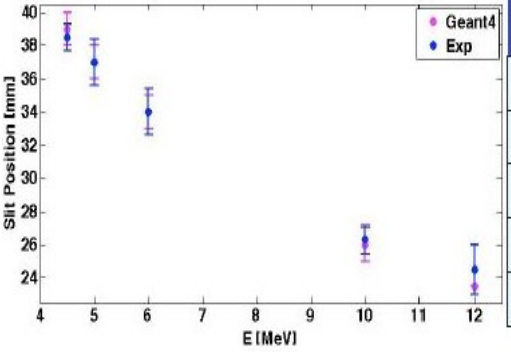

Energy [MeV]	Geant4 data [mm]	Experimental data [mm]	Percentage difference
4.5	39±1	38.5±0.8	1.3%
5	37±1	37.0±1.4	0%
6	34±1	34.0±1.4	0%
10	26±1	26.3±0.9	1.2%
12	23±1	24.5±1.5	4.2%

Fig. 35 Left: slit position as a function of energy calibration curve obtained with the monochromatic proton beam of the LNS-INFN 13-MV TANDEM accelerator in comparison with the simulated data. Right: tabulated data demonstrate the good agreement between simulations and experimental data.

The beam optics test was performed by means of a 5 MeV monochromatic proton beam produced by the CN-7MV Van de Graaff accelerator at LNL-INFN. In this experiment, only an initial 2-mm thick Al collimator (positioned before the first dipole) with a 3-mm diameter was used along the beam axial direction; no slit device or any other collimator were employed.

The beam dynamics through the four magnetic dipoles was studied by means of EBT3 radio chromic films (RCF, further described in Appendix B) detectors positioned, one at the time, behind each dipole.

Figure 36 shows the appearance of film detectors after a 10-s irradiation at an input proton beam current of 16 nA.

Figure 37, on the other hand, shows the simulation of the experimental ESS beam optics test campaign. As previously mentioned, simulations were obtained with the GEANT4 toolkit.

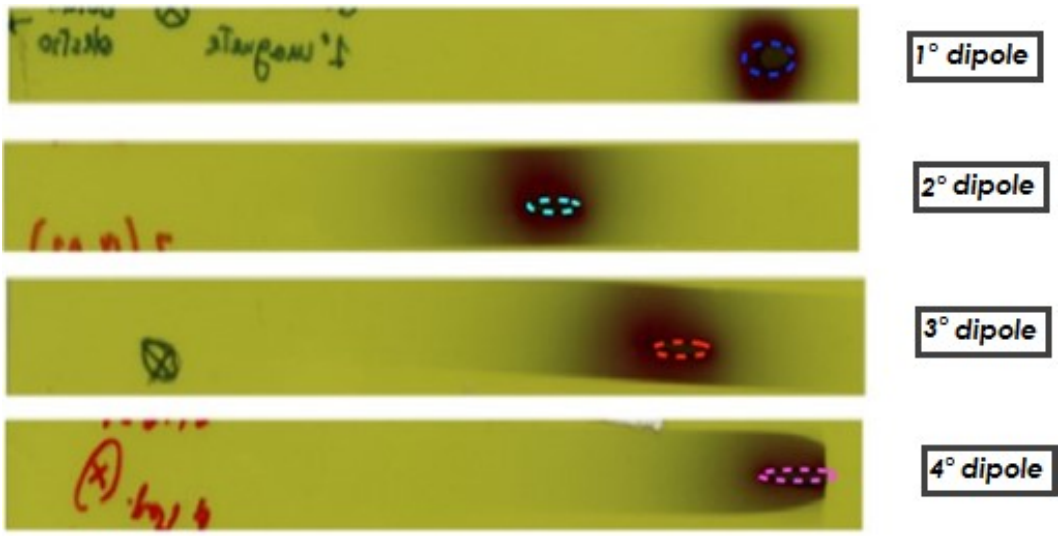

Fig. 36 ESS proton beam optics study: the film detectors sequence shows the beam dynamics of the 5-MeV proton beam through the selection device. Dashed circles (of different colors in correspondence to each GAF "stripe") represent the overlapping with the simulation result.

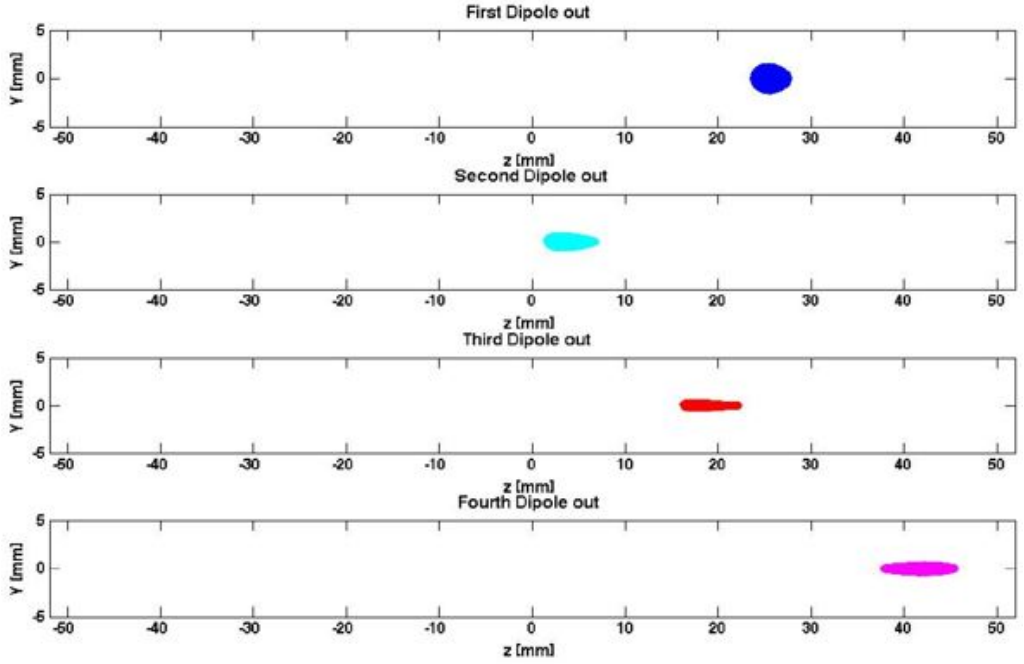

Fig. 37 ESS optics study simulation results: data relate to the beam exit position at each dipole; no input divergence was considered (courtesy of Dr. A. Tramontana).

3.2.2 The TARANIS run: experimental results

As previously mentioned, before optically accelerated laser-driven proton beams may be used in the clinic, the ability to control their properties in a reliably reproducible manner must be demonstrated. Among such properties, the broad energy spectrum of the output beam represents one of the most important characteristics to deal with; in fact, it can go from the order of keV up to maximum cut-off values that are related to the laser power and to the target properties [73, 74]. A first experimental shift dedicated to the characterization of the ESS prototype was carried out with an actual laser-driven beam at the TARANIS (Terawatt Apparatus for Relativistic and Nonlinear Interdisciplinary Sciences) laser facility of the Center for Plasma Physics at the Queen's University of Belfast (QUB, UK), whose detailed optical layout is reported in figure 38.

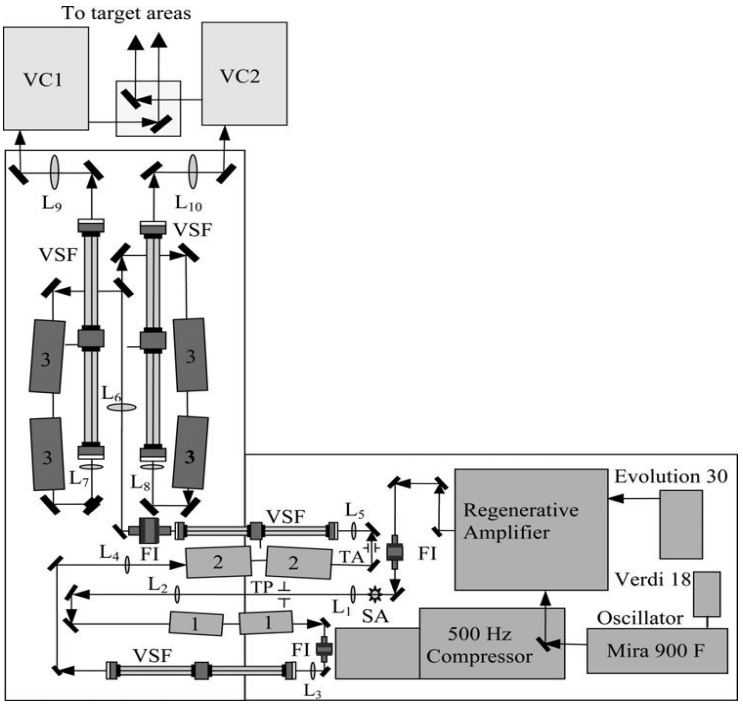

Fig. 38 TARANIS laser optical layout. Abbreviations used in the image are here explained. FI: Faraday isolator; VSF: vacuum spatial filter; TA: Teflon aperture; TP: Teflon pinhole; SA: serrated aperture; 1-2-3: laser heads with Nd:Glass rods of 9 mm, 25 mm, and 50 mm diameter, respectively; L1L2-L3L4-L5L6-L7L9- L8L10: relay imaging telescopes; VC1-VC2: vacuum compressors.

TARANIS is a hybrid Ti:Sapphire-Nd:glass laser system that operates in the CPA regime. It can simultaneously deliver two beams with ω=1053 nm, one in each of the two existing target areas, at two different pulse durations of ~700 fs and 1 ns, with intensities of ~10^{19} W/cm^2 (in the short pulse mode) and up to an energy of 30 J on the target with the ns laser beam [75]. During the run carried out as part of this thesis, the laser was focused on an *F*/3 Of-Axis Parabola (being the OAP the focus property of the parabola), characterized by a focal length of 300 mm.

Taking into account the spatial constraints that a laser target chamber normally presents due to the ensemble of the focalization and diagnostic components, the ESS was positioned at about 8 cm from the laser-target interaction point. Two collimators composed of 2-mm thick Al plates with a circular 3 mm diameter aperture were placed at the entrance and at the exit of the ESS, respectively, in order to reduce the angular divergence and to control the beam spot size.

The slit-based device was placed between the second and the third dipole as in the ESS standard configuration. It consisted of an 8-mm thick Al plate with an *ad hoc* rectangular aperture of 3 mm (height) × 6 mm (width) as to maximally reduce the particle spatial mixing effect and achieve a satisfactory transmission efficiency. Behind the ESS, at 30 cm downstream after the final collimator, a spectrometer was used to obtain quantitative information regarding the energy spread of particles leaving the ESS. The spectrometer consisted of a 10-cm long 0.9-T intensity magnet equipped with a 500 μm slit aperture on its front surface; the latter selected protons that were then deflected according to their energies. The deflection measurements along the radial plane of the detector signals obtained by means of an Image Plate (IP) (a detailed description of whose working principles can be found in the Appendix C) made possible to attain the energy spread interval of the out coming beam (knowing the magnetic field intensity).

Figure 39 shows a sketch of the experimental set-up within the TARANIS target chamber and the spectrometer device while figure 40 depicts the TARANIS chamber and the ESS positioning into it.

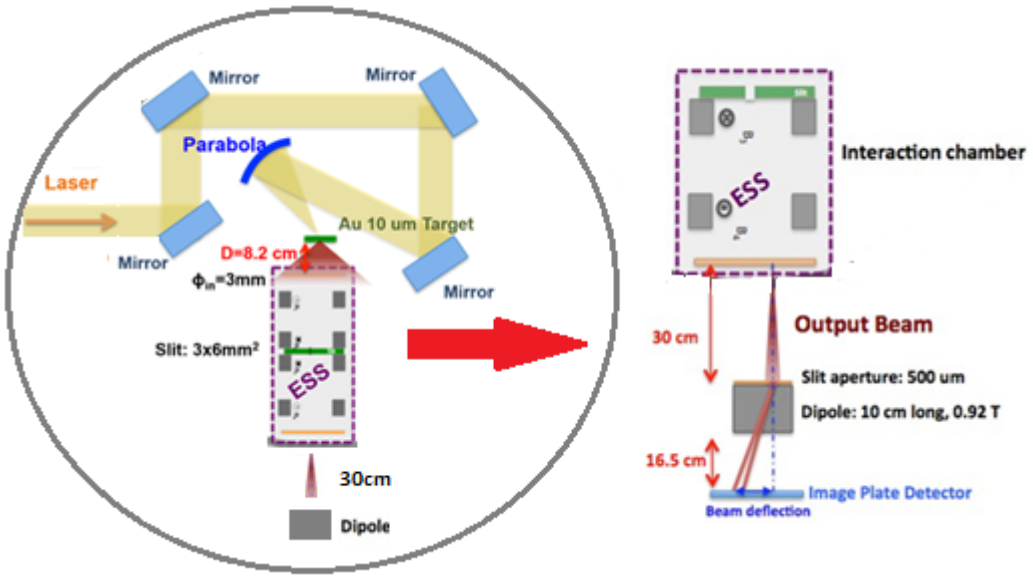

Fig. 39 Left: overall scheme of the experimental set-up. Right: energy spreader system, consisting of the spectrometer (~0.9T magnet).

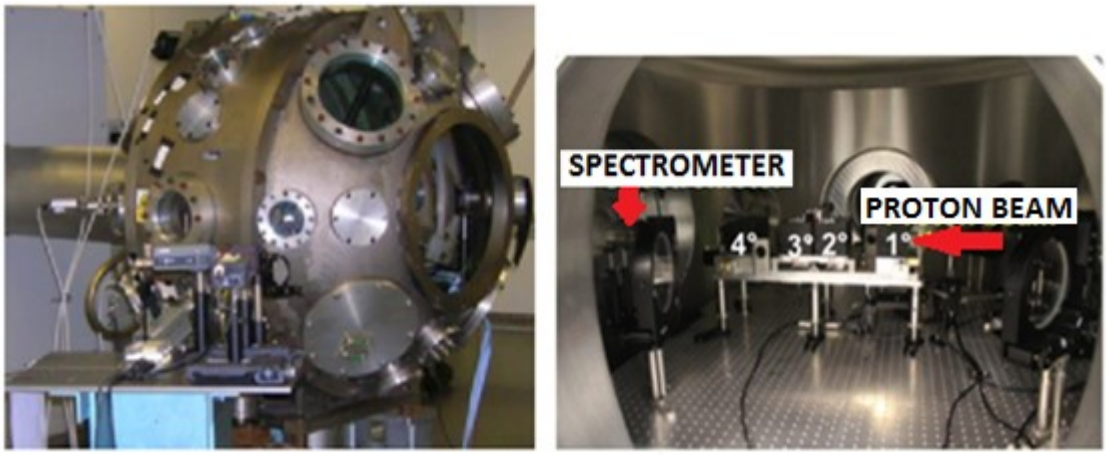

Fig. 40 Left: TARANIS target chamber is shown. Right: Picture of ESS and additional spectrometer positioned inside the chamber.

The first part of the experimental campaign carried out at QUB was dedicated to study the beam properties by placing immediately after its production by the laser-target interaction (i.e. before the proton beam entered the ESS) an HD-810 RCF stack, wrapped in a 12-μm Al foil to avoid electron, heavy ion and photon contributions to the signal. Such

arrangement allowed the gathering of information regarding the beam input properties such as energy, proton abundance and angular distribution (figure 41). RCFs were chosen for their low-energy dependence, high spatial resolution and dose-rate independence properties [76].

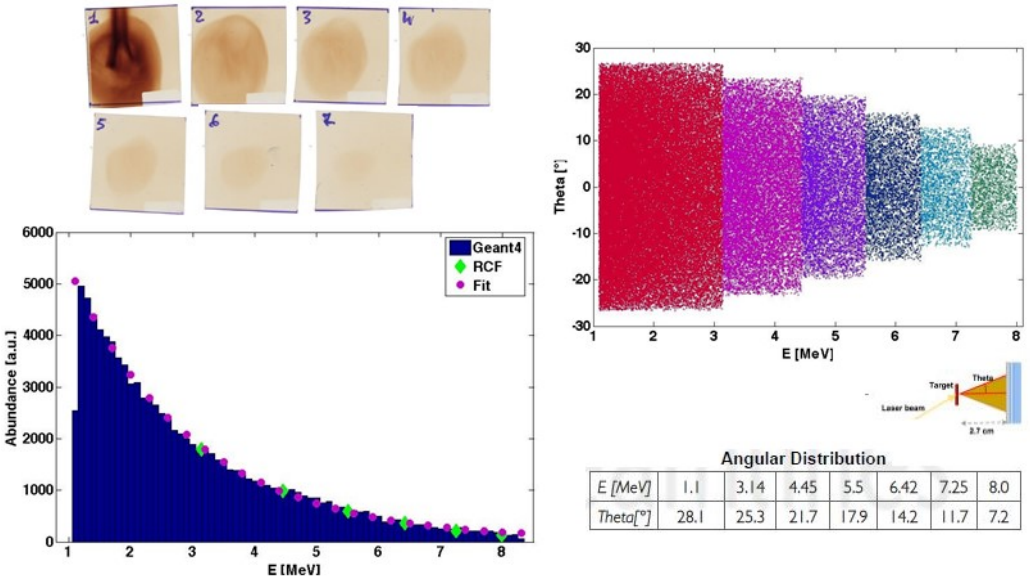

Angular Distribution

E [MeV]	1.1	3.14	4.45	5.5	6.42	7.25	8.0
Theta[°]	28.1	25.3	21.7	17.9	14.2	11.7	7.2

Fig. 41 Top left: detectors signals of a EBT-810 RCF stack positioned at about 3 cm from the 10-μm thick Au target. Graph of proton abundance obtained from RCF measurements (green dots) and correspondent simulation data (bottom left). Right: beam angular distribution simulation as a function of energy. Energies and correspondent divergence angle values are also reported.

Several output configurations were tested: for example, detectors were positioned at different distances downstream the ESS and various slit-based device positions were employed in order to select different energies as well. Figure 42 shows a typical beam output study and figure 43 shows the corresponding solid-state nuclear track detectors CR-39 analysis. For more details on the properties of CR-39 detectors see Appendix D.

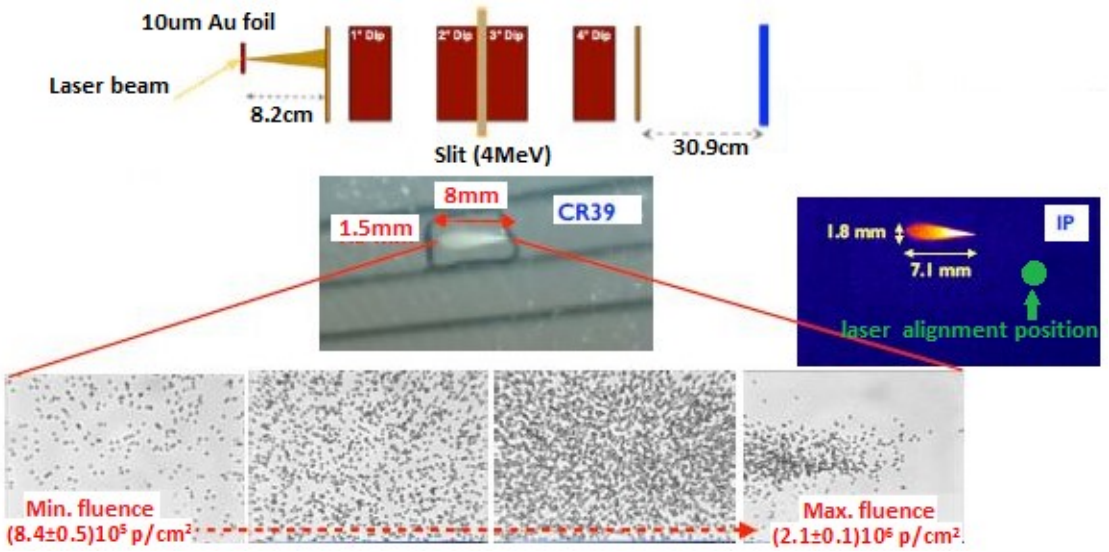

Fig. 42 Example of a laser shot analysis. The slit device was positioned in order to select particles having an energy of 4 MeV. CR-39 and IP detectors, positioned downstream at about 31 cm from the final collimator, were used to obtain information regarding beam dimension and fluence. The central CR-39 pictures sequence shows a fluence variation within the irradiated spot. A poor agreement between the laser alignment position (green dot in the IP image: center right) and the actual beam spot position is also shown.

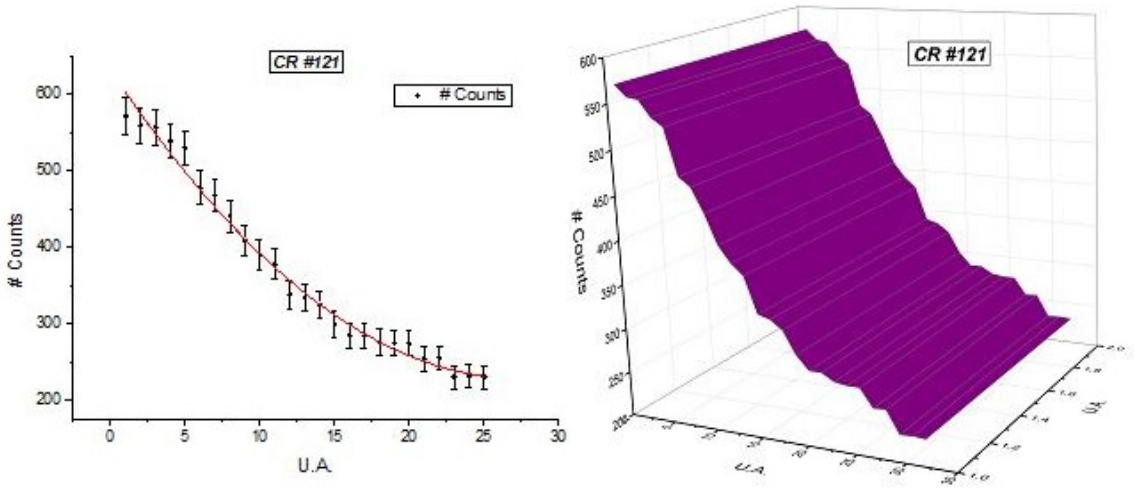

Fig. 43 Study of the CR-39 discussed in figure 42. Left: Counts distribution along the central axis of the beam spot affected by a Poisson error. Right: 3D counts distribution representation.

The shot analysis graphically represented in figure 42 points out that the layout of the ESS, i.e. with the four magnets aligned on the same axis, gave rise to a magnetic field gradient on the edge between the two central dipoles. This, in turn, led to a non-uniformity of the beam fluence within the irradiated spot and to a poor agreement between the laser alignment position and the actual beam spot on the considered detector (discussed in figure 42).

This issue, together with low-fluence values (hence, dose values in the order of cGy) and an unacceptably large energy spread when selecting a specific energy (all these factors making impossible proper radiobiological studies), led to a new configuration of the ESS.

The two central dipoles will be shifted (of a few centimeters) from the coaxial direction along which the external magnets are located in order to direct the beam in the uniform region of the magnetic field (figure 44). Furthermore, a module composed of four permanent magnet quadrupoles (PMQ) placed before the ESS will be used (figure 45).

The purpose of the PMQ system (developed at the LNS-INFN) is to collect the largest fraction of particles as well as reduce the beam angular divergence. The device has to be rather compact due to the unavoidable positioning into the vacuum chamber, which has to be as close as possible to the proton production point, therefore to the target (as shown graphically in paragraph 3.1, figure 29). To satisfy such requirements, solenoid magnets producing pulsed high magnetic fields are used. In fact, a solenoid has a large acceptance and guarantees focusing on both transverse planes [77, 78]. Furthermore, considering that the focal point of a solenoid depends on the particle energies, this system is also able to provide a very preliminary energy selection with the aid of a collimator placed at its entrance. However, the PMQ energy selection is defined as preliminary since part of the low and high-energy beam components pass through the solenoid-collimator system and are transported together with the desired energy particles due to the intrinsic “collecting” effect of the PMQ device.

Such an arrangement is expected to maximize particles transmission efficiency and to focus the beam on the slit plane, which will reduce the energy spread, increase the fluence values (hence dose values in the order of a few Gys) and the particles uniformity,

making the beam suitable for radiobiology studies. The four permanent magnet quadrupoles have been recently delivered to the LNS-INFN in Catania (figure 46): tests and calibrations are undergoing.

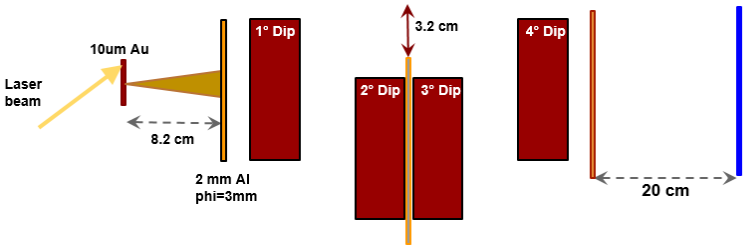

Fig. 44 Layout of the ESS configuration with the central dipoles shifted of about 3 cm from the coaxial direction along which the external magnets are located as to direct the beam in the magnetic field uniform region.

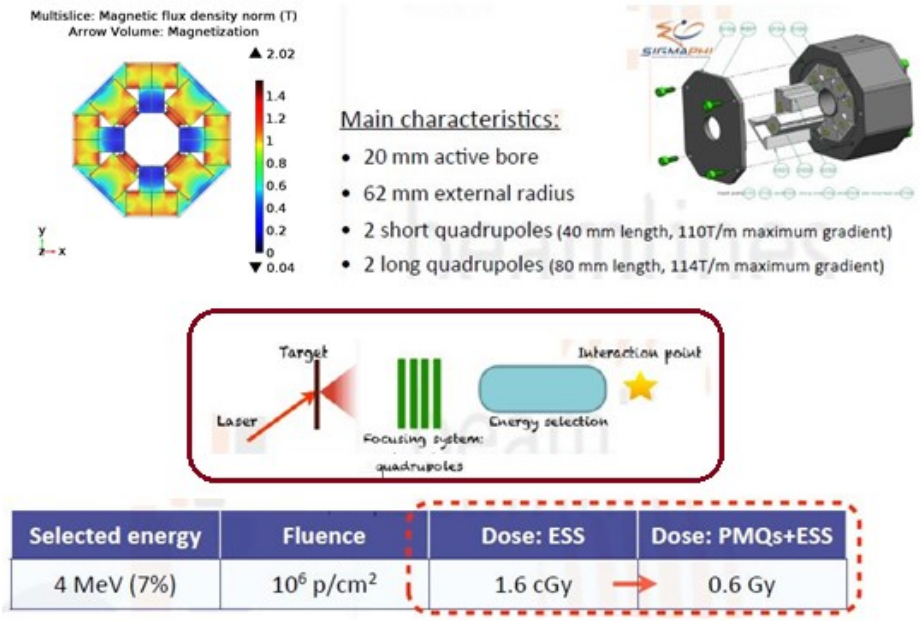

Fig. 45 Top left: as an example the magnetic flux density of one of the two 40-mm length quadrupole that composes the PMQ system and main characteristics of the device (top right) are reported. Bottom: PMQ allocation into the beam transport line (BTL) and, as an example, fluence and corresponding dose values of a beam output with and without the PMQ module at a given energy value.

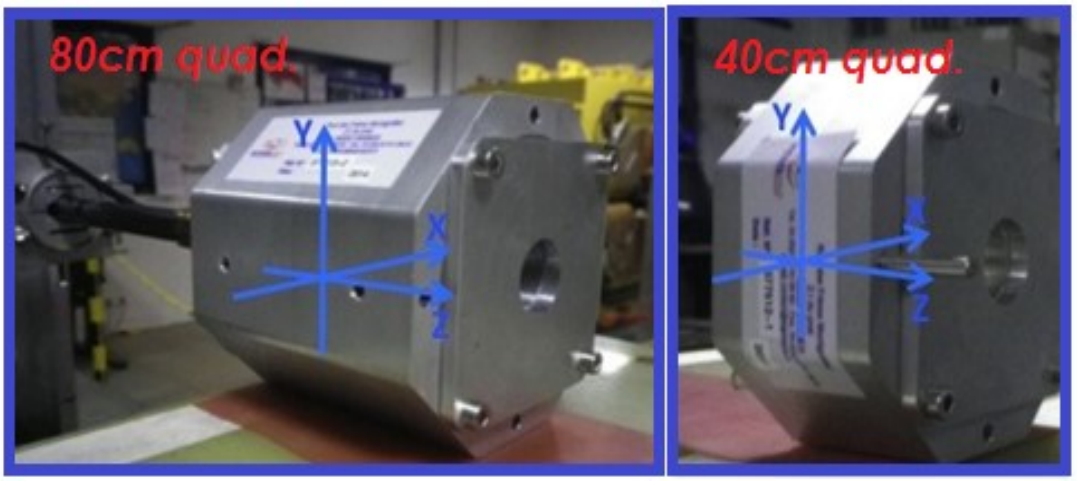

Fig. 46 Picture of one of the two 80-mm length quadrupole (left) and of one of the two 40-mm quadrupole components (right).

Chapter 4

Second experimental campaign

Hadrontherapy is an excellent candidate for deep-located tumor treatment. This assertion is based on a physical principle: charged particles exhibit an inverse depth-dose deposition profile, which significantly reduces the overall dose absorbed by normal tissues and organs. However, such non-negligible amount of radiation absorbed in correspondence of the plateau region of the Bragg curve (paragraph 1.1) may still result in sub-lethal damage to healthy cells, such as Stress-Induced Premature Senescence (SIPS, discussed in paragraph 1.2.4), and possibly with a greater efficiency than after low-LET radiations (see concept of RBE discussed in paragraph 1.2.2). It is also of fundamental importance to have information regarding the lethal potential of a given radiation studying cellular radio-sensitivity, therefore cellular survival.

Moreover, reliable hadrontherapy follow-up patient data is limited since this type of treatment has been adopted relatively recently. The very first use of protons for radiobiological issues was proposed in the '40s from R. Wilson [79].

The possible clinical use of laser-driven particle beams as a long-term less expensive alternative to large and complex conventional accelerators cannot overlook a careful study of the radiobiological properties of such beams. The unique physical properties that laser-driven beams possess, such as an exceedingly high dose-rate coupled with a pulsed nature, originated by laser interaction with target materials, yield open issues. The physical pattern of the energy deposition events drives the biological outcome of the exposure to ionizing radiation. The extreme spatio-temporal features of laser-driven particle beams may cause unknown biological responses [80]. A possibility is that a spatio-temporal overlapping of independent particle tracks occurs resulting in the production of collective effects. The lack of correlation between direct (caused from ion-DNA and secondary electron interaction) and indirect effects (caused by free radicals with a diffusion time up to 1 μs) can also occur. How these factors can influence the onset

of healthy tissue damage and/or can efficiently kill tumor cells is unknown and must be examined by in vitro experiments at facilities such as $LULI_{2000}$, a laser laboratory based at the Ecole Polytechnique in Paris. There we successfully conducted a preliminary experimental campaign in 2015, achieving a satisfactory reproducibility of physical parameters such as dose, and attaining interesting radiobiological results.

In general, very little data exist on cellular survival by laser-driven beams. Instead, to the best of our knowledge at the time of the experimental campaign below described, SIPS had never been studied with such peculiar beams. The few experiments so far carried out concentrated mainly on the lethal effects caused by pulsed beams with ultra-high dose-rates measuring, in some cases, the accumulated dose over several laser shots [81–83], while in other cases a single short burst deposition was considered [84–87]. It has been argued that no significant difference ought to be expected between laser-driven and conventionally accelerated proton beams in terms of biological response since the modality with which an ion is accelerated should not influence the damage it causes at the cellular or molecular level. However, experimental data are needed. In the radiobiological experimental campaign described in this chapter, the obtained results need further experiments to be confirmed but surely gave us the opportunity to make some interesting considerations.

4.1 The LULI experimental set-up

The experimental campaign, as mentioned, was performed at the $LULI_{2000}$ facility of the Ecole Polytechnique in Paris. It is a unique facility in Europe because of the possibility to couple simultaneously on target high-energy pulses of *ns* and *ps* durations as well as auxiliary beams. The $LULI_{2000}$ laser hall is composed of two laser chains (North and South) mono-pulse Nd:Glass, respectively named $NANO_{2000}$ and $PICO_{2000}$. Figure 47 gives an outline of the laser hall and the two experimental areas [88].

The $NANO_{2000}$ is the nanosecond component of $LULI_{2000}$ and consists of two Nd:Glass laser chains, of 200 mm in diameter, each one delivering 1 kJ in nanosecond pulses at a

ω=1053 nm wavelength. A fiber oscillator allows the shaping of all desired temporal pulse durations from 0.5 to 20 ns while the repetition rate is limited to a shot every 90 minutes; between 4 and 6 full energy shots per day are achievable. Through the implementation of the $NANO_{2000}$ laser chain by means of the CPA process it is possible to deliver up to about 150 J at a ω=1053 nm wavelength (150 TW) in 1 ps; the latter is therefore the configuration called $PICO_{2000}$.

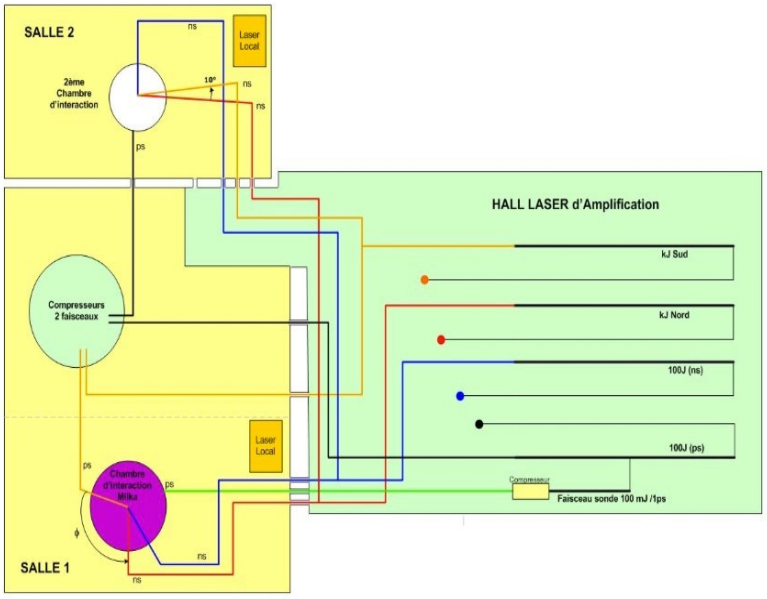

Fig. 47 $LULI_{2000}$ facility. Laser hall and experimental areas.

The experiment was carried out employing the $PICO_{2000}$ laser beam directed in the vacuum chamber (*"salle 1"*, figure 47) named "Milka" (figure 48). The beam was focused on the foil targets surface with an incidence angle of approximately 22.5º thanks to an *F/*4 Off-Axis Parabola (being the OAP the focus property of the parabola), characterized by a focal length of 800 mm. Our working regime laser energy at the entrance of the compressor, on average, was of 100±10 J with a pulse duration of 1.3ps; taking into consideration that the compressor efficiency was about 65%, the mean laser intensity we reached was approximately 5×10^{19} W/cm^2. Figure 49 reports the $PICO_{2000}$ laser focal spot obtained in the experimental run and its ImageJ reconstructed profile. The campaign was performed in collaboration with the LNS-INFN group and the QUB-Belfast group.

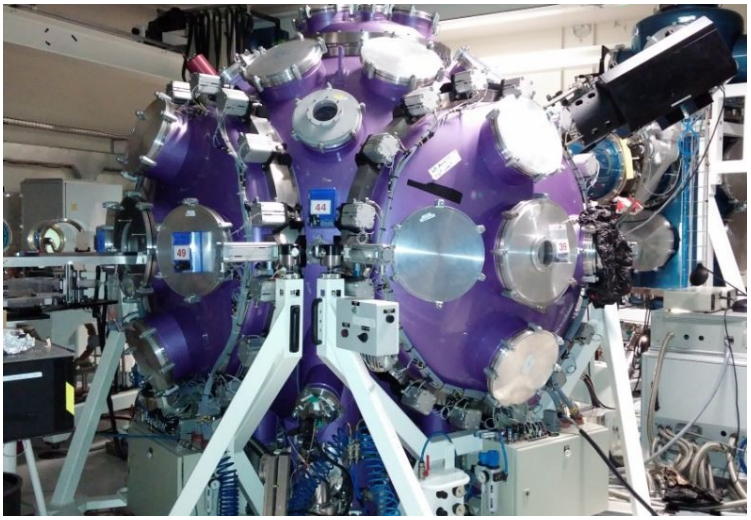

Fig. 48 External view of the "Milka" target vacuum chamber.

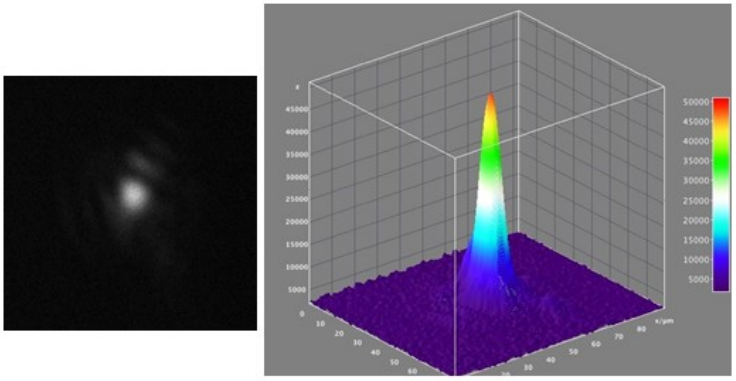

Fig. 49 PICO$_{2000}$ focal spot obtained during our experimental run (left) together with its ImageJ reconstructed profile (right).

Our aim was to expose cells only to particles with a selected (and as narrow as possible) energy range, while, at the same time, achieving reasonably high doses able to produce radiobiologically detectable results. Therefore, a beam transport and delivery system capable of separating protons with different energies was installed inside the target chamber and an in-air tube re-entrance ensured appropriate dose values to be reached. To optimize the number of samples to be irradiated, we simultaneously exposed three cell dots in one shot (on the same sample), each one with a specific energy and a specific dose as will be described in more detail below.

A sketch of the experimental chamber arrangement is shown in figure 50 together with a close-up view of the beam transport and delivery system. Figure 51, instead, shows a CAD reconstruction and a picture of the target chamber configuration.

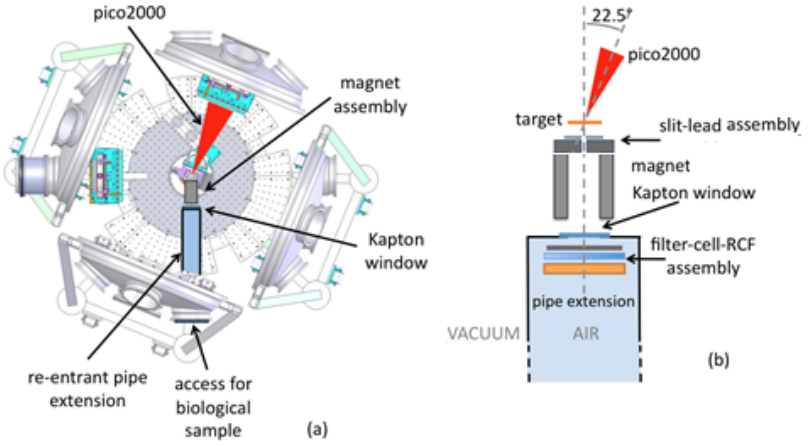

Fig. 50 (a) General overview of the target chamber arrangement. (b) Details of the transport and delivery system and of the biological sample positioning inside the in-air re-entrant pipe extension.

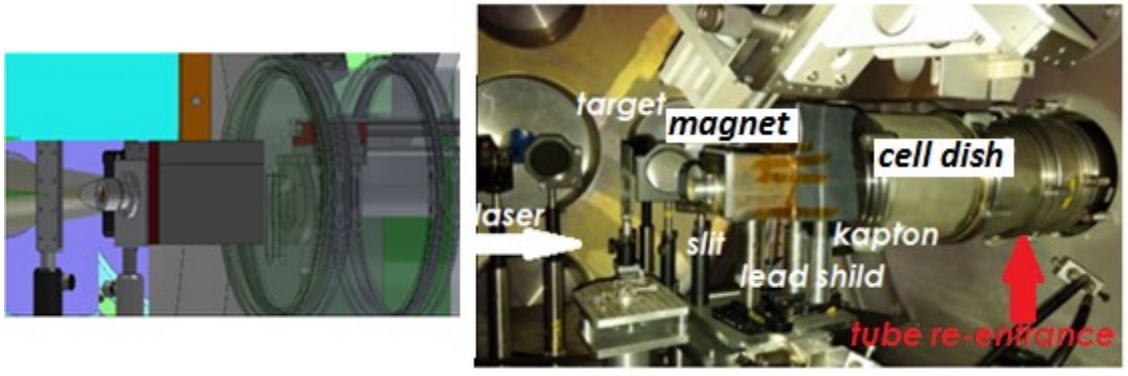

Fig. 51 CAD reconstruction of the vacuum chamber (left) and an explanatory picture taken during the experimental shift (right).

The laser was focalized on thin foil targets located at the nominal center of the target chamber on a permanent motorized stage. The target thickness was varied in order to optimize the proton energy, the beam uniformity and the dose values. The use of gold

(Au, Z = 79) was based on the experience acquired in previous experiments where it had been proven that high-Z target materials provide the best performances in terms of proton beam spatial homogeneity and uniformity. The thickness of the targets ranged between 10 and 50 µm in correspondence to different shots since employing thinner targets (of a few µm) maximizes the beam energy and dose (within certain limits as discussed in paragraph 2.2), while increasing the target thickness provides a higher degree of dose control but lower dose values.

After being produced by the laser-target interaction, the multi-MeV proton beam encounters the transport system installed inside the vacuum chamber along the target's normal axis, equipped with an entrance slit located at about 50 mm from the target itself. Two different slit widths were used, respectively of 310 and 520 μm, in order to change the final beam features in terms of particles abundance. The beam transport consisted of a 100-mm long permanent magnet with a constant magnetic field of about 0.9 T on a 50×4 mm gap. During the run, the chamber pressure was about 10^{-4} mbar. Figure 52 shows the experimental magnetic field values, measured using a Hall probe, in the central plane of the gap.

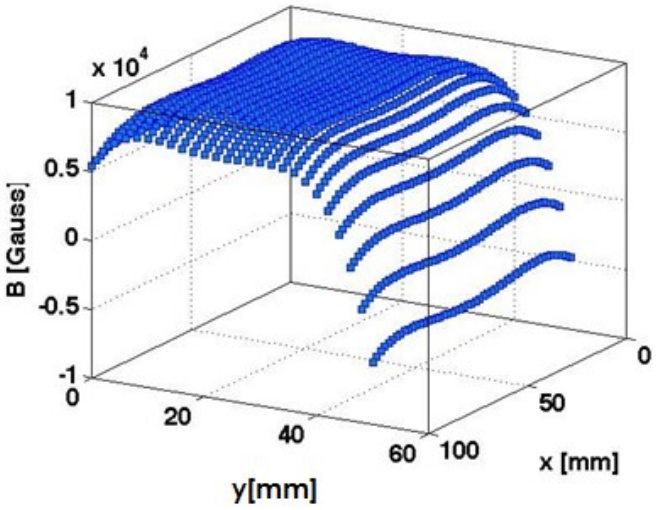

Fig. 52 Experimental magnetic field values obtained in the central plane gap of the 0.9 T permanent magnet used in our campaign.

The use of a dipole with the magnetic field orientated perpendicularly to the beam propagation direction, gives rise to the protons' deflection that are angularly dispersed according to their energy; this is due to the Lorentz force component perpendicular to the magnetic field. Ions heavier than protons will also be deflected but at different angles due to their higher mass. In any case, a great percentage of them was suppressed before entering the magnet by employing metal filters of suitable thickness placed just behind the slit device. Instead, parasitic X-ray radiation was suppressed by appropriate lead shielding in the chamber, while X-rays going through the slit will be spatially separated from the deflected protons and will not reach the sample (figure 53).

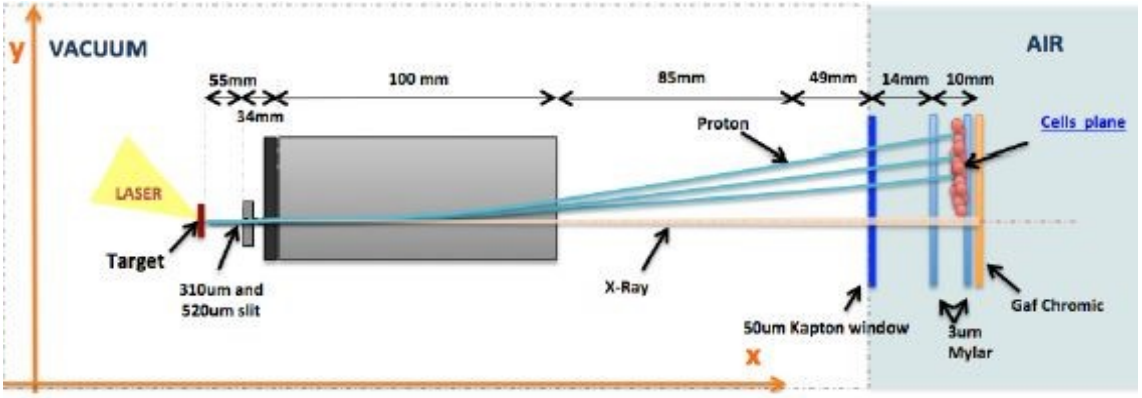

Fig. 53 Proton beam transport and delivery system. Particles experience a magnetic deflection due to the Lorentz force.

The angularly dispersed proton beam was transported to the cell dish through a 50 µm thick Kapton window, with transverse dimensions of a few cm. The elasticity and stress resistance properties of the Kapton window ensured the proper sealing of the vacuum chamber.

The dish containing the biological sample was placed outside the target chamber behind the Kapton window in the in-air tube re-entrance. The latter was required in order to reduce the overall distance from the proton production to the irradiation point, which is in turn necessary to maximize the delivered dose onto the cells as previously discussed. To facilitate the installation and removal of the sample, the dish was mounted on a sliding

system consisting of a metallic arm that allowed to insert and extract the dish from the tube re-entrance and ensured the correct positioning at each shot (figure 53).

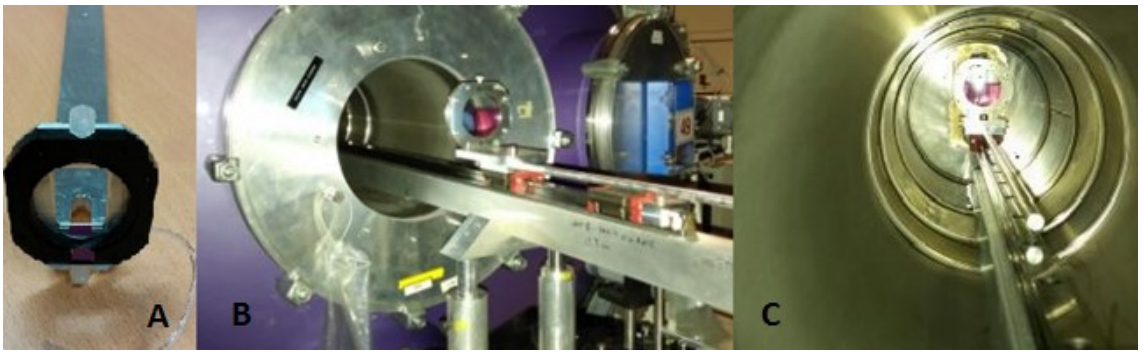

Fig. 53 (A) Picture of the dish holder connected to the metallic arm. (B) Cell dish positioned on its arm holder prior to being inserted into the tube re-entrance and its final irradiation location (C).

Cells were seeded on a 3-µm thick mylar sheet in three separate dots, each one in a specific position, corresponding to an area of 3x5 mm^2. The latter configuration allowed us to simultaneously expose each cell dot to a different energy and dose within the same laser shot (figure 54); after exposure, the cells from each dots were treated and examined independently.

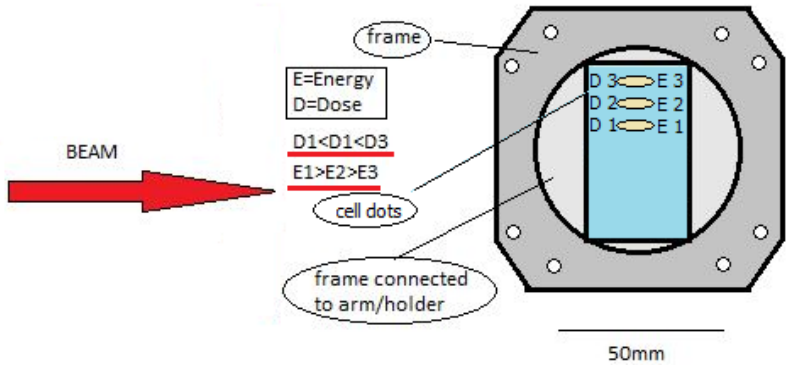

Fig. 54 Scheme of the cell dish and positioning of the cell dots (not in scale).

The customized sample dish was composed of three elements: an inner component and two twin external components (to which mylar sheets are attached) screwed to the top and bottom of the inner part (figure 55). The dish was equipped with an automated syringe system in order to be able to remove the cell media during irradiation and to re-inject it immediately post irradiation. A schematic overview of the overall irradiation configuration is shown by means of a simplified draft in figure 56.

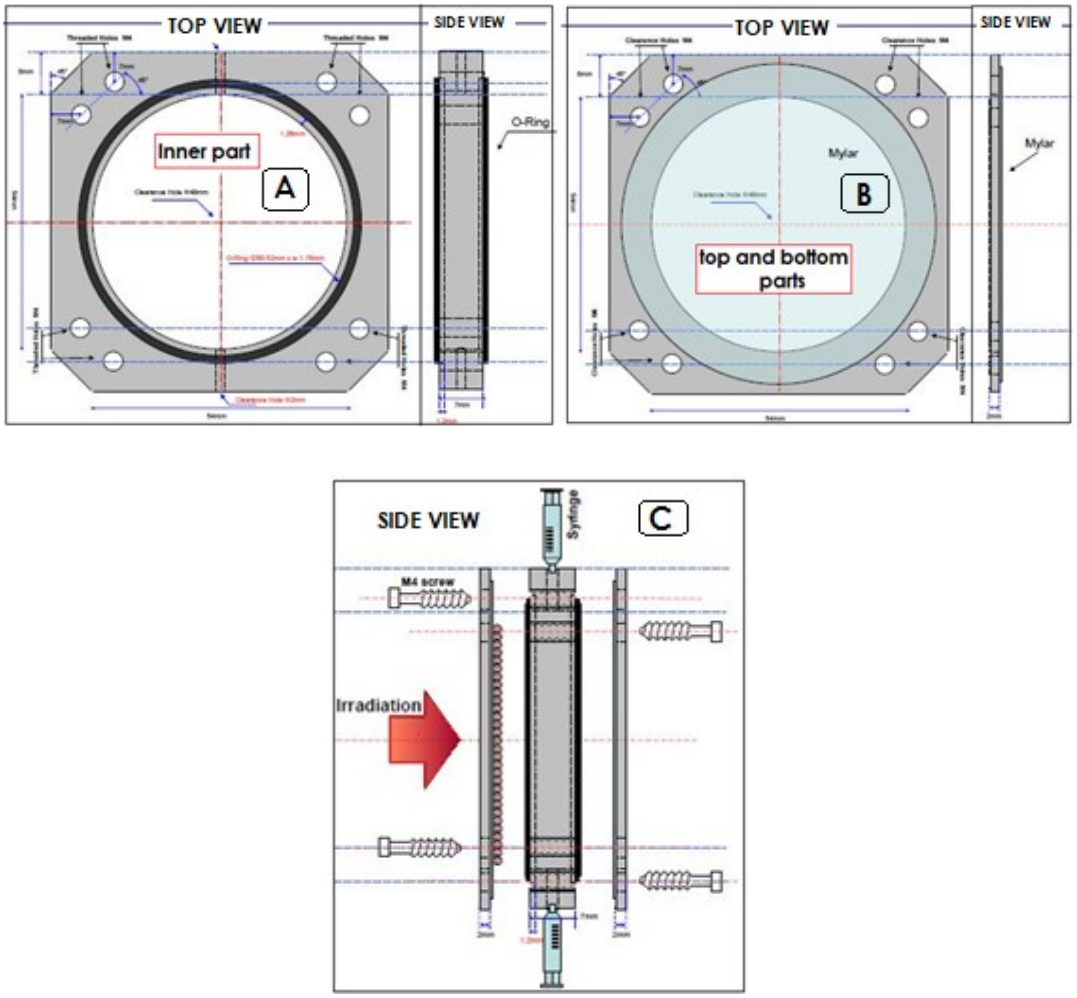

Fig. 55 CAD representation of the cell dish used at the LULI$_{2000}$ run. A: Cell dish inner component made of a bio-compatible polyester compound. B: Cell dish top and bottom aluminum elements to which mylar is attached. C: Cell dish assembly.

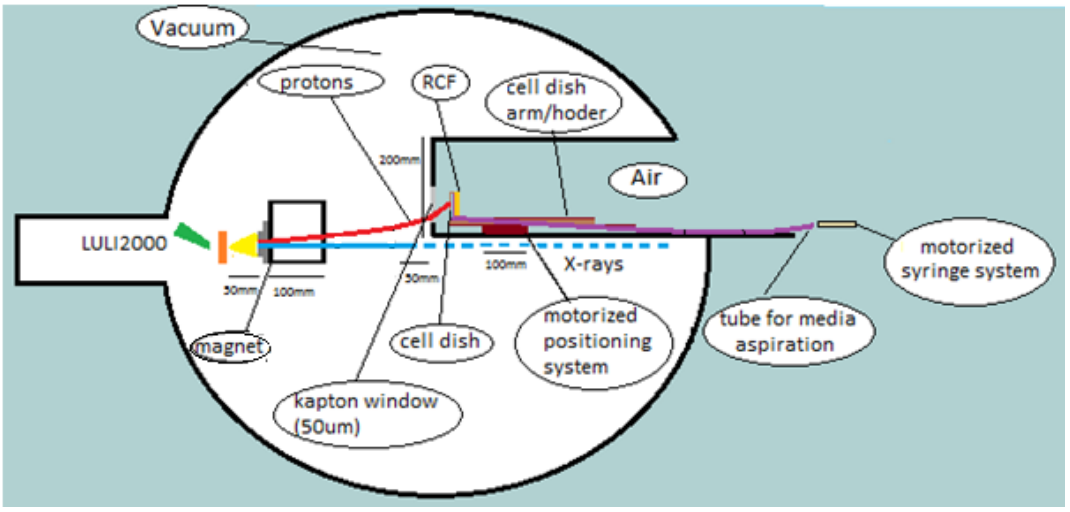

Fig. 56 Schematic layout of the irradiation set-up (not in scale).

4.1.1 The LULI dosimetry system

The LULI dosimetry set-up configuration involved the employment of different particle detectors such as radiochromic films (RCF), image plates (IP) and nuclear track detectors CR-39s. Details of their working principles can be found in Appendix B, C and D.

Prior the cell irradiation, low-sensitivity HD-V2 RCF were positioned inside the target chamber at about 5 cm from the proton source, in order to study the beam input properties, in terms of energy and angular distribution, before it entered the transport and delivery system. HD-V2 stacks were wrapped in a 12-μm Al foil in order to reduce the electron, heavy ion and photon contributions to the detector's signal.

In figure 57, as an example, a RCF stack composed of 27 layers, obtained irradiating a 25-μm Au target is reported. The energy values written on each RCF layer are obtained using the Stopping Range of Ions in Matter (SRIM) software toolkit. In general, RCF can be used as a single detector or in a stack configuration to obtain the energy spectrum of the incident protons [89, 90]. Figure 58 shows the energy distribution as a function of particle abundance correspondent to the laser interaction with the three Au targets thicknesses (10, 25 and 50 μm) employed in this experiment.

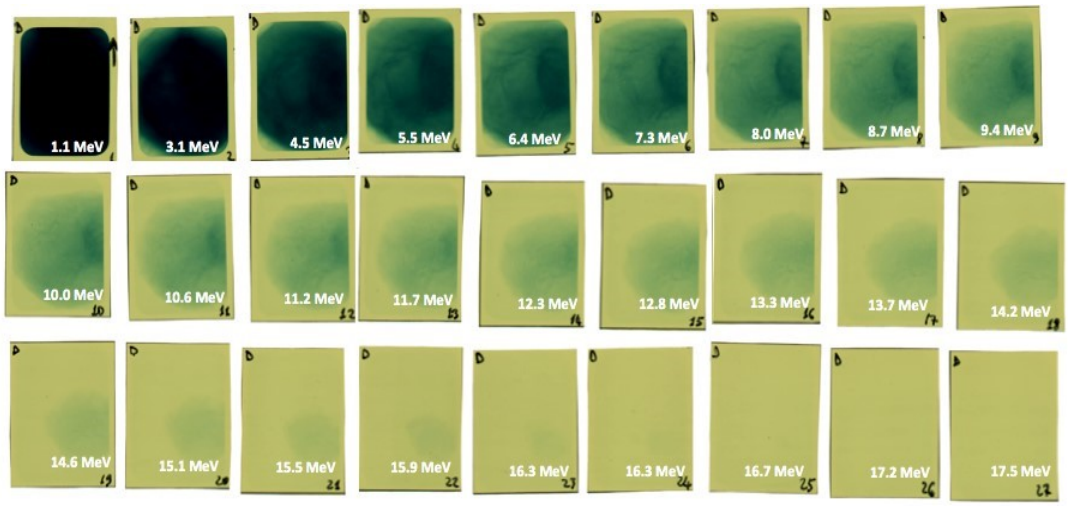

Fig. 57 RCF stack obtained irradiating a 25-μm Au target. Each layer reports the correspondent proton energy obtained from SRIM calculations.

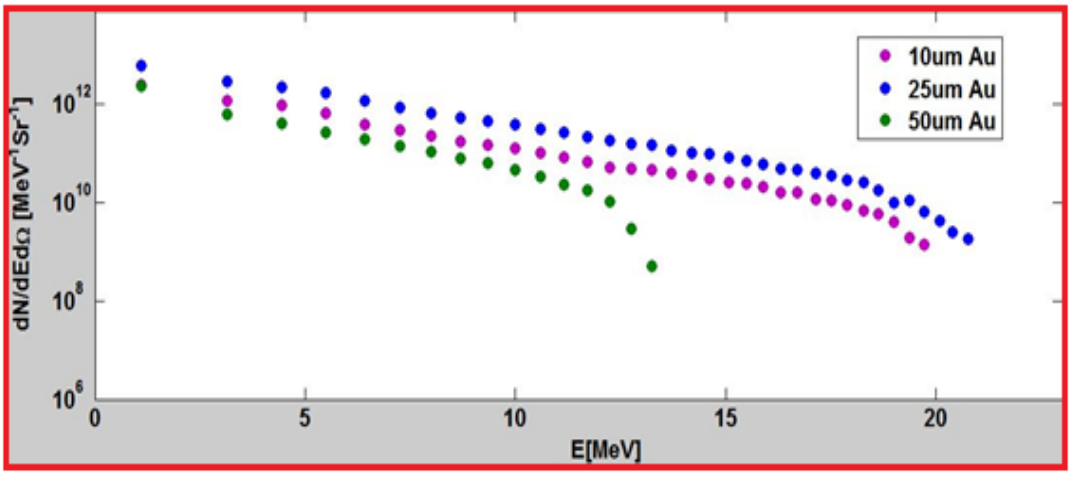

Fig. 58 Laser-driven proton beam energy distribution as a function of proton abundance (calculated in turn as a function of the solid angle Ω). Each curve refers to the laser-target interaction with Au targets of different thicknesses: 10, 25 and 50 μm.

It can be noticed (figure 58) that the energy spectrum corresponding to the 50-μm Au target is characterized by a lower proton fluence and also shows an energy cut-off that the other Au targets thicknesses do not show (discussed in paragraph 2.2). The energy spectrum of the 10 and 25 μm target thicknesses are similar, but the spatial distributions

of protons in terms of homogeneity are not. To strengthen this assertion figure 59 shows, as an example, the comparison between the two 10th layers of the RCF stacks obtained from the laser interaction with the 10 and 25 μm Au targets, which corresponds to the 10 MeV proton contribution. In both cases, we notice a higher fluence at one edge (due to the intrinsic angular distribution of particles with different energies), which decreases towards the periphery more smoothly for the 25 μm target. Therefore, in the experimental campaign we used the 25 and 50 μm Au targets to be able to irradiate the samples with different dose values while the 10 μm Au target was dismissed due to the poor beam homogeneity it gave rise to.

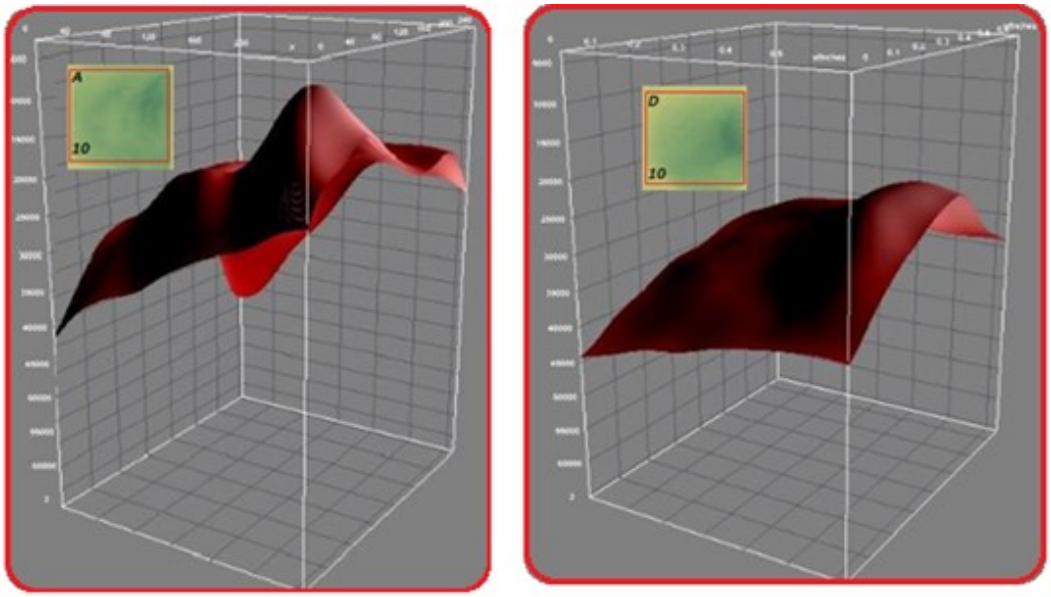

Fig. 59 3D ImageJ reconstruction of the two 10th layers of the RCF stacks (which corresponds to 10 MeV) irradiating the 10 µm (left) and 25 µm (right) target thicknesses.

Regarding the evaluation of the beam dose output values, high-sensitivity EBT3 RCFs were used. They were placed outside the target chamber, just behind the biological sample, in an *ad hoc* frame, as to provide a shot-to-shot characterization of the irradiation dose.
Image plates (IPs) were employed for the beam energy evaluation: their high sensitivity gave the opportunity to directly assess the energy distribution and its spatial uniformity

at the sample position. CR-39 nuclear track detectors, instead, were used to estimate the particles fluence and homogeneity, and to cross-calibrate the IPs. During sample irradiation, IPs or CR39s were placed behind the EBT3 RCFs, which, as mentioned, were in turn positioned behind the biological sample. Figure 60 shows a picture of the detectors configuration mounted on the sample holder and a draft of their arrangement.

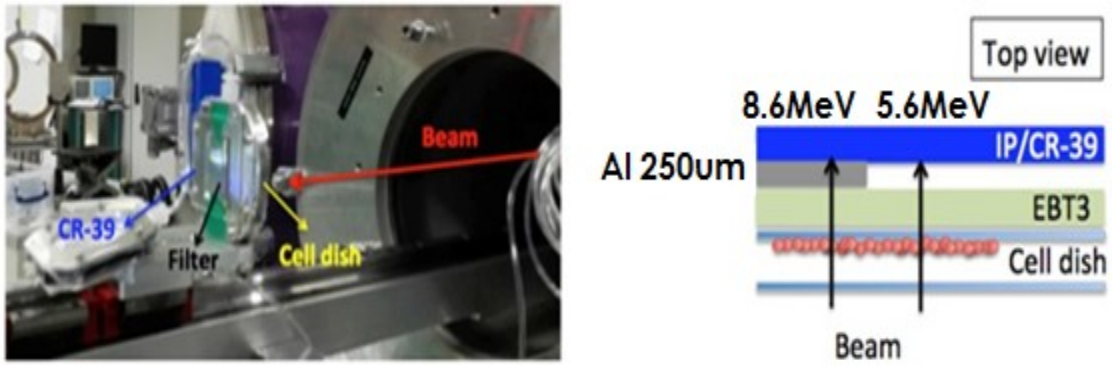

Fig. 60 Left: detectors positioning in the irradiation configuration. Right: scheme of the detectors sequence behind the biological sample.

The overall aim of the use of such a combination of various detectors is to obtain a dose evaluation (by means of the EBT3) as well as an energy distribution along the beam dispersion axis (by means of EBT3, IP/CR39 and Al filters) simultaneously with the irradiation of the biological sample irradiation. This way it was possible to attribute each dose to each position, hence the cell dots. As it can be noticed in the right-hand side of figure 60, an Al filter was placed between the RCF and the IP/CR-39. Several Al filters were employed in order to stop particles of different energies according to their thickness (tab. 1), and to be able to obtain energy cut-off positions on the beam dispersion axis (y) from the IP/CR-39 output analysis.

RCF	*Al thickness [μm]*	*Energy of stopped protons [MeV]*
EBT3	0	5.6
EBT3	250	8.6
EBT3	500	10.6
EBT3	1000	14.6

Tab. 1 RCFs (EBT3) and Al filters thicknesses combination employed in the experimental campaign for proton energy spectrum construction.

The IPs and the scanner used for their reading were both of the Fuji Film Co. and were supplied by the LULI facility as well as an ImageJ tool that converted the image created by the scanner in a 32-bit image. Each pixel value corresponds to the PSL (Photo Stimulated Luminescence) signal whose intensity is proportional to the proton beam energy. The signal was studied as a function of the dispersion axis (y) to precisely evaluate the positions of the energy cut-offs corresponding to the different Al filters.

As an example of the performed measurements, the analysis of the IP and CR-39 using the 310-μm entrance slit, the 250-μm Al filter and the EBT3 behind the biological sample (as shown on the right in figure 60) is reported below. The on-site analysis were performed in collaboration with the LNS-INFN colleagues.

Figure 61 shows the IP signal and its analyzed profile. We notice that two “steps” are present: from top to bottom they correspond to the 5.6 and 8.6 MeV energies cut-offs (figure 61, left). Focusing on the 8.6 MeV cut-off energy value and selecting a region of interest (ROI), represented by the red rectangle, we analyzed its PSL signal as a function of the dispersion axis (figure 61, right). Between 40 and 45 mm on the y-axis, a steep reduction of the signal is noticed. The y-axis positions corresponding to 100%, 50% and 20% of the PSL intensity signals were evaluated. The 50% of the maximum value has been considered as the position corresponding to 8.6 MeV cut-off, while the half distance between 100% and 20% of the signal has been considered as the error: y(8.6MeV)= (42.7 ± 1.1) mm.

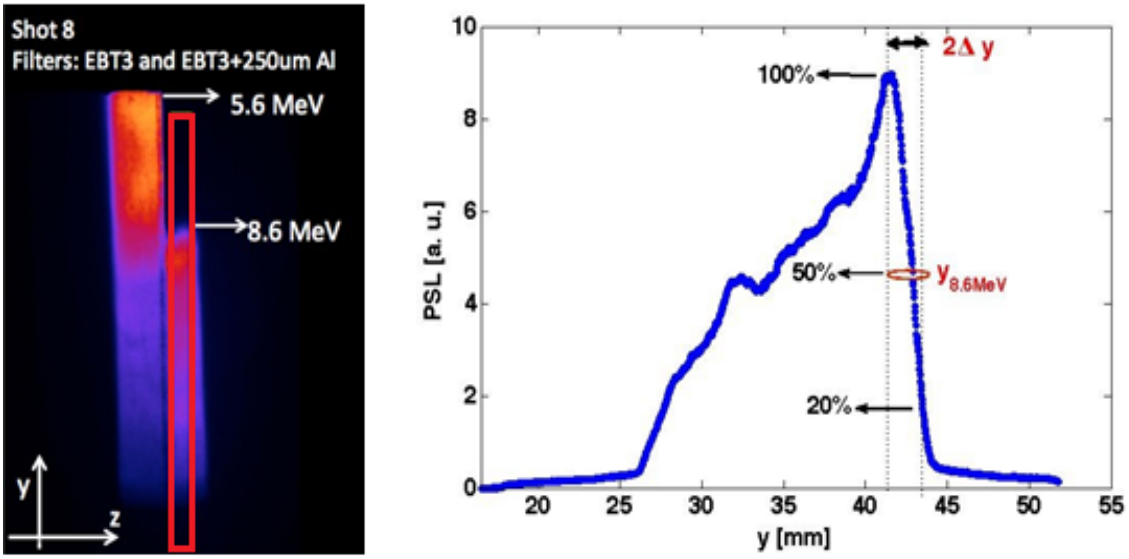

Fig. 61 Example of IP analysis performed during the experimental campaign.

The above described analysis with the IPs was also performed with the CR-39 using exactly the same configuration, except for substituting the two detectors. The CR-39 was subjected post irradiation to an etching procedure by means of a 6.25M NaOH solution at a temperature of 70°C. Outcomes were evaluated at different etching times, starting from 2h up to 8h. The etching procedure is a non-reversible process (described in appendix D). The analysis at each etching time was performed by means of an inverted microscope with a 32X magnification (corresponding to an area of $(1.2\pm0.1)*10^{-3}$ cm^2). Maintaining the solution temperature constant while increasing the etching time leads to a larger particle track diameter; therefore, a compromise between being able to distinguish the single tracks and not incur in the detector saturation has to be found. Another parameter that affects the track diameter, at a constant etching procedure (in terms of solution, temperature and time), is the particles' energy. In fact, particles of the same species but with different energies have a different LET and generate tracks with different diameters. Figure 62 shows, as an example, the fluence values as a function of the dispersion axis (y) of the CR-39 irradiated using the 8.6 MeV Al filter (250 µm).

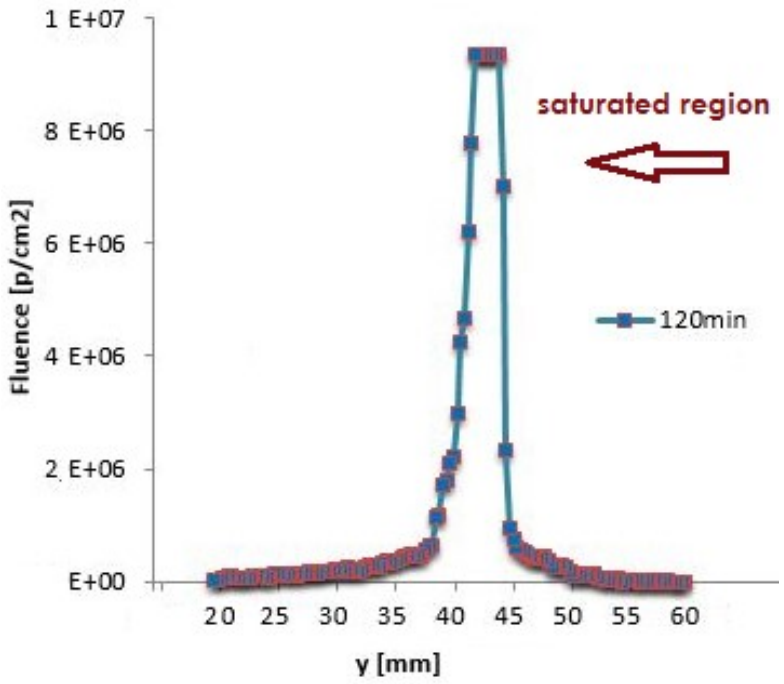

Fig. 62 CR-39 fluence distribution as a function of the dispersion axis (y) obtained after 2h of etching in a solution of 6.25M NaOH at 70°C (using the 8.6 MeV Al filter).

Firstly, we notice that there is a saturated region that corresponds to the lower energy particles and a slight reduction of fluence values before it, corresponding to the higher energy particles. The trend does not have exactly the same shape compared to the previously examined IP (figure 61, right), but it has to be taken into consideration that after 2h of etching high energy particles have diameters non-sufficiently viewable at the microscope. CR-39 calibration curve (figure 63) performed by Szydlowski et al [91], at our same etching conditions, was useful to this purpose. In fact, we realized that after 2h of etching with a 6.25M NaOH solution at 70°C only protons with energies up to about 1.5 MeV had an appreciable diameter. We were using a 250-μm Al filter, which means, for example, that the particles originally revealed as having 1.5 MeV on our detector, had a higher energy. We then increased the etching times and at various time points (30 min) the detectors were viewed at the microscope but the fluence was too high and the detector saturated before we could decently view high-energy particles. Therefore, from the 2h etching analysis (figure 62) we obtained the position corresponding to the 8.6 MeV

energy cut-off and its error as the central point and the half width of the saturated region respectively: y(8.6MeV)= (42.5 ± 1.1) mm.

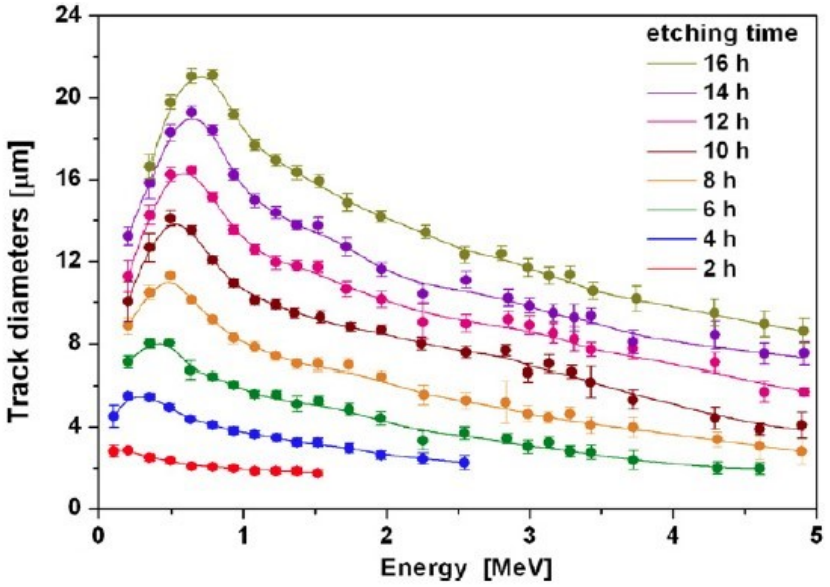

Fig. 63 CR-39 proton calibration curves at different etching times obtained with 6.25M NaOH at 70°C.

There is a good agreement between the IP and CR-39 detectors on the 8.6 MeV energy cut-off position along the dispersion axis (y). The procedures and the analysis above described were carried out for all the irradiated IP and CR39 detectors, and for both slit apertures of 310 and 520 μm, respectively. Table 2 reports the positions along the dispersion axis (y) corresponding to the different energy cut-off values and an acceptable agreement within the errors between the two detectors is noticeable. The higher discrepancies are shown for the 520-μm entrance slit; this is due to the greater particle spatial mixing that occurs compared to the 310-μm slit aperture situation.

E [MeV]	310 μm slit		520 μm slit	
	y_{IP} [mm]	yCR−39[mm]	y_{IP} [mm]	yCR−39[mm]
5.6	51.4±1.1	saturated	55.1±1.7	saturated
8.6	42.7±1.1	42.5±1.1	45.7±1.7	42.5±1.8
10.6	37.7 ±1	39.2 ± 1.1	40.5±1.7	41.3±1.7
14.5	32.9±1.1	n.a.	33.6±1.7	35±1.7

Tab. 2 Energy cut-off positions along the dispersion axis (y) obtained from the IP and CR39 analysis, using the 310 and 520 μm entrance slits apertures.

Figure 64 shows the energy distribution curve along the dispersion axis (y) obtained plotting the data reported in table 2 for the 310 μm slit aperture (as an example) together with the simulation data performed, for comparison, by the LNS-INFN colleagues.

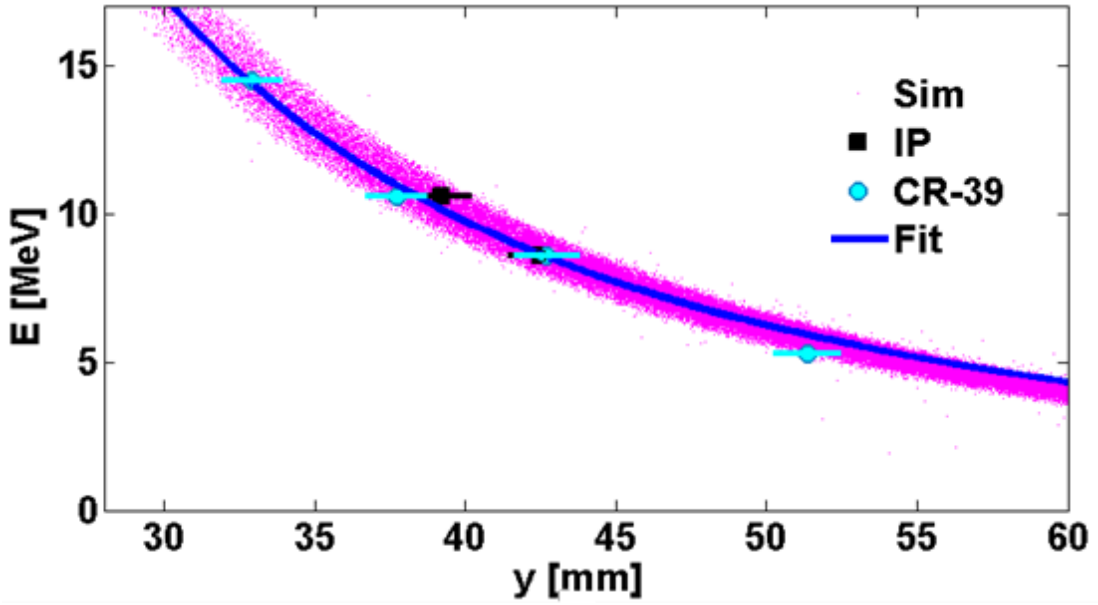

Fig. 64 Energy distribution curve. Experimental data and simulations obtained by using the 310-μm slit entrance aperture are reported.

Thanks to the above energy distribution curve, we were able to reconstruct the mean energy values within the cell spots, seeded always in the same position by employing a

reference frame (as mentioned previously in paragraph 4.1, in three 3x5 mm^2 dots). Table 3 reports the mean energy values corresponding to the three cell dots for both slit entrance apertures; about 10% dispersion must be considered at each energy value.

Num. dot	*y [mm]*	*E [MeV] 310 µm slit*	*E [MeV] 520 µm slit*
1	52.5	5.7	6.2
2	42.5	8.6	9.4
3	34.5	13.1	14.3

Tab. 3 Energy values corresponding to the cell dots positioning in relation to the two different entrance slit apertures.

As previously mentioned, EBT3 RCFs (placed immediately after the mylar sheet where cells are attached) were used as dosimeters. Figure 65 reports how the typical signal of an irradiated RCF looks like post irradiation and the correspondent simulation, for comparison, performed by the LNS-INFN colleagues.

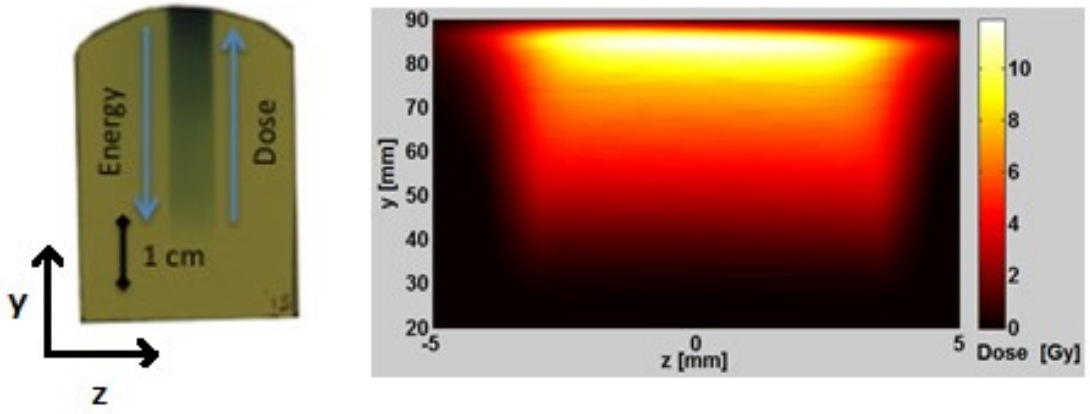

Fig. 65 Left: Typical laser-driven proton irradiated EBT3 with a 310-µm entrance slit aperture compared with its simulation (right).

The mean dose value in each cell dot was evaluated with its standard deviation in correspondence to each laser shot during the LULI campaign. Table 4 reports the latter

dose values in relation to the targets' thicknesses, the biological endpoints and the slit apertures. No significant variation can be observed in the overall dose values obtained employing the 310 and 510 µm slit entrance apertures. This is probably due to the beam fluctuation and/or target inhomogeneity. A dose-rate of about 3×10^9 Gy/s was estimated.

#Shot	Target Au (µm)	1° Dot (y=52.5mm) Dose [Gy]	2° Dot (y =42.5mm) Dose [Gy]	3° Dot (y=34.5mm) Dose [Gy]	Radio-bio end-point	Slit ap. (µm)
1	25	4.4 ±0.9 (23.5%)	1.6±0.2 (14.6%)	0.7±0.1 (19.0%)	Senescence	310
2	25	4.5 ±0.8 (18.0%)	1.1±0.1 (8.5%)	0.9±0.1 (12.9%)	Senescence	310
3	25	4.2 ±0.7 (16.6%)	1.5±0.2 (14.0%)	0.7±0.1 (14.1%)	Senescence	310
4	25	4.2 ±0.6 (14.4%)	1.5±0.2 (13.0%)	0.51±0.07 (14.6%)	Senescence	310
5	25	4.8 ±0.8 (17.1%)	1.4±0.2 (17.0%)	0.47±0.07 (14.3%)	Survival	310
6	50	2.1 ±0.4 (17.6%)	1.1±0.2 (15.0%)	0.68±0.08 (11.5%)	Survival	310
7	25	3.4 ±0.3 (8.9%)	2.7±0.4 (13.1%)	0.73±0.09 (12.3%)	Survival	510
8	25	3.8 ±0.5 (12.5%)	2.1±0.3 (13.0%)	0.5±0.1 (20.4%)	Senescence	510
9	25	4.1 ±0.7 (17.1%)	3.1±0.4 (12.6%)	0.6±0.1 (23.4%)	Senescence	510
10	25	6.3 ±0.8 (12.8%)	2.6 ±0.2 (6.0%)	0.7±0.2 (23.5%)	Senescence	510
11	50	4.3 ±0.6 (13.8%)	1.8±0.3 (17.6%)	0.7±0.1 (16.7%)	Survival	510
12	25	4.1 ±0.7 (17.1%)	1.8±0.3 (17.6%)	0.6±0.1 (23.4%)	Senescence	510

Tab. 4 The laser shots sequence of the LULI experimental campaign is reported. Mean dose values and related standard deviations, measured on a 3x5 mm^2 area, in correspondence to the targets' thicknesses, the radiobiological end-points and the slit entrance apertures are also shown.

4.1.2 Radiobiological results

Clonogenic cellular survival and radiation-induced premature senescence were studied in Human Umbilical Endothelial Vein Cells (HUVEC) to understand the potential clinical impact of laser-accelerated proton beams. Cellular survival as measured by the ability of irradiated cells to maintain their proliferative activity is the gold standard assay for studying cellular radiosensitivity and represents the basis for radiation therapy treatment planning as well as being considered the reference test for other radiobiological assays.

It is, therefore, important to ascertain whether and to what extent cell radiosensitivity is altered by the peculiar physical properties possessed by laser-driven beams.

Stress-induced premature senescence (SIPS), on the other hand, is a process whereby cells exposed to insults such as ionizing radiation enter a permanent state of quiescence. It has attracted growing interest for its possible long-term consequences *in vivo* since accumulation of sub-lethally damaged, ectopically senescing cells may adversely affect normal tissue (and organ) integrity and/or function as well as increase the risk of secondary cancer. Hence, study of radiation-induced senescence is of interest for healthy tissue damage in radiotherapy patients. As is the case for cell survival, it is not known if senescence induction by laser-generated protons differ from that observed following conventionally accelerated particles. SIPS was here studied by means of the histochemical beta-galactosidase enzyme assay, by which nuclei of senescing cells are specifically stained as they express an affinity for this enzyme; the fraction of senescent cells within a given cell population can be measured by examining random fields by light microscopy. The radio-induced effects of laser-driven beams were compared with:

- Conventionally accelerated therapeutic pulsed proton beam achieved by means of a chopper device applied to the *LNS-INFN cyclotron (CT, IT).*
- Conventionally accelerated therapeutic proton beam at *LNS-INFN cyclotron (CT, IT).*
- Low-LET radiation (as a reference) by using a radiogen tube at the Radiation Biophysics Laboratory, *University of Naples (IT).*

As mentioned earlier, the $LULI_{2000}$ laser-driven proton beam irradiation was characterized by extremely high dose-rates, in the order of 10^9 Gy/s. The conventionally accelerated proton beam irradiations (whose regime is continuous) at the LNS-INFN facility were performed at a dose-rate of about 0.03 Gy/s (therefore about 2 Gy/min), which is comparable to that used in radio- and hadrontherapy. An intermediate dose-rate of 2 Gy/s was obtained by means of a chopper device applied to the cyclotron accelerator of the LNS-INFN facility in Catania (figure 66). The chopper was basically a parallel plate capacitor with a distance of 8 cm between the two plates, of which one was set at a potential of 800 V and the other was electrically grounded. When the capacitor was

activated, the beam was deflected due to the electric field, giving rise to a quasi-pulsed beam. Such device was able to produce a 50-ms beam pulse with 500 mHz frequency such that a total dose of 1 Gy was delivered by 10 pulses. Despite dose-rates orders of magnitude lower than a laser-driven proton beam, this irradiation regime was at least two orders of magnitude higher than the clinically used one. Table 5 summarizes the dose-rates values corresponding to each experimental campaign.

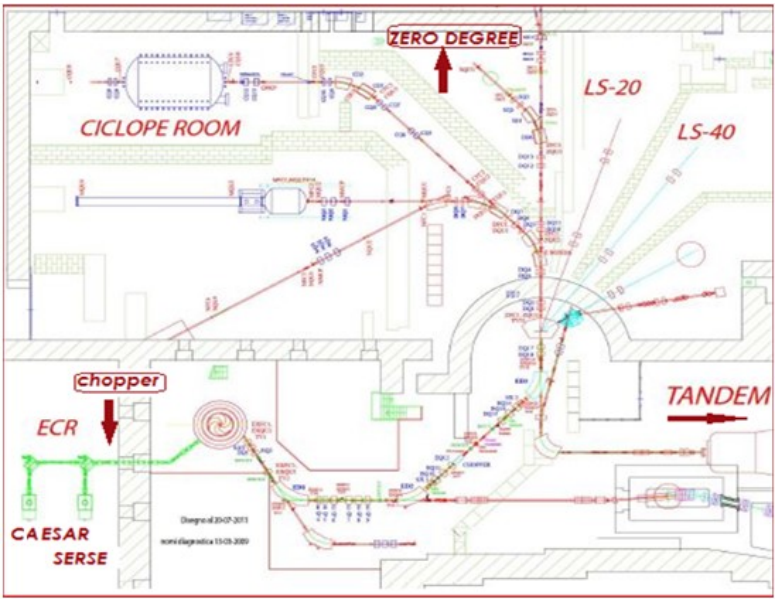

Fig. 66 Scheme of the LNS-INFN superconducting cyclotron facility. The chopper device was positioned right after the ion beam production (by means of the ECRIS, Electron Cyclotron Ion Source, called CAESAR) before its injection into the cyclotron.

Exp. campaign	*Dose rate [Gy/s]*
LULI, laser driven	~10^9 Gy/s
LNS-INFN, pulsed	2 Gy/s
LNS-INFN, conventional	0.03 Gy/s

Tab. 5 Dose-rate values achieved in the experimental campaigns.

The energy differences within the dot-containing dish region reported in table 3 (paragraph 4.1.1) did not correspond to a LET variation able to elicit significantly different biological effects (at least as far as traditional radiobiology is concerned). Hence, it was thought that the best way to analyze the radiobiological laser-driven beam data was for them to be pooled and evaluated as a function of the dose only. In the pulsed and conventional proton beam experiments, irradiations were carried out using beams having as LET the mean value of the laser-driven irradiation LETs. In table 6 the initial beams energy and calculated or estimated LET values incident on the biological samples are reported for each experimental campaign. The energy of the LNS-INFN proton beam employed for the pulsed and conventional irradiations was attenuated by means of degraders in order to obtain LET values comparable to the laser-driven ones.

Exp. campaign	*Initial Energy [MeV]*	*LET [keV/um]*
LULI, laser driven	~6-14 MeV ± 10%	5±2
LNS-INFN, pulsed	60 ± 2%	5
LNS-INFN, conventional	60 ± 2%	5

Tab. 6 Initial beams energies and LET (on cells) values are reported. LNS (pulsed as well as conventional) LET values do not show errors since they are negligible.

In table 7, the dose values corresponding to the pulsed and conventional proton beam irradiations, are reported in relation to the specific radiobiological end-point. Unlike laser-driven beams, where due to intrinsic instabilities (even if keeping constant all the parameters), different dose values at each shot can be obtained (reported in table 4, paragraph 4.1.1), in the case of conventional accelerators we have a reliable stability and reproducibility of the dose delivered.

Radio-bio end-point	*Dose [Gy]*
Survival	0.5 – 1 – 2 – 4 (5 only X-rays)
Senescence	0.5 - 1.5 - 4

Tab. 7 Pulsed and conventional protons as well as X-ray radiation dose values for each radiobiological end-point are reported.

4.1.2.1 Cellular survival: comparison between laser-driven, pulsed and conventionally accelerated proton beams

Cellular survival experimental data were fitted by the equation $SF=e^{-\alpha D-\beta D^2}$ (described in 1.2.1), which represents the formalization of the linear-quadratic model commonly accepted as the best descriptor of cellular radio-response.

HUVEC cellular survival dose-response curves, following laser-driven and conventionally accelerated proton irradiations, are shown in figure 67.

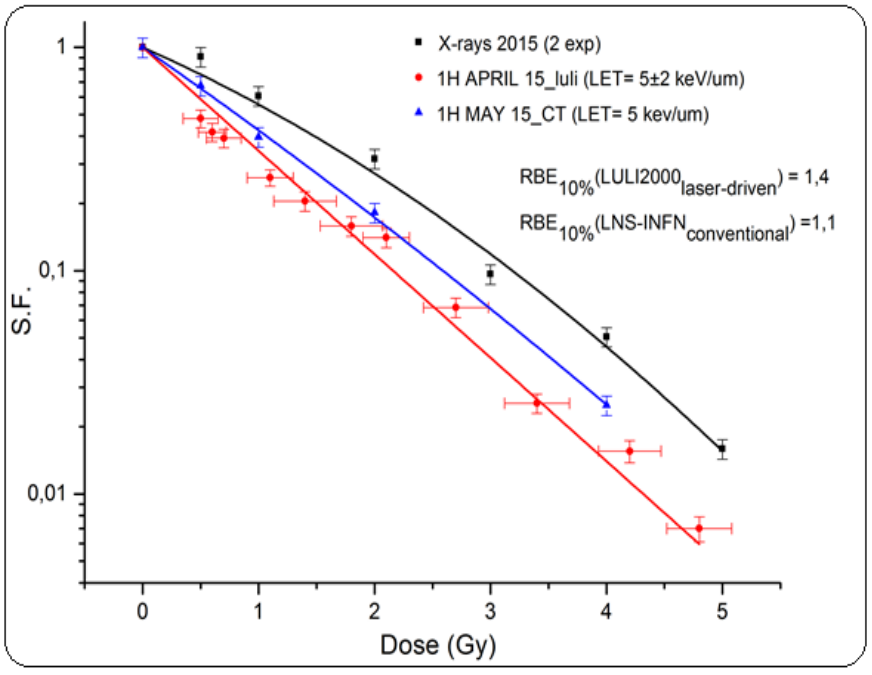

Fig. 67 HUVEC clonogenic survival curves following laser-driven beam (red symbols) and conventionally accelerated beam (blue symbols). Results of X-ray irradiation (black symbols) are shown as a reference for RBE estimation.

In figure 68, the results of the LNS-INFN pulsed beam are added. Table 8 reports the α and β parameters obtained from the fit equations. It can be noted that data from the laser-driven and the pulsed proton beam are best fitted by a linear equation, as the beta parameter is consistent with zero.

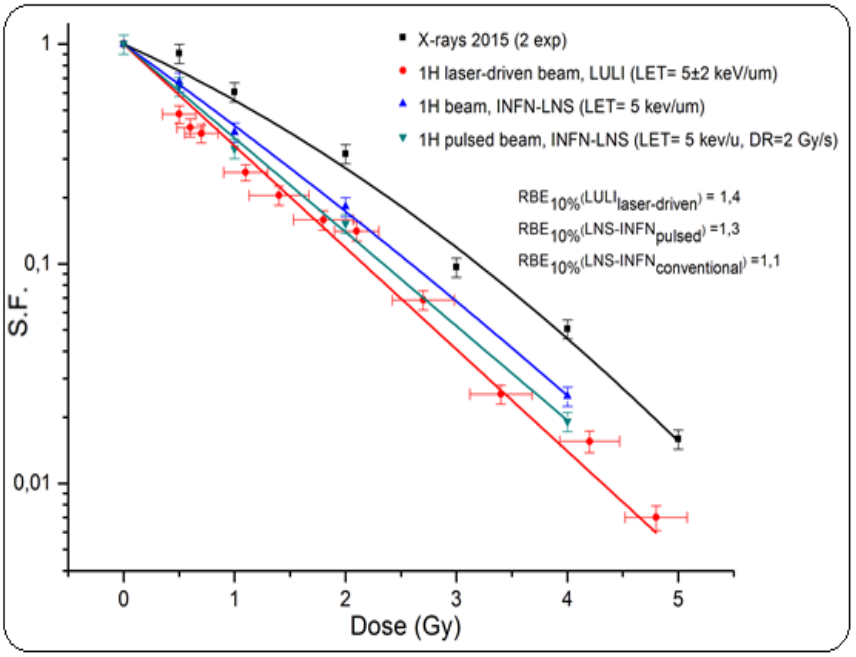

Fig. 68 HUVEC clonogenic survival curves following laser-driven beam (red symbols), conventionally accelerated beam (blue symbols) and pulsed beam (green symbols). Results of X-ray irradiation (black symbols), are shown as a reference for RBE estimation.

Rad. modality	*α(Gy⁻¹)*	*SE α(Gy⁻¹)*	*β(Gy⁻²)*	*SE β(Gy⁻²)*
X-rays	0,578	0,083	0,061	0,020
LULIlaser-driven	1,066	0,082	0,001	0,023
LNSpulsed	0,984	0,069	0,001	0,019
LNSconventional	0,833	0,040	0,022	0,011

Tab. 8 Cellular survival curves α and β parameters correspondent to each experiment with protons accelerated in different manners and X-rays.

Figure 67 shows that although there is no statistically significant difference between the cellular survival to laser-driven and conventionally accelerated proton beams, the former mode of acceleration seems to result in a slightly more efficient cell killing. A few consideration can, in fact, be made. Firstly, both proton beams are more effective than X-rays at causing clonogenic death. This results in Relative Biological Effectiveness (RBE) values, calculated at the 10% level of the surviving fraction using the linear-quadratic equation and from the α and β parameters, estimated to be of 1.4 and 1.1 for laser-driven and conventionally accelerated protons respectively. The latter value agrees with the one commonly accepted and currently used in proton-based hadrontherapy treatment plans and provides a good indication of the reliability of the experimental set-up, hence of the data obtained.

Figure 68 shows the pulsed proton beam cellular survival curve plotted together with the ones from laser-driven and conventionally accelerated proton experiments. It is clear that there appears to be no statistically significant difference between the three curves for the three proton irradiations. However, pulsed beams seem to be more effective than X-rays at causing clonogenic death; this leads to a RBE value of about 1.3.

As reported in table 6 (paragraph 4.1.2), the dose-rate of the pulsed proton beam is orders of magnitude smaller than the one of laser-driven beams, but it is nevertheless two orders of magnitude larger than the ones used in conventional therapy and traditional radiobiology experiments where most data underlying the clinical findings and protocols derive from. If results are confirmed, cellular survival following proton irradiation seem to be influenced, and slightly enhanced, by high and very high dose-rates, and possibly, by the pulsed nature of the beams.

4.1.2.2 Cellular senescence: comparison between laser-driven, pulsed and conventionally accelerated proton beams

The onset of cellular senescence in irradiated cells was assessed for three doses of each experimental campaign carried out (laser-driven, pulsed and conventionally accelerated protons and, for comparison purposes, X-rays). Both at early time post-irradiation (2 days) and at later times: cell cultures were, in fact, followed up and periodically assayed for almost a month following exposure (28 days). The results are shown in figure 69. To our knowledge, these are the first experimental data on premature cellular senescence induced by laser-accelerated particles. Regarding the laser-driven data, in particular, it has to be pointed out that a total of 8 dishes were irradiated (each containing three cell dots treated separately), of which 4 at the time were processed at different time points to improve the statistical robustness of the analysis. Due to the intrinsic shot-to-shot laser input instabilities, we estimated three mean doses at which the three cell dots on each of the 8 dishes were irradiated; they resulted to be (0.6±0.2) Gy, (1.8±0.6) Gy and (4.5±0.8) Gy. Single dose values correspondent to each cell dot in each dish are reported in table 4 (paragraph 4.1.1). The dose values of pulsed, conventionally accelerated protons as well as X-rays (all three used for comparison with laser-driven senescence induction) are reported in table 7 (paragraph 4.1.2).

When examining the results, it can be noticed that all irradiated samples persistently show a significant increase in the induction of senescence compared to controls. The latter are important because they obviously take into account the physiological progression of senescence in non-irradiated cells but also they account for the stress cells are subjected to (besides the irradiation) due, for example, to transportation, irradiation conditions, etc. Because we performed experiments at four different times and under different conditions, it was important to ensure that controls from each experiment showed a similar behavior in their senescing pattern. This is shown in figure 70: the fractions of senescing cells among controls as a function of time vary consistently within the experimental errors.

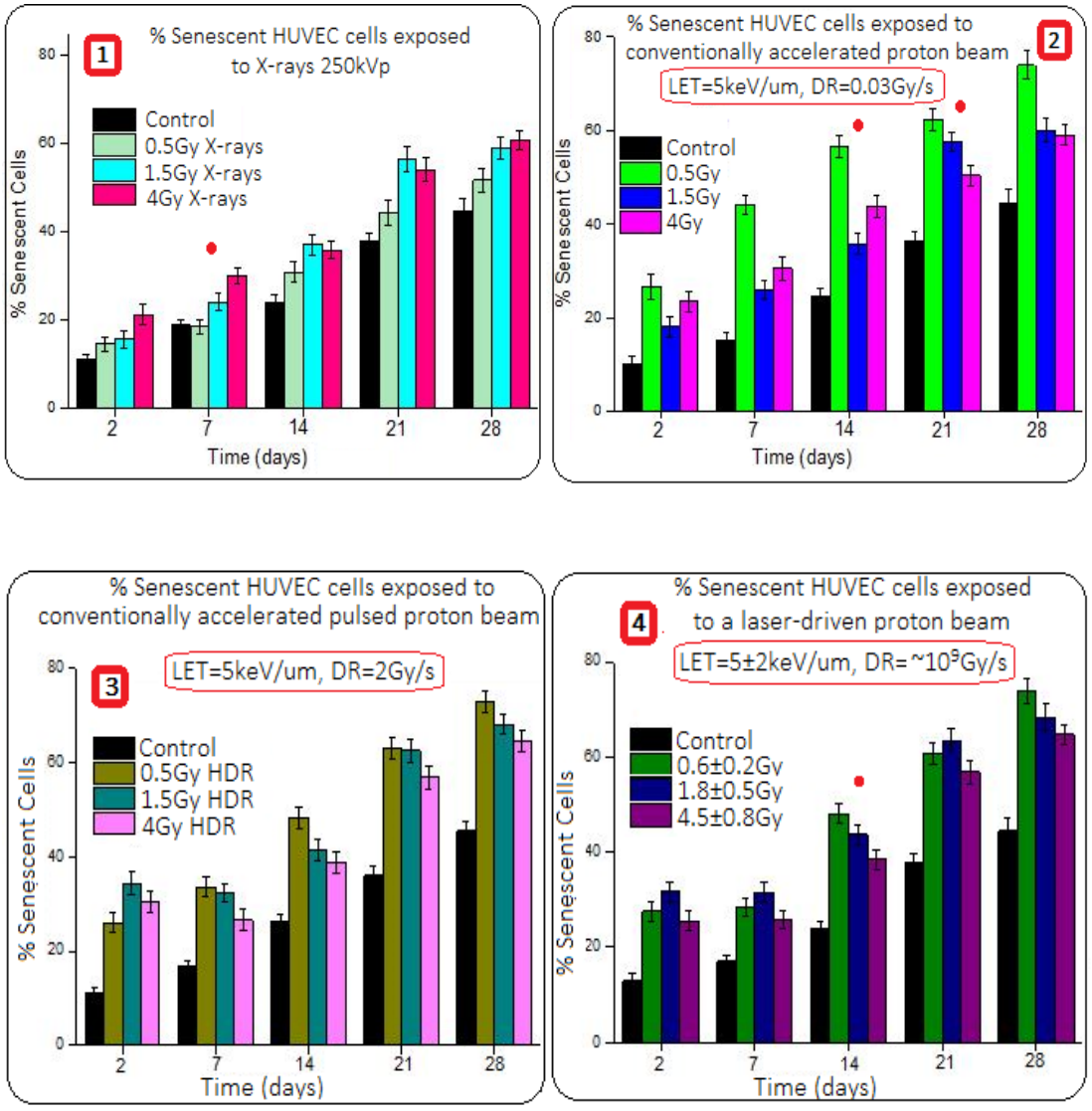

Fig. 69 Percentage of senescent cells as a function of time evaluated at the three examined doses induced by X-rays, conventionally accelerated, pulsed and laser-driven proton beams indicated with numbers 1, 2, 3 and 4 respectively. Red circles point out the time points at which there is a statistically significant difference between the three doses (based on p-value calculations, p<0.05).

In general, when evaluating the percentage of SIPS in each single experiment conducted, the irradiation regime of conventionally accelerated protons (figure 69, n.2) is the only

one to show a clearly statistically significant difference between the lower dose of 0.5 Gy compared to the other two doses of 1.5 and 4 Gy, except for the first time point examined (2 days). For all other cases, there does not seem to be a strong dependence by the dose.

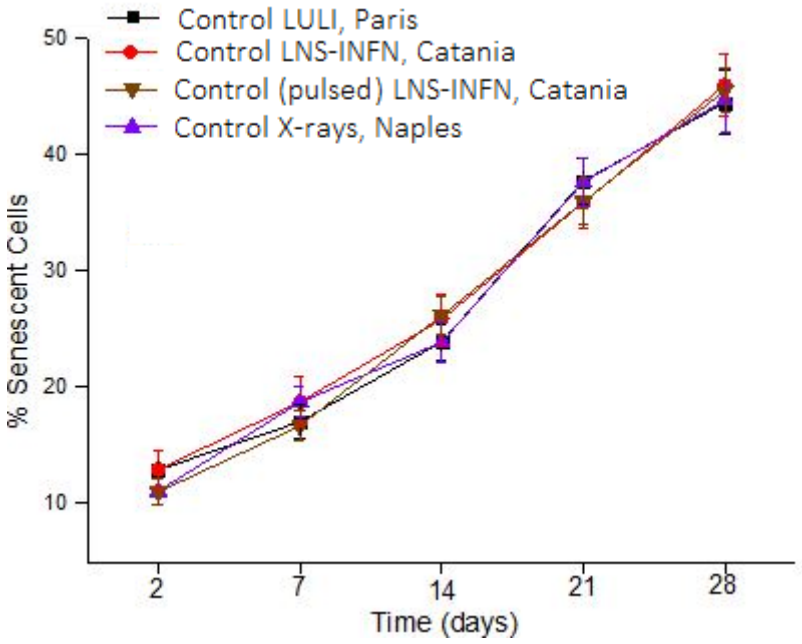

Fig. 70 Percentage of senescence shown in the control cells at the different irradiation facilities as a function of time.

It is interesting to evaluate senescence induction at equal/comparable doses for the different experiments: that is grouping senescence induction by dose as shown in figure 71. In general, since senescence induced by the laser-driven and pulsed beam has a similar trend at all doses and at all time points (as shown in figure 72), it is more meaningful to focus our attention on evaluating the statistically significant differences between laser-driven and conventionally accelerated protons (marked by black triangles in the histograms).

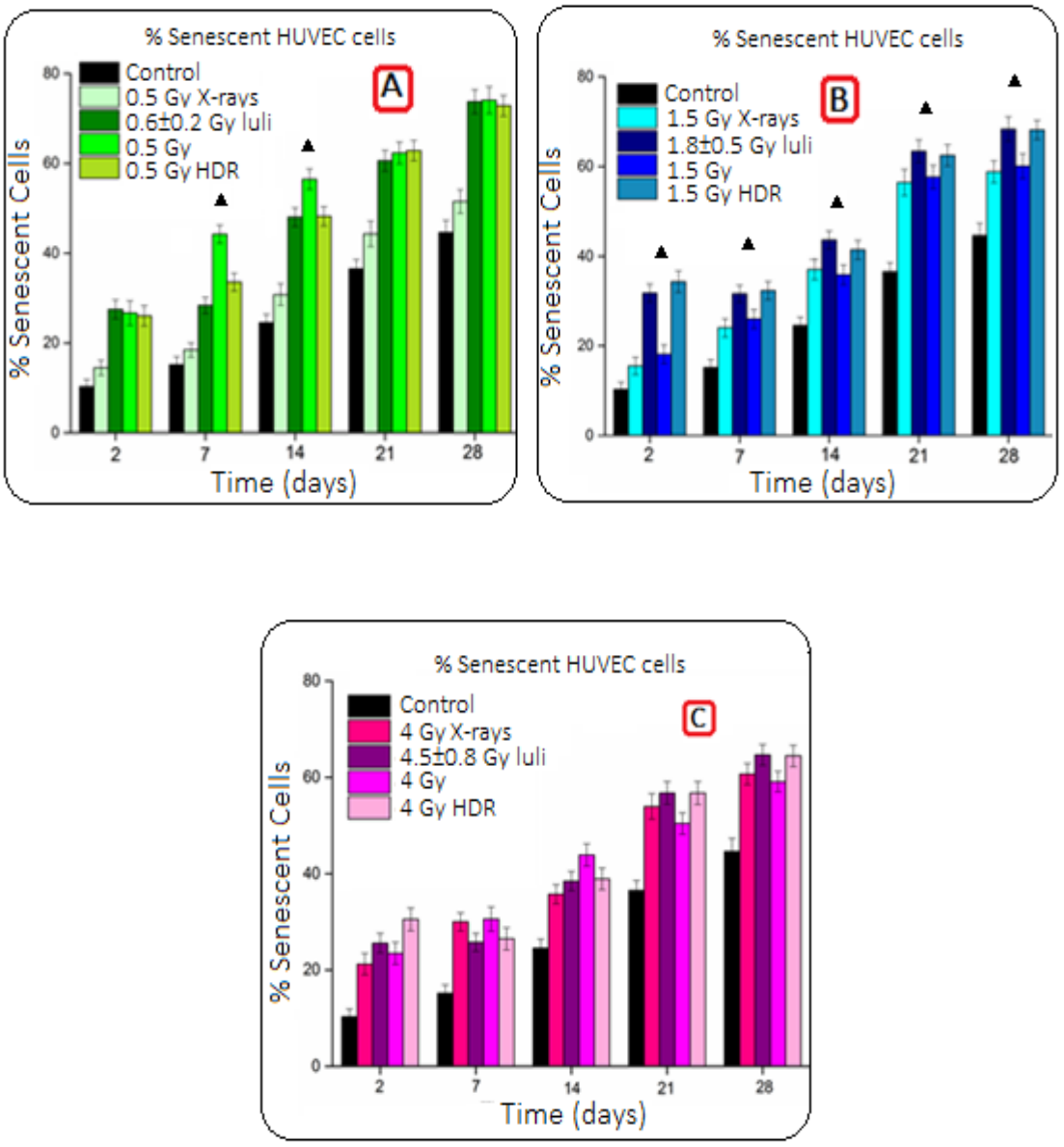

Fig. 71 Senescence induction grouped by doses: 0.5 Gy (0.6±0.2 Gy for laser-driven), 1.5 Gy (1.8±0.5 Gy for laser-driven) and 4 Gy (4.5±0.8 Gy for laser-driven) indicated as A, B and C respectively. Black triangles point out the statistically significant differences between laser-driven and conventionally accelerated protons. The latter assertion is based on p-value calculations ($p<0.05$).

At the lower dose (0.5 Gy, 0.6±0.2 Gy for laser-driven), i.e. the dose that healthy tissues are likely to receive during a radiotherapy session, laser-driven beams induce a lower percentage of senescence in comparison with conventional proton beams, especially at 7 and 14 days. Conversely, at the intermediate dose used in our experiments (1.5 Gy, 1.8±0.5 Gy for laser-driven), i.e. a value close to the fractionated therapeutic dose of 2 Gy administered to the tumor volume, senescence percentages obtained from laser-driven protons are at all times higher than the one induced by the conventionally accelerated proton beam. At the highest dose used (4 Gy, 4.5±0.8 Gy for laser-driven) there appears to be no particular trend to be noticed. In fact, senescence mainly could play a role as a low-dose response being a typical sub-lethal effect. Therefore, at higher dose values other mechanisms (such as interphase cell death by apoptosis or necrosis, for example) are likely to prevail and be influenced by radiation quality and irradiation conditions.

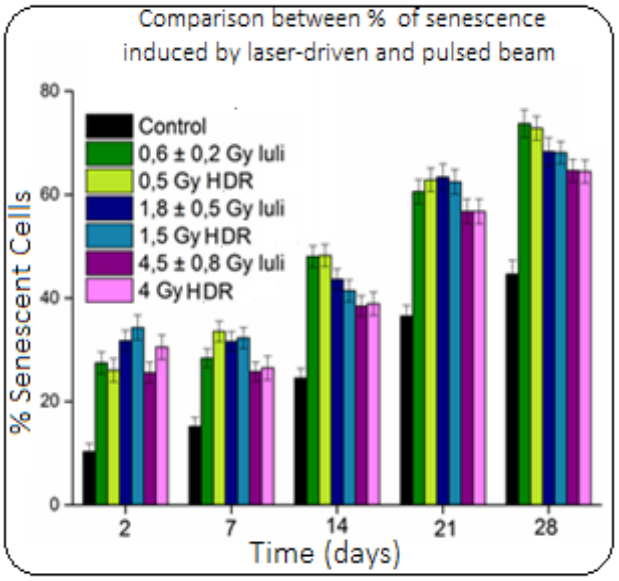

Fig. 72 Comparison between senescence induced by laser-driven and pulsed beams at each time point and at each of the three examined doses.

Conclusions

Cancer is the second cause of death in developed countries right after cardiovascular diseases [1]. Therefore, the interest in discovering more advanced and sophisticated techniques compared to the existing ones is the goal of the scientific community, which involves physicists, radiobiologists and medical doctors.

In recent years, proton radiotherapy has attracted growing interest. The exploitation of accelerated proton beams for cancer treatment, based on the superior ballistic properties of charged particles compared to photons, translates in advantages in terms of dose distribution to tumor and sparing of normal tissue.

Worldwide, the existing hadrontherapy centers that perform patient treatments with charged particles and heavier ions (primarily carbon) are few compared to the demand from potential beneficiaries. One of the main reasons is that today's economic climate has made even more stringent the issue of the costs of building and running a proton radiotherapy facility, thereby limiting the availability of this type of cancer treatment. The need for cost reduction in order to render proton therapy affordable by an increasing number of medical facilities and therefore patients, has stimulated the research and development of new technologies aiming at compact, single-room accelerators that require less initial expenses. Particle acceleration from laser-matter interaction is an emerging technique employing ultra-intense power lasers to produce particle bursts of ultra-high dose-rates. Laser-driven accelerators have been thus proposed for future clinical facilities, in view of reduced costs and operational complexity. In fact, hadrontherapy is only one of the possible applications of laser-driven beams but surely it is the most appealing due to the social repercussion it could have. It is also the most challenging and demanding in terms of beam handling.

The work presented in this thesis has been carried out in the framework of the EU funded project ELIMED and the Italian joint project PLASMAMED funded by INFN (Italian National Institute of Nuclear Physics). Both projects are dedicated to the construction of an amenable laser-driven beam line for medical applications and to the performance of the

mandatory radiobiological tests necessary to validate the possible use in cancer therapy of laser-accelerated particles.

Studies and tests of a crucial component of the whole beam transport line (BTL), the Energy Selector System (ESS), have been successfully carried out at conventional accelerator facilities (LNS and LNL-INFN respectively in Catania and Legnaro, Italy) for device calibration purposes and at an actual laser-driven facility (TARANIS, Belfast, UK). Experimental results were compared with simulations, provided by the LNS-INFN colleagues, and are described in chapter 3. The TARANIS trials pointed out the necessity to employ a collecting/focusing device, the permanent magnetic quadrupoles system (PMQ), in order to maximize particle transmission efficiency prior to their energy selection by the ESS. It has also been understood that the ESS original configuration had to be modified to be able to obtain the best beam behavior (paragraph 3.2.2). The PMQ module has been recently delivered to the LNS-INFN in Catania where preliminary tests are undergoing by means of the 13-MV Tandem accelerator and superconducting cyclotron there based. In the near future, experimental campaigns at proper laser-driven facilities employing the combination of the PMQ and ESS are planned at the TARANIS (Belfast, UK) and at LOA (Paris, Fr) laboratories. The aim is to verify their performance in the configuration that will be then installed at the ELI-Beamlines facility in Prague (CZ), pillar of the ELI (Extreme Light Infrastructure) consortium.

Meanwhile, we considered necessary to investigate whether radiobiological differences existed between laser-driven beams and those currently used in hadrontherapy, from which the former profoundly differ due to their energy spread, ultra-high dose-rate and pulsed nature. In fact, very little data exist on the biological effects of particles with these or similar physical characteristics. The proof-of-principle radiobiological trials were performed at the $LULI_{2000}$ laser-facility (Paris, FR) focusing on two specific end-points: cellular survival and stress-induced premature senescence (SIPS), both employing a normal human cell line, that is Human Umbilical Vein Endothelial Cells (HUVEC). Clonogenic survival is a gold standard assay for studying cellular radio-sensitivity and is the basis for radiation therapy treatment planning. Premature radiation-induced cellular senescence, on the other hand, may have consequences *in vivo* since its accumulation

can affect normal tissue (and organ) integrity and/or function as well as increase the risk of secondary cancer. Hence, study of radiation-induced senescence is of interest for healthy tissue damage in radiotherapy patients. Radiobiological experimental results are shown in chapter 4. It has to be pointed out that these are the first data obtained at a laser facility on such endpoint.

Cellular survival analysis shows that the extremely high dose-rates and pulsed nature of laser-driven beams may at least be considered as effective as the conventionally accelerated protons: as a matter of fact, they actually seem to pint to a slight increase in the efficiency by laser-driven protons compared to current proton-based hadrontherapy in terms of cell death induction. This result is not trivial nor was it at all obvious beforehand given the poorly understood biological consequences of the laser-driven beams.

Regarding cellular senescence induction, these preliminary data allow inferring some interesting conclusions: the fact that the laser-driven proton beams yield a higher percentage of senescing cells at typical therapeutic doses and at the same time induce a lower percentage at low doses, typically affecting healthy tissues, is of relevance in radiotherapy scenarios. It may imply a greater effect at the tumor level (in vivo senescing endothelial cells may reflect disruption of the blood vessels feeding the tumor) and a lessened effect on normal tissues. Hence, if confirmed by future experiments, the implications for a future clinical use of this particle acceleration modality are of great importance.

The use of laser-driven proton beams in medical applications is still at a pioneering stage. However, the studies here presented from both the dosimetry and the radiobiology point of view seem to indicate that laser-based accelerators could be a realistic long-term alternative to conventionally accelerated particles.

Appendix

A. Linear Energy Transfer (LET)

The dose (measured in Gy=J/kg) is a fundamental parameter to quantify the macroscopic absorption of the energy carried by ionizing radiation (IR) against which its biological effects can be assessed, but it does not take into account the intrinsic discontinuous mechanisms by which IR deposits such energy in the traversed medium. Equal doses of radiation of different quality (i.e. sparsely and densely ionizing radiation, paragraph 1.1.1), typically do not cause the same magnitude of a given biological effect. The produced biomolecular lesions are not only strongly influenced by the radiation type but also by the amount of locally absorbed energy; these parameters govern the different distribution of ionization events within an irradiated medium. The spatial localization of ionizing events is called track structure and can be clearly visualized using an immunofluorescence technique. Figure A.1 shows the nuclei of human fibroblasts exposed to sparsely and densely ionizing radiation in which, by means of the foci immuno-chemical test, the phosphorylation of γ-H2AX histone adjacent the DNA double helix breakage sites is revealed and can be visualized. The cytogenetic damage caused by sparsely ionizing radiation appears as a uniform and casual foci distribution within the nucleus, while the foci induced by an equal dose of densely ionizing radiation are tightly localized along the particle tracks [92]. In the attempt to correctly correlate the energy deposition events and the correspondent biological effects, a parameter able to describe the local energy deposition was introduced: it is called the linear energy transfer (LET). This is defined as the energy locally released per unit length in a material and is described by the ratio:

$$LET = \frac{dE}{dl} \left(\frac{keV}{\mu m}\right)$$

with *dE* the average energy locally deposited, and *dl* being the distance travelled by the particle in matter.

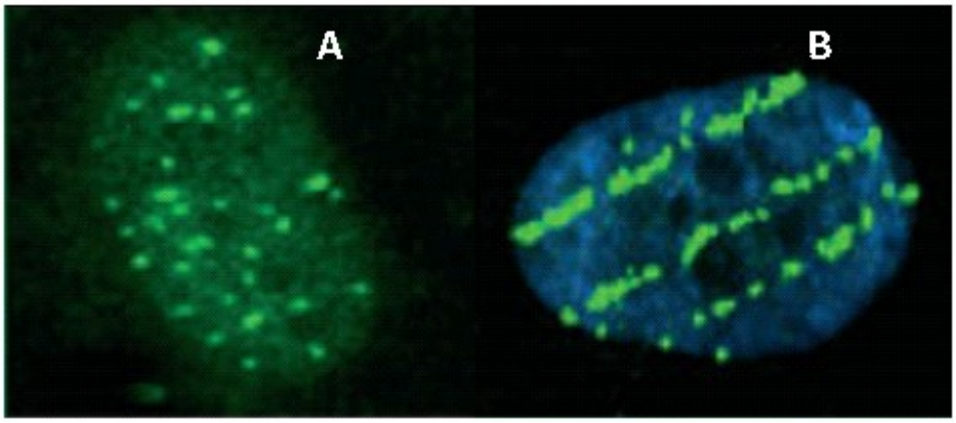

Fig. A.1 Experimental evidence of differing patterns of ionization events produced by sparsely (X-rays, A) and densely (^{12}C ions, B) ionizing radiation by means of an immunofluorescent technique.

Energy release is considered local for electrons produced by energies up to 100 eV thus able to travel for a maximum of 5 μm, hence such restricted LET is defined as LET_{100}. The LET assessment does not take into account that in the ionization process part of the total energy is not locally transferred to matter. In fact, a percentage of the energy is transported "away" from the primary interaction sites through secondary electrons, released in the first ionization event, that then interact with the target atoms; such electrons are called δ-rays. Therefore, when estimating the LET of a beam, both energy deposition processes must be considered: the one due to the interaction of the primary particle with matter and the one due to δ-rays.

The beam track structure is related to the LET; the higher the LET the greater the density of ionization events. Sparsely ionizing radiation is defined as low-LET, while densely ionizing radiation is defined as high-LET. In fact, charged particles due to their physical nature have a higher probability to interact with matter, release energy and therefore cause complex cytogenetic damage, with less chances of being correctly repaired compared to the ones caused by the same dose of low-LET radiation. Figure A.2 schematically shows the path of the ionization events of radiations with different LETs.

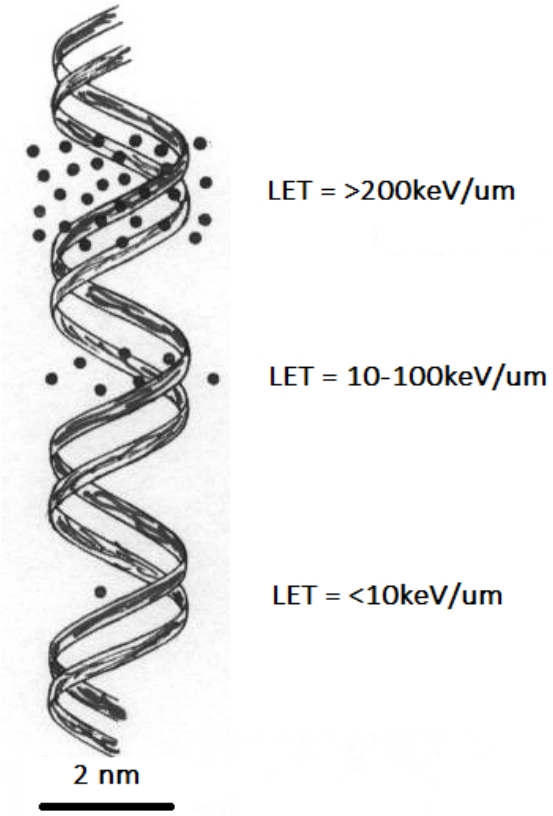

Fig. A.2 Ionization density produced by radiation with different LET values.

B. Radiochromic films (RCF)

Radiochromic films (RCF) are widely used as dosimeters for industrial as well as medical applications in clinical routine, mainly due to their small energy dependency and water-equivalence. RCF are self-developing devices that produce a direct coloration of their active layer consequently to radiation exposure, which do not require any latent thermal, optical nor chemical development or amplification [93]. Furthermore, recent experimental studies have demonstrated that the RCF response is independent from the dose-rate [94]. This feature, in the perspective of a future medical application of laser-driven beams characterized by ultra-high dose-rates, renders RCF a potentially pivotal component of the dosimetric system. RCF are made of layers that differ in terms of numbers and materials according to film quality. The radiation sensitive component

(active layer) is a solid colorless crystalline diacetylene monomer coated with polyester layers. Whether it is X-rays or charged particles, RCF exposure to radiation produces as a reaction the formation of a dark colored polymer, whose darkening is proportional to the dose of the incident radiation. In general, they have a large spatial resolution, of about 2.5 up to 5 μm. The optical density (OD) variations as a function of dose can be measured in different manners, such as: transmission densitometers, film scanners or spectrophotometers. The quicker and more reliable RCF analysis is obtained using RGB (red, green, blue) scanners in the red channel [95]. An RGB scanner is basically composed of three photomultiplier tubes (PMT) sensitive to the red, green and blue light. The precaution that must be taken when using these self-developing detectors is the time after irradiation at which the analysis is recommend to be made, that is of about 24h. Within milliseconds, about 90% of the RCF darkening process is over, but it cannot be neglected that the whole process is completed within 24h.

The RCF used in the experimental campaigns described in this thesis (chapter 3 and 4) are of three different models: EBT3, HD-810 and HD-V2, used according to their operational ranges, as summarized in table B.1 [96].

RCF model	*Operational range [Gy]*
EBT3	0.01-40
HD-810	10-400
HD-V2	10-1000

Table B.1 RCF operational ranges in terms of dose according to their model.

Structures and compositions of the RCF mentioned above are reported in figures B.1, B.2 and B.3.

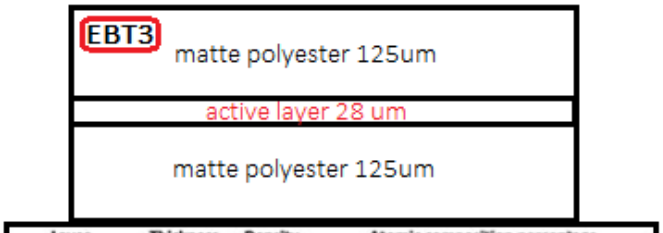

Layer	Thickness [μm]	Density [g/cm³]	Atomic composition percentage				
			C	H	O	Li	Al
Matte polyester	125	1.35	45.30	36.40	18.10	0.10	0.10
Active layer	28	1.2	26.60	55.80	10.70	5.30	1.60

Fig. B.1 Top: layers components and thicknesses of the EBT3 RCF. Bottom: density and atomic composition percentage. Draft is not in scale.

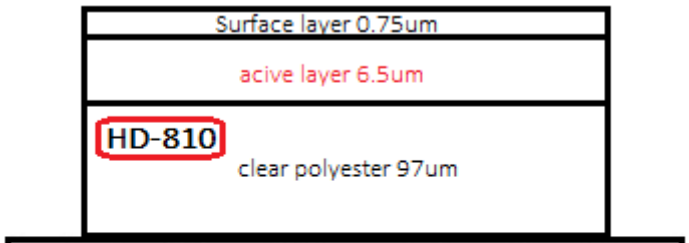

Layer	Thickness [μm]	Density [g/cm³]	Atomic composition percentage			
			C	H	O	N
Clear polyester	97	1.35	45.45	36.36	18.19	
Active layer	6.5	1.08	29.14	56.80	7.12	6.94
Surface layer	0.75	1.2	24.36	55.22	12.82	7.6

Fig. B.2 Top: layers components and thicknesses of the HD-810 RCF. Bottom: density and atomic composition percentage. Draft is not in scale.

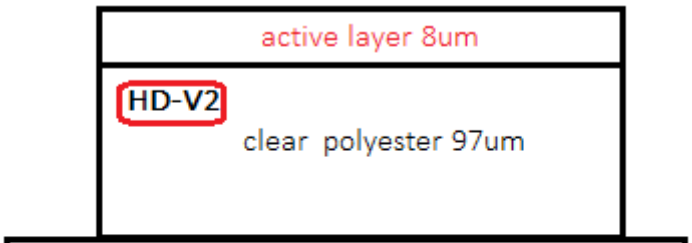

Layer	Thickness [μm]	Density [g/cm³]	Atomic composition percentage			
			C	H	O	N
Clear polyester	97	1.35	45.45	36.36	18.19	
Active layer	8	1.08	29.14	56.80	7.12	6.94

Fig. B.3 Top: layers components and thicknesses of the HD-V2 RCF. Bottom: density and atomic composition percentage. Draft is not in scale.

C. Image Plates (IP)

Image Plates (IP) detectors were first developed by Fuji and Kodak and nowadays are widely used for medical applications, especially for X-ray imaging, but they are also sensitive to ions and to a wide energy spectrum as well [97]. They can be reused several times after radiation exposure (following a specific procedure after each use), they are not sensitive to electromagnetic noise and have a great spatial resolution [98]. The latter is limited only by the scanner necessary to analyze them, which depending on the model, generally can vary between 25 up to 50 μm. IP are currently used for laser-driven beam diagnostics, such as the experiments carried out and described in this thesis (chapter 3 and 4).

An IP is a flexible image sensor (which appears as a plastic sheet) typically composed of three layers; a protective layer, an active layer (photo-stimulable phosphor) and a polyester support (figure C.1).

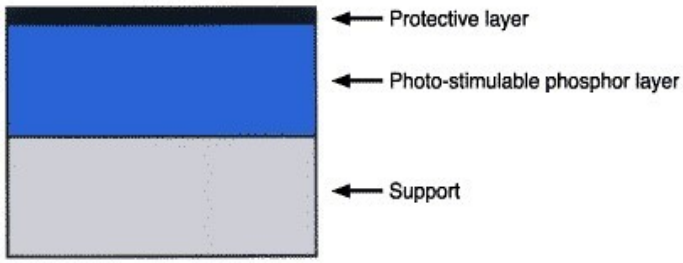

Figure C.1 Typical IP structure is shown.

The active layer composition is usually of crystals (grain size of about 5 µm) of a photo-stimulable phosphor of barium fluorobromide containing traces of bivalent europium as a luminescence center, formulated as BaFBr:Eu^{2+}, and uniformly coated on a polyester support film.

During irradiation, particles pass through the phosphor layer and Eu^{2+} is ionized in Eu^{3+}. Ejected electrons enter the conduction band of the phosphor crystal and remain trapped in its lattice defects called "F-centers". Therefore, IP are able to store the energy of the initial beam until stimulated by a second illumination using a scanner. The light that the

latter emits, excites the trapped electrons (in the “F-centers”) into the conduction band where they recombine with the Eu^{3+} ion, releasing a photon characterized by a blue-violet (λ= about 400 nm) luminescence wavelength. The photo-stimulated luminescence (PSL) signal is then collected by a photomultiplier tube (PMT) through a light collection guide and is converted into electric signals. The output is then processed, through amplification and digitalization, assigning a PSL-value at each scanned pixel. The total electric signal is proportional to the energy of the primary beam that interacts with the IP. Figure C.2 schematically shows the IP reading principle [99].

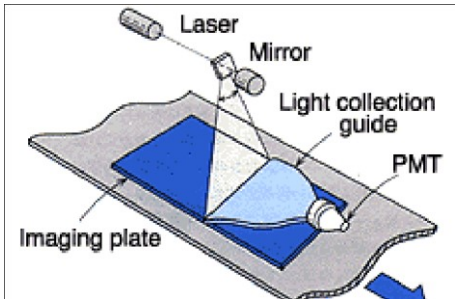

Fig. C.2 IP reading principle: The radiation-exposed IP is scanned with a focused laser beam. The PSL signal released is collected into a photomultiplier tube (PMT) through a light collection guide and is then converted to electric signals [99].

IP have an energy-dependent response given a specific ion, therefore protons with different energies produce different signals. IP reading should be performed in a dark room in order to minimize the signal loss caused by the environmental light. After the reading procedure process, between 60-90 % of the stored energy is released depending on the reader model. In order to be able to reuse the IP a de-excitation procedure is necessary. This is performed using commercial dedicated scanners designed for medical imaging; the eventual IP residual stored energy can be completely erased by 10-15 minutes exposure to environmental light. The detector is then ready to be reused [100].

D. CR-39 nuclear track detectors

CR-39 are solid-state nuclear track detectors commonly used for ions fluence and/or energy evaluation. They appear as a clear rigid plastic made by polymerization of diethyleneglycol bis allylcarbonate (ADC) resin, with a density of 1.30 g/cm^3 and its chemical formula is $C_{12}H_{18}O_7$. The abbreviation CR-39 stands for "Columbia Resin #39", because it was the 39th formula of a thermosetting plastic developed by the "Columbia Resins project" in 1940 [101].

The peculiarity of CR-39s is that they are able to reveal single ions but they are non-sensitive to X-rays. They are commonly used in combination with other detectors to perform cross calibrations between two or more devices in high-energy, nuclear physics as well as laser-driven accelerated beams experiments.

The interaction of ions with energies greater than 100 keV with the CR-39 detector causes a track of broken molecular chains and free radicals along their trajectory. At a given atomic number (Z), the particles track diameter increases as energy decreases while, at a given energy, particles with a higher atomic number (Z) generate tracks with greater diameters. Particle tracks are then made visible by chemical etching in worm and concentrated solutions that could be NaOH or KOH. The size of tracks gets larger with increasing etching times and, at a fixed etching time, they are larger for lower energy particles, as shown in figure D.1. Etching solution temperatures have an influence on track diameters; equally as important is the fact that the chosen temperature has to be stable during the procedure in order to obtain a uniformly and homogeneously etched detector (figure D.2) [102]. After the etching procedure, tracks are revealed by means of optical microscopes. The number of counted tracks gives information regarding the incident beam fluence and according to their spatial distribution, homogeneity evaluations can be made. Furthermore, energy spectroscopic analysis can also be performed by estimating the track areas.

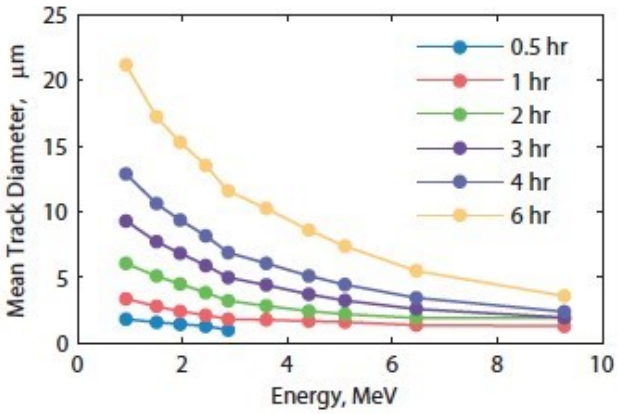

Fig. D.1: Proton track diameters as a function of mean incident energy at different etching times is reported. Etching solution: NaOH, 6N [102].

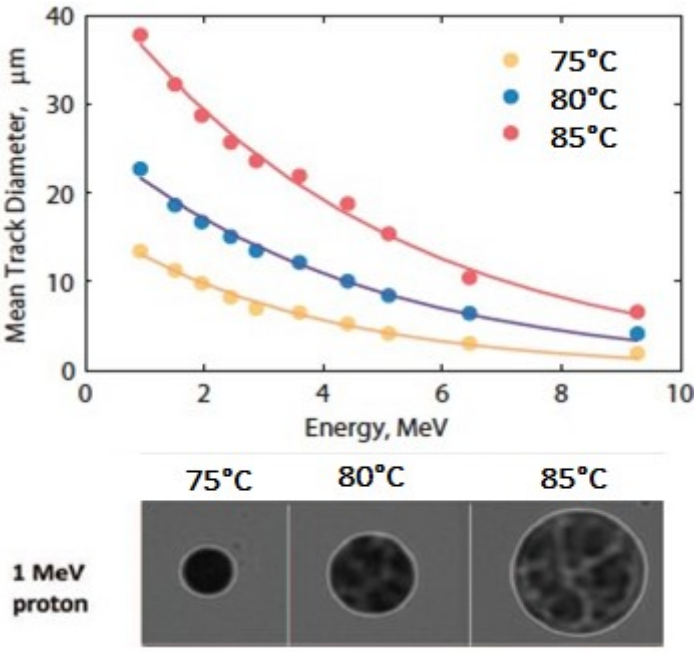

Fig. D.2 Top: Proton track diameters as a function of mean incident energy at different etching temperatures is reported. Etching solution: NaOH, 6N. Etching time: 6h. Bottom: 40x magnification microscope images of 1 MeV proton tracks at increasing etching temperatures of 75, 80 and 85°C are shown. Tracks non-uniformity worsens as temperatures increase [102].

Bibliography

[1] Vermorken, *Towards coordination of cancer research in Europe*, IOS Press, (1994).

[2] Newhauser W. et al., *Assessing the risk of second malignancies after modern radiotherapy*, Nature Rev. Cancer (2011).

[3] Particle Therapy Co-Operative Group (PTCOG), *Particle therapy facilities in operation,* http://www.ptcog.ch/index.php/facilities-in-operation.

[4] Particle Therapy Co-Operative Group (PTCOG), *Particle therapy facilities in a planning stage*, (2001).

[5] Joshi C. et al, *Plasma Accelerators at the Energy Frontier and on tabletops*, Phys. Today 56 (2003).

[6] Cirrone G.A.P. et al. *ELIMED: a new hadron therapy concept based on laser driven ion beams SPIE Proceedings of SPIE*, Medical Applications of Laser-Generated Beams of Particles III, vol. 8779, (2013).

[7] Schillaci F. et al. ELIMED, *MEDical and multidisciplinary applications at ELI-Beamlines Journal of Physics*, Conference Series, (2014).

[8] Schmid T.E et al. *No evidence for a different RBE between pulsed and continuous 20 MeV protons,* Radiat. Res., (2009).

[9] Bohr N., *On the Constitution of Atoms and Molecules*, Phil.Magazine, (1913).

[10] Karam, *Inconstant sun: how solar evolution has affected cosmic and ultraviolet radiation exposure over history of life on Earth*, Health Phys. (2003).

[11] Miller, Organic compound synthesis on the primitive Earth, Health phys. (2003).

[12] Oparin, *The origin of life*, Macmillan (1938).

[13] Rontgen, *Annallen del physik* (1898).

[14] Manti et al, *Cooperative biological effects between ionizing radiation and other physical and chemical agents*, Mut. Res-Rev (2012).

[15] Markus et al, *Clonal growth in vitro of epithelial cells from normal human tissues*, J. exp. Med (1956).

[16] Puck & Markus, *Action of X-rays on mammalian cells*, J. exp. Med (1956).

[17] Campisi, *Cellular senescence as a tumor-suppressor mechanism*, Trends Cell Biol. (2001).

[18] Hayflick, *Moorhead PS: The serial cultivation of human diploid cell strains*, Exp. Cell Res (1961).

[19] Serrano et al, *Putting the stress on senescence*, Curr. Op in Cell Biology (2001).

[20] Lopez M: *Apoptosi e senescenza cellulare,* Oncologia medica pratica (2010).

[21] Hall E. et al, *Radiobiology for the radiologist*, (2006).

[22] Ben-Porathet al, *The signals and pathways activating cellular senescence*, Int J. Biochem Cell Biol (2005).

[23] Dimri, *A biomarker that identifies senescent human cells in culture and in ageing skin in vivo*, Proc Natl Acad Sci USA (1995).

[24] World Health Organization http://www.who.int/mediacentre/factsheets.

[25] Alexandre*, Optimization of In-Beam Positron Emission Tomography for Monitoring Heavy Ion Tumor Therapy* (2005).
[26] Brahme, *Recent advances in light ion radiation therapy,* International Journal of radiation oncology biol. Phys. (2004).
[27] Laungauer et al, *Genetic instabilities in human cancers*, Nature (1998).
[28] Cucinotta et al, *Nuclear interactions in heavy ion transport and event based risk models,* Radiation Protection Dosimetry (2011).
[29] Newhouser, Durante, *Assessing the risk of second malignancies after modern radiotherapy,* Nature (2011).
[30] Maalouf, Durante et al, *Biological effects of space radiation on human cells: history, advances and outcomes,* Journal of Radiation Research (2011).
[31] Fournier et al, *Interrelation amongst differentiation, senescence and genetic instability in long-term coultures of fibroblasts exposed to different radiation qualities*, Radiation Biology/Oncology (2007).
[32] Manti et al, *Misura e modellizzazione di anno citogenetico lungo la curva di Bragg di ioni accelerati (MIMO-BRAGG, INFN funded project).*
[33] Agodi et al, *Heavy ions fragmentations measurements at intermediate energies in hadrontherapy and spatial vehicles shielding,* Nuclear Science Symposium Conference Record, (2007).
[34] Nikjoo et al, *Experimental verification of track structure models,* International Journal of radiation Biology (1998).
[35] Vecchio, Cirrone et al, *A PET Prototype for "in-beam" monitoring of proton therapy,* IEEE Transactions on Nuclear Science (2009).
[36] Hall H., *Intensity-modulated radiation therapy, Protons and risk of second cancers,* International Journal oncology biol. Phys. (2006).
[37] K. Flippo et al, *Forward ion acceleration in thin films driven by a high-intensity laser*, Phys. Rev. Lett., (2000).
[38] E. Clark et al, *Measurements of energetic proton transport through magnetized laser from intense laser interactions with solids*, Phys. Rev. Lett., (2000).
[39] R. A. Snavely et al. *Intense high-energy proton beams from petawatt-laser irradiation of solids*, Phys. Rev. Lett., (2000).
[40] M. Borghesi et al*., Ion acceleration by superintense laser-plasma interaction*, Rev. Mod. Phys., (2013).
[41] K. Ledingham and W. Galster, *Laser-driven particle and photon beams and some applications*, New Journal of Physics, (2010).
[42] Busold S., *Construction and characterization of a laser-driven proton beamline at GSI*, PhD thesis, Technische Universitat Darmstadt, (2014).
[43] G. Cook, *Pulse Compression-Key to More Efficient Radar Transmission*, IEEE P. IRE (1960).
[44] Strickland D. and G. Mourou G., *Compression of amplified chirped optical pulses*, Opt. Commun., (1985).
[45] S. Eliezer, *The Interaction of High-Power Laser with Plasmas*, (2002).

[46] E. Lefebvre et al, *Nonlinear electron heating in ultrahigh-intensity-laser-plasma interaction*, Phys. Rev. *(*1897).
[47] M. I. Santala et al, *Effect of the plasma density scale length on the direction of fast electrons in relativistic laser-solid interactions*, Phys. Rev. Lett. (2000).
[48] A. Vlasov, *On Vibration Properties of Electron Gas*, J. Exp. Theor. Phys. (1938).
[49] Wilks, S. C. et al, *Energetic proton generation in ultra-intense laser-solid interactions*. Phys. Plasmas (2001).
[50] G. E. Cook, *Pulse Compression-Key to More Efficient Radar Transmission*, IEEE Proceedings IRE (1960).
[51] Perry M*, Multilayer dielectric gratings: increasing power of light,* Science & Technology Review September, (1995).
[52] P. Drude, *Ueber fernewirkungen*, Ann. Phys., (1897).
[53] Gibbon, *Short Pulse Laser Interactions with Matter*, Imp College Press (2005).
[54] *A Superintense Laser–Plasma Interaction Theory Primer*, (2013).
[55] Bauer et al, *Relativistic ponderomotive force, uphill acceleration, and transition to chaos*, Phys. Rev. Lett., (1995).
[56] Nürnberg, F., *Laser-Accelerated Proton Beams as a New Particle Source*, PhD thesis, TU Darmstadt (2010).
[57] S. A. Gaillard et al., *Nearly 70 mev laser-accelerated-proton beams from micro-cone targets via laser grazing,* Phys. Rev. Lett*.* (2010).
[58] S.C. Wilks et al., *Energetic proton generation in ultra-intense laser-solid interactions*, Phys. Plasmas, (2001).
[59] M. Borghesi et al*., Ion acceleration by superintense laser-plasma interaction*, *Rev.* Mod. Phys., (2013).
[60] L. Robson et al., *Scaling of proton acceleration driven by petawatt-laser-plasma interactions,* Nat. Phys., (2007).
[61] J. Fuchs et al., *Laser-driven proton scaling laws and new paths towards energy increase*, Nature Physics, (2006).
[62] S. Rossi, The status of CNAO, Eur. Phys. J. Plus (2011).
[63] CNAOs website, www.fondazionecnao.it.
[64] U. Linz and J. Alonso., *What will it take for laser driven proton accelerators to be applied to tumor therapy?,* Phys. Rev. Special Topics Accel. and beams, (2007).
[65] ELI website, www.eli-beams.eu.
[66] S.V. Bulanov, *Feasibility of using laser ion accelerators in proton therapy,* Plasma Physics Reports*, (2002).*
[67] INFN ELIMED proposal, *2013*.
[68] A. Tramontana et l., *A transport beamline solution for laser-accelerated proton beams at elibeamlines*, Il Nuovo Cimento (2015).
[69] M. Maggiore et al., *Innovative handling and transport solutions for laser-driven ion beams*, AIP Conf. Proc. 1546 (2013)
[70] A.Tramontana et al., *The Energy Selection System for the laser-accelerated proton beams at ELI-Beamlines*, IPRD (2013).
[71] P. Castro., *Beam trajectory calculations in bunch compressors*, DESY Tech (2003).

[72] L. P. Chau et al., *Bunch compressor for intense proton beams.,* Proc. LINAC, (2010).
[73] A.V. Kuznetsov et al., *Efficiency of ion acceleration by a relativistically strong laser pulse in an underdense plasma,* Plasma Phys. Rep, (2011).
[74] D. Haberberger et al., *Collisionless shocks in laser-produced plasma generate monoenergetic high-energy proton beams*, Nature Phys., (2012).
[75] T. Dzelzainis et al., *The taranis laser: A multi-terawatt system for laser-plasma investigations,* Laser and particles beams, (2010).
[76] D. S. Hey et al., *Use of gafchromic film to diagnose laser generated proton beams,* Rev. Sci. Instrum., (2008).
[77] *Focusing of charged particles*, New York Academic Press, (1967).
[78] *Optics of charged particles*, Academic Press Inc., (1987).
[79] Wilson R., *Radiobiological use of fast protons*, Research Laboratory of Physics, Harvard University, Cambridge, Massachusetts (USA), (1946).
[80] S. Auer et al*., Survival of tumor cells after proton irradiation with ultra-high dose rates,* Radiat. Oncol., *(2011).*
[81] S. D. Kraft et al., *Dose-dependent biological damage of tumour cells by laser accelerated proton beams*, New Journal of Physics, (2010).
[82] A. Yogo et al., *Measurement of relative biological effectiveness of protons in human cancer cells using a laser-driven quasimonoenergetic proton beamline*, Appl. Phys. Lett., (2009).
[83] A. Yogo et al., *Measurement of dna double-strand break yield in human cancer cells by highcurrent, short-duration bunches of laser-accelerated protons,* Japanese Journal of Applied Physics, (2011).
[84] D. Doria et al., *Biological effectiveness on live cells of laser driven protons at dose rates exceeding 109 gy/s*, AIP Advances, (2012).
[85] S. Kar et al., *First results on cell irradiation with laser-driven protons on the taranis system*, AIP Conf. Proc, (2013).
[86] F. Fiorini et al., *Dosimetry and spectral analysis of a radiobiological experiment using laser-driven proton beams.,* Phys. Med. Biol., (2011).
[87] K. Zeil et al., *Dose-controlled irradiation of cancer cells with laser-accelerated proton pulses*, Appl. Phys. B, (2013).
[88] LULI website*,* www.luli.polytechnique.fr.
[89] D. S. Hey et al., *Use of gafchromic film to diagnose laser generated proton beams,* Rev. Sci. Instrum., (2008).
[90] F. Fiorini et al., *Dosimetry and spectral analysis of radiobiological experiment using laserdriven proton beams.,* Phys. Med. Biol., (2011).
[91] A. Szydlowski et al., *Application of solid-state nuclear track detectors of the cr-39/pm-355 type for measurements of energetic protons emitted from plasma produced by an ultra-intense laser*, Radiation Measurements, (2009).
[92] F. Cucinotta & Durante M, *Cancer risk from exposure to galactic cosmic rays: implications for space exploration by human beings*, Lancet Oncology, (2006).
[93] G. Dempsay, *Validation of a precision radioch. film dosimetry system for quantitative two-dimensional imaging of acute exposure dose distribution*, *Med Phys.*, (2000).

[94] Karsch L. et al., *Dose rate dependence for different dosimeters and detectors: Tld, osl, ebt films and diamond detectors*, Med. Phys., (2012).
[95] S. Chiu-Tsao, *Dose response characteristics of new models of gafchromic films: Dependence on densitometer light source and radiation energy*, Med Phys., (2004).
[96] URL http://www.ashland.com/products/gafchromic-radiotherapy-films.
[97] Gales S. and Bentley C., *Image plates as x-ray detectors in plasma physics experiments*, Review of scientific instruments, (2004).
[98] A. Mancic et al., *Absolute calibration of photostimulable image plate detectors used as (0.5–20 mev) high-energy proton detectors*, Review of scientific instruments, (2008).
[99] http://home.fujifilm.com/products/science/ip/feature.html.
[100] Z. Dauter and S. Wilson, *Imaging plates in sinchrotron and conventional x-ray crystallographic data collection*, Acta Physica Polonica (1994).
[101] http://corporate.ppg.com/Home.aspx.
[102] N. Sinenian et al., *The response of cr-39 nuclear track detector to 1-9 MeV protons.*, Review of Scientific Instruments, (2011).

Acknowledgments

I would like to thank my mentor, Dr. Lorenzo Manti, for his support and patience during these years. Lorenzo, many things have changed since we first met seven years ago when I asked you to be the tutor of my bachelor thesis. Thanks to your constant and daily supervision, I feel grown up from the scientific and personal point of view as well. Thanks for believing in me even when sometimes I did not and for finding the right motivations when things were not going the way I expected. I believe that the teamwork we established over the years is precious and whatever and wherever my future will be I will never forget such a wonderful relationship based on respect and trust.

I want to thank my parents, Vincenzo and Margaret. You have taught me how important it is to pursue our personal goals with determination and sacrifice.

I also thank my husband, Andrea. The past two years have been not easy at all, but I had once again the opportunity to realize that without you by my side nothing would make any sense.

Finally, I want to thank all the LNS-INFN colleagues whose collaboration has been of fundamental importance to carry out the entire thesis work.